ADDIS ABABA UNIVERSITY

COLLEGE OF NATURAL AND COMPUTATIONAL SCIENCES

SCHOOL OF EARTH SCIENCES

A New Approach to Compact Gravity Inversion Algorithm.

by

Mesay Geletu

A Thesis Submitted in Partial Fulfillment of the Requirements for the Degree of Doctor of Philosophy

in

Geophysics (Applied Geophysics)

Addis Ababa University

Addis Ababa

Ethiopia

June, 2021

ADDIS ABABA UNIVERSITY
COLLEGE OF NATURAL AND COMPUTATIONAL SCIENCES
SCHOOL OF EARTH SCIENCES

This is to declare that the doctoral dissertation entitled: "A New Approach to Compact Gravity Inversion Algorithm" submitted by Mesay Geletu in partial fulfillment of the requirements for the degree of Doctor of Philosophy in Geophysics (Applied Geophysics) complies with the regulations of the university and meets the accepted standards with respect to originality and quality.

Approved by the Examining committee:

	Signature	Date
1. Dr. Elias Lewi (Advisor)	_____	_____
2. Prof. André Kazuo (External examiner)	_____	_____
3. Prof. Tilahun Mammo (Internal examiner)	_____	_____
4. Dr. Bayisa Regassa (Chair man)	_____	_____

DECLARATION

This is to declare that, this doctoral dissertation entitled: "A New Approach to Compact Gravity Inversion Algorithm" is submitted to School of Graduate Studies of Addis Ababa university for Ph.D. degree in Applied geophysics. And I would like to certify that all the research findings presented in this thesis were accomplished by myself, under the supervision of my advisor Dr. Elias Lewi. Materials or ideas used from other sources are cited accordingly.

Name: Mesay Geletu

Signature …….

Date ……

ABSTRACT

A New Approach to Compact Gravity Inversion Algorithm

Mesay Geletu

Addis Ababa University, 2021

The gravity method is one of the geophysical methods that has been used in a wider range of geophysical prospecting and investigations. One of the indispensable steps in this method is the inverse modelling of the measured data to estimate the subsurface density distribution and geometrical properties (e.g. shape and depth) of the causative bodies. Particularly, delineating localized and blocky geologic features, through the inversion of gravity data is an important goal in a range of geophysical investigations and it is still a subject of interest and concern in the scientific community. Most conventional inversion algorithms generally yield smooth models with poor edge definition. These methods have difficulties in recovering non-smooth distributions that have sharp boundaries. The main objective of this thesis was then to develop and implement a gravity inversion algorithm that can produce compact and sharp images, aiming at recovering localized and blocky geologic features with varying geometric representations. In the course of the thesis work, this goal has been achieved by presenting a gravimetric inverse modelling method that has been tested to be effective.

At the heart of the developed inversion method lies the usage of the L_0-norm minimization of the objective function, which consists of data misfit and L_0-norm stabilizing function, by an efficient iteratively reweighted least-squares (IRLS) algorithm. As a major contribution, the presented method incorporates three novel technical advancements. At first, the method incorporates an auto-adaptive regularization technique, which automatically determines a suitable regularization parameter, and a modified error weighting function that helps to improve both the stability and convergence of the method. The other advantage of the auto-adaptive regularization technique and error weighting matrix is that they are not wholly dependent on the known noise level. Because of that, the method can yield reasonable results even when the noise level of the data is not properly known.

The other major contribution is the use of a new depth weighting function. The advantages of the newly proposed depth-weighting function can be summarized as follows: (I) It properly counteracts the gravity kernel decay, so that the inversion results

can provide realistic depth information. (II) It avoids the selection of the depth weighting function parameters through trial and error, which was common in the traditional methods, through the usage of automated parameters selection techniques. Especially, this has a significant advantage when there is no prior depth information that helps to choose the optimum parameter in using the traditional depth weighting function.

Furthermore, to achieve geologically plausible results and also reduce solution ambiguity, a physical parameter inequality constraint algorithm has been developed and employed to constrain the obtained density contrast values.

Finally, the implementation of an effectively combined stopping criterion has been used to terminate the iterative inversion procedure, when geologically viable solutions are obtained. The proposed combined termination criteria are shown to outperform traditional termination criteria, used in most iterative geophysical inversion algorithms, through the modeling of synthetic and published measured data

To test the new method, forward and inverse modeling codes were written using Python programming in a Linux environment. The validity of the overall Python codes, and the practicality and efficiency of the presented inversion method were tested by inverting a number of synthetic data sets from geometrically complex bodies and field data sets from different geological settings. The results of the inversion confirmed the capability of the developed inversion method in producing geologically acceptable compact and sharp models that define the shape, location, and density distribution of the causative subsurface bodies. This proves, the reliability and effectiveness of the developed inversion method in practical applications to delineate sharp discontinuities and blocky features such as distinct layering or formation of localized bodies in the subsurface.

Key words: Gravity data, inverse modeling, regularization, compact and sharp image.

ACKNOWLEDGEMENTS

First of all, I would like to thank my advisor Dr. Elias Lewi for being my mentor since the beginning, for the insightful discussions, constructive criticism and encouragement. I am truly grateful for all the time he has dedicated to my success. I have been very privileged to have him as an adviser who is not only enthusiastic and caring, but also friendly.

My special thanks go to Wolkite University for sponsoring my Ph.D. research program at Addis Ababa University School of Earth Sciences. I am thankful to Addis Ababa University for its financial and logistic support. Particularly, I would like to thank all the staff and colleagues of the School of Earth Sciences who contributed to the accomplishment of my Ph.D. study. Especially, I am thankful to Prof. Tilahun Mammo and Dr. Bayisa Regassa for their support in the course of this Ph.D. research work.

I wish to acknowledge all staff members and colleagues of the Institute of Geophysics, Space Science and Astronomy of Addis Ababa University for all their assistance and allowing to use different office and computational facilities. Most importantly I would like to thank the irreplaceable Filagot Mengistu for her endless contributions and assistance throughout this Ph.D. research work. I am truly grateful for her support in the good and the bad moments, for encouraging me at all times, especially in those stressful moments that come throughout this study.

I am very thankful to my friends that have been there through the years and with whom I have spent incredible moments and enjoyed memorable times.

At last but not least my special gratitude also goes to my beloved mother Adanech, my father Geletu, and all my family members, who over the years have given me so much love and support. I feel so fortunate to have such great family in my life.

Table of Content

Contents

List of Figures

List of Tables

List of Acronyms

2D	Two Dimensional	11
3D	Three Dimensional	6
EM	Electromagnetic	29
FM	Forward modeling	2
GCV	Generalized Cross-validation	31
GSVD	Generalized Singular Value Decomposition	32
IM	Inverse modeling	2
IRLS	Iterative Re-weighted Least Squares	40
LC	L-curve	31
MDP	Morozov's Discrepancy Principle	31
MT	Magnetotelluric	42
NP	Nondeterministic polynomial	39
PPICA	Physical Parameter Inequality Constraint Algorithm	63
SVD	Singular Value Decomposition	32

List of Symbols

$\|\rho\|_p^p$	L_p–norm of a vector	23
a_{ij}	the element of the kernel matrix A	14
∇	Discrete approximation of the first derivative operator	29
∇^2	Discrete approximation of the second derivative operator	30
A	Kernel matrix	13
e	Noise Vector	13
$\mathbf{g}^{obs}$	Observed gravity data	27
$\mathbf{g}^{pre}$	Predicted data generated by forward modeling	27
k	Iteration counter	53
M	The number of cells (number of model parameters)	12
N	Denots the number of available observation points	13
$S(\rho)$	Stabilizing or regularization functional	22
$S_{L_2}(\rho)$	L_2–norm stabilizing function	28
$\mathbf{W}_{L_0}$	L_0-norm compactness stabilizing matrix	53
$\mathbf{W}_m$	General regularization matrix (model weighting matrix)	28
$\mathbf{W}_e$	Diagonal error weighting matrix	27
$\mathbf{W}_h$	Hard constraint matrix	53
$w_z(z)$	Depth weighting function	58
$\mathbf{W}_{zn}$	New depth weighting matrix	53
$w_{zn}(z)$	New depth weighting function	60
δ_ρ^2	Density variance	54
ε	Focusing parameter	42

μ	Regularization parameter	22
$\boldsymbol{\rho}$	Density contrast vector of the cells	13
$\boldsymbol{\rho}_F$	Prior reference density contrast model vector	28
τ	Threshold value for parameter variation function	66
φ	Threshold value for misfit variation	66
Φ_d	Data fidelity or misfit functional	22

CHAPTER 1: INTRODUCTION

1.1 General Introduction

Geophysics is a science that deals with the physical properties of the Earth based on measured data. Gravity method represents one of the oldest disciplines in geophysics and it has been used in a wide range of geophysical prospecting and investigations, such as in mineral exploration, engineering and environmental problems, archeological site investigations, and mapping the internal structures of the Earth (Reynolds, 2011; Hinze et al., 2013). The advancements in instrumentation systems and acquisition methods together with increasing positional accuracy since the advent of GNSS method increased data resolution and increased the demand for the gravity method with better appreciation. This has in turn necessitated the utilization of reliable and applicable gravity data interpretation approaches. The primary goal of a gravity anomaly interpretation that are generated by mass variations in the subsurface, is to estimate the densities, location and shapes (geometry) of the causative bodies. This is usually achieved through a forward or inverse gravity modeling. The development of an alternative inverse gravity modeling methodology is then will be the topic of this dissertation.

This chapter is divided into three sections. The first section provides a general theoretical background concerning the geophysical modeling including its major steps. In the second section, an overview about potential field inversion and its numerical difficulties and a review of existing work will be presented. The fourth section describes the research objectives and the outline of the thesis work.

1.2 Modelling

Modelling in geophysical investigation mainly involves the representation of the subsurface through a plausible arrangement of causative subsurface bodies with physical properties, by making use of geophysical and geological information, that are gathered on or/and below the surface of the Earth. This is usually carried out using sophisticated computational methods. In other words, geophysical modelling is a process that maps the observed data to the physical property of the subsurface by means of mathematical relations. The model is a one- or two- or three-dimensional digital

representation of the continuous subsurface physical property distribution. As compared to the measured geophysical data, the models are more easily interpreted and can be related to the geology of the study area. Thus, geophysical modelling is an indispensable step in geophysical data interpretation. Some examples of the physical properties of the Earth in geophysical modelling are density, conductivity, and magnetic susceptibility. In general, there are three main steps in the geophysical modelling process:

(I) **Discretization of the model**: Because the Earth is made up of subsurface features, that consist continuously varying physical properties, the first step in a modelling process is to systematically discretize the subsurface to make the modelling procedure manageable and easier. The discretization allows the utilization of available analytical expressions to compute the approximate anomaly of the causative bodies.

Depending on the target of interest, there are two approaches that are commonly followed in the discretization of the Earth for gravimetric data inversion. The first approach fixes the physical property values (e.g. density) and varies the geometry of each digitized cell. This approach results in a nonlinear problem during the modelling process. The second approach, which is also used in this work, fixes the geometry of the cells and varies the physical property of each cell. This approach leads to a linear system in the modelling process. Thus, the choice of the discretization of the subsurface naturally determines the modelling process.

(II) Forward modelling (FM): In this procedure set of geophysical field data (e.g. gravity or magnetic anomaly) are computed from given distribution of physical properties (model parameter) of each discretized cell and geological structure. It is based on the physical laws which can provide the means for computing the synthetic geophysical data for the given physical properties of the discretized model. Depending on the discretization approach, mentioned above, the relationship between theoretical or the observed data and the given physical properties is either linear or nonlinear.

(III) Inverse modeling (IM): This procedure involves the reconstruction of the physical properties or model parameters from a set of measured data, which is the reverse process of the forward modelling. That means, in the forward modelling one uses the model space to compute the data in the data space and in the inverse modelling one makes use of a measured data in the data space to search for an appropriate model

in the model space. A detail explanation about geophysical inverse modelling theory and Methods of solution are given in different standard books such as Menke (1989) and Zhdanov (2015).

Depending on the circumstances, one might opt for forward or inverse modelling and sometimes one might start with the forward modelling and use the result of the forward model as an a priori model in an inverse modelling. Irrespective of the approach, the modelling process usually commences through the discretization of the subsurface, which in turn depends on the problem at hand. Once the data is prepared and the discretization process is completed the forward and inverse modelling will begin following all necessary geophysical and geological priory information are prepared. The formulation of forward modelling is the inherent part of the inverse modelling and it plays an important role in testing geologic scenarios of the inverse problem so that calculated data generated from these scenarios can be compared with the observed data.

As geophysical modelling is a very vast topic, in the present work focus will be given to the development of potential field modelling, particularly gravity inverse modelling algorithm. Therefore, a detailed discussion about these major steps will be made in the framework of gravity inverse modelling.

1.3 **Potential Field Inversion**

Potential field inversion, such as gravity and magnetic field inversion methods, have an important role in the studies of the Earth's interior through the determination of the physical properties of rocks which are density and magnetic susceptibility respectively. Gravity inverse modelling, which is the topic of this thesis, is a mathematical modelling technique that is used to estimate the subsurface density distribution, geometry (size and shape), and location of a causative body from an observed gravity anomaly. Thus, inversion of gravity data is, therefore, an important step in the quantitative interpretation since the reconstruction of density contrast models markedly increases the amount of information that can be extracted from the gravity data. The reproduced density models must be best estimates of the true subsurface so that they are capable of predicting the measured data sufficiently.

In general, potential field inverse problems that arise in geophysics are ill-posed (Fedi et al., 2007). For this reason, in developing potential field inversion procedures, there are a number of numerical difficulties, as it is the case in any geophysical inversion methods (Al-Chalabi, 1971; Blakely, 1996; Barbosa et al., 2002). The major well-known difficulties are (Aster et al., 2018):

(I) **Non-uniqueness:** The solution of the inverse problem is not unique. As gravity data is measured on discrete points, there are several alternative models that can reproduce the same data. Firstly, this is due to the intrinsic problem of non-uniqueness, which is basically known from the Gauss theorem and is common in any geophysical method (Blakely, 1996). Secondly, it is because of the under-determinedness of the inverse problem, which is caused by the insufficient knowledge the observed data contains as compared to the number of the model parameters.

(II) **Non-existence:** There may be no model that generates exactly the observed data. This can occur in practice because the mathematical model of the system's physics is approximate or because the measured data are always contaminated with error or noise.

(III) **Instability:** Since the inverse problem is usually ill-posed, small changes in the observed data, for example, noise can result in large changes in reconstructed density model.

In general, the aforementioned facts make the recovery of the causative bodies (i.e. their physical properties, shape, and depth of burial) from only measured geophysical data impossible. Instead, it is common to look for a solution that approximates the true model by incorporating a priori information or constraints as additional information. This same principle also plays a crucial role in this work.

1.3.1 Constraints in Existing Potential Field Inversion Methods

Towards overcoming the aforementioned difficulties in potential field inverse problems, it is common to optimize the parameters by using a priori information and different mathematical techniques. The implementation of the a priori information or constraints is usually carried out by making assumptions on the following aspects: (1) about the model parameters (existing information on the subsurface structure from

geological or other geophysical observations) and (2) about the data parameters (statistical properties of the observed data, e.g. Gaussian distribution of errors). The a priori information or constraints can be in the form of geological or geophysical information and mathematical constraints. Numerous types of a priori information or constraints have been well described by many authors (e.g. Silva et al., 2001; Lelièvre et al., 2009). The benefits of utilizing a priori information or constraints in the inversion algorithms have been demonstrated by several authors (Phillips, 2002; Farquharson et al., 2008). Moreover, Boulanger and Chouteau (2001), Wijns and Kowalczyk (2007), Lelièvre et al. (2009), Rezaie et al. (2017a), and many others demonstrated the advantage of incorporating a combination of different a priori information or constraints in the inversion algorithm to dramatically improve the inversion results. Therefore, a good inversion procedure must incorporate this information into the inversion to overcome the non-uniqueness and to enhance inversion results leading to more reliable Earth models.

Several potential field inversion algorithms have been developed by incorporating a priori information into the inversion process. Each developed algorithm was characterized by a different type of a priori information or constraints that lead to different inversion results. In other words, the obtained solution is dependent on the prior information and the way it is implemented. For this reason, one cannot talk about a unique algorithm suitable for every geological situation (Silva et al., 2001). This means that it is very essential to select a reasonable algorithm according to the geological context of the study area and according to the available a priori information.

Generally, depending on the reproduced model features potential field inversion algorithms can be classified into two main groups: (i) smooth, and (ii) non-smooth approaches. Some of the examples of the most common algorithms that produce smooth models to recover geological structures with smooth behavior include Li and Oldenburg (1996 1998), Pilkington (1997), Boulanger and Chouteau (2001). Li and Oldenburg (2000) further improved Li and Oldenburg (1996, 1998) approach by incorporating additional information such as strike and dip information about the geologic structure. Additional bound constraints are included in Li and Oldenburg (2003) to their previous inversion procedure to allow specification of lower and upper bounds on the model parameters. However, these methods have difficulties in recovering blocky structures

or non-smooth distributions that have sharp boundaries or abrupt changes in physical properties (Farquharson, 2007; Rezaie et al., 2017b).

On the other hand, to produce focused and sharp images of the subsurface several non-smooth inversion strategies have been proposed by numerous researchers, such as by Bertete-Aguirre et al. (2002), Namaki et al. (2011), Vatankhah et al. (2018), Fournier and Oldenburg (2019), Rezaie (2019). Particularly, a compact gravity inversion method is a well-known method for the reconstruction of focused models of the subsurface in the area of potential field data inversion. The methodology was first proposed by Last and Kubik (1983) to estimate a compact density distribution. The basic idea in the original work of Last and Kubik method involves the minimization of the area of a 2D causative body, which is equivalent to maximizing its compactness, to define a sharp density boundary. Based on the pioneering work of Last and Kubik (1983) a large number of researchers have improved this principle in different ways, while constantly enhancing its efficiency and practicality. For example, Guillen and Menichetti (1984) extended that to allow specification of a dip line along which the moment of inertia is minimized. Barbosa and Silva (1994) generalized Guillen and Menichetti's (1984) method to allow compactness about several axes by a priori information about the axis length. Some instability of the original compact gravity inversion algorithm of Last and Kubik (1983) was reported by Lewi (1997), when the data is contaminated with error. Then Lewi (1997) has improved the original compact inversion by introducing a new approach to the 3D compact gravity inversion. The problem with his method arises when dealing with a multiple-source model, where the inversion algorithm tends to concentrate densities towards the surface of the Earth, regardless of the true depth of the causative bodies. Silva and Barbosa (2006) have developed an 'interactive inversion' in which the interpreter can set the arbitrary inertial axes as desired with the purpose of testing a geologic hypothesis, by employing the method of Barbosa and Silva (1994). All the methods that are proposed by Guillen and Menchetti (1984); Barbosa and Silva (1994); Silva and Barbosa (2006) including Silva Dias et al. (2009, 2011) strongly need various prior information to yield an accurate estimation (Meng et al., 2018). In other work, Portniaguine and Zhdanov (1999, 2002) extended the method of Last and Kubik's (1983) by introducing a minimum gradient support stabilizing functional that helps to produce focused models with sharp features.

Generally, with the increased demand for geologically viable and reliable information about the subsurface the inversion of potential field data to recover 2D and 3D model parameters became one of the topics that got attention in geophysical exploration and interpretation. Potential field inversion is a broad area of research and numerous different inversion strategies have been developed. Particularly, in the last three decades, the development of non-smooth gravity inversion methods that produce focused images of the subsurface density distribution has attracted much attention and it is an active area of research. This is because the non-smooth gravity inversion approaches are known to be the best in delineating sharp geological interfaces or blocky features, which is the main goal in a range of geophysical investigations. Taking this into account, in this thesis, a special focus is given to gravity inversion methods that can reproduce compact and sharp images.

1.4 **Research Objectives**

The present study aims at developing a new gravity inversion method that can produce compact and sharp images which help to estimate the geometry, location, and densities of multiple localized subsurface causative bodies based on the compact and focused gravity inversion algorithms. Therefore, the main objective of this work will be to investigate and further develop, the compact and focused gravity inversion methodologies. In particular, the thesis has the following specific objectives.

1) To study and review the different compact gravity inversion techniques already developed and analyze their strength and weaknesses.
2) To investigate different new ideas on how to improve those weaknesses observed in already developed methods in the compact gravity inversion algorithm and develop an inversion method, that can give a compact and sharp body that approximates the true causative body. In other words, different mathematical methods and ways to incorporate a priori information will be explored so that it is possible to improve the compact gravity inversion technique to deliver a geologically plausible model for multiple sources anomalies.
3) To develop several new computer programs to assess the strength and weaknesses of already existing methods, test new developments and finally prepare a working code that makes use of the newly developed

method. These programs, deal with the forward and inverse modelling of the gravity data including plotting and visualization. Here the Python programming language that makes use of different scientific computing packages such as Numpy, Scipy, Pandas, and Matplotlib will be used.

4) Demonstrate the effectiveness and the practicality of the developed forward and inverse modelling programs.

1.5 **Thesis Outline**

Considering this introduction part as Chapter 1, the thesis in total consists of six chapters. Apart from this, the abstract, a reference list, and the appendices form part of the thesis. Chapter 2 discusses the forward modelling procedure in gravity inversion and presents the developed computer programs for the implementation purpose. In this chapter, the parameterization or discretization methods of the model and formulation of the forward modelling procedure will be described. In addition to this, the forward problem equation and the Python modules that implement this equation are presented in the chapter. Chapter 3 introduces the basic principles and theory needed to solve the gravity inverse problem and the major concepts of some of the most popular potential field inversion algorithms are discussed. The explanations serve in particular as a basis for the new ideas that will be presented in more detail in the later chapters. In Chapter 4, the newly developed gravity inversion method that can produce compact and sharp models of the subsurface density distribution, to assist the recovery of non-smooth, blocky geologic features with sharp boundaries will be presented. In addition, the new contributions, which can also be incorporated in other inversion approaches and the developed Python programs to implement the presented gravity inversion algorithm are well described in this chapter. Chapter 5 provides a number of synthetic and real data inversion results to illustrate and prove the efficiency, and practicality of the developed gravity inversion strategy described in Chapter 4. Finally, in Chapter 6, I conclude by reflecting on the newly developed method, its advantages and drawbacks. At the end of the conclusion, a recommendation for future research will be provided.

CHAPTER 2: DISCRETIZATION AND SOLUTION TO THE FORWARD PROBLEM

2.1 Introduction

The goal of gravimetric FM is to determine the gravity field anomaly caused by a given density distribution under the surface of the Earth. On the contrary, inverse modelling is a process that involves the generation of a model from a given data set. In an effective gravity forward or inverse modelling process one needs a fast and accurate algorithm as a solution to the forward problem. Several methods have been developed to calculate the gravitational acceleration caused by a given subsurface feature. Providing a comprehensive description of the available methods is beyond the scope of this work. Thus, for a more complete review of the developed methods, one can refer to Nabighian et al. (2005).

In general, there are two approaches that are commonly used to model the subsurface in forward or inverse modelling. In the first one, the subsurface is divided into small cells of fixed geometry or structured grids and the density of each cell is assigned separately to reconstruct the desired model. Common to all existing fixed geometry forward or inverse methods, either two dimensional (2D) or three-dimensional (3D) cases, the Earth is usually discretized into small 2D or 3D cells respectively. The discretization allows the utilization of available analytical expressions to compute the approximate gravitational attraction of the single cell in space. The total effect of the model then will be the sum of the effect of the individual cells. In the second approach, the target subsurface density is commonly modeled using polygons that have fixed densities. The shape of the polygons is then varied to reconstruct the desired model. The methods that apply this type of discretization are usually called unstructured polygonal (geometric) methods (Snopek, 2005). To use unstructured polygonal discretization in order to solve the forward problem, several analytical expressions have been presented by different researchers, for example, Götze and Lahmeyer (1988), Holstein (1999), D'Urso (2014) and Ren et al. (2017).

This chapter mainly discusses the former method that is the model space discretization approach, which is using fixed geometries. This method is used in this work, to solve the forward problem and in the inverse modelling. In the first section,

some commonly available discretization approaches will be introduced. Subsequently, the discretization technique implemented here and the formulation of the forward problem are described in detail. In the second section, the solutions of the 2D and 3D gravity FM integral equations are presented.

2.2 Discretization of the Model Space and Formulation of Forward Problem

Depending on the scale of the problem at hand, the gravity exploration problems can be classified into global or regional (large scale) and local cases (small scale). In all circumstances (i.e. for large and small-scale problems) the subdivision of the subsurface into discrete elements permits the utilization of analytical expression with respect to the calculation of the gravitational acceleration of each element. In other words, after the subdivision of the Earth into discrete cells, the widely used Newton's integral, which can be done either in the spectral domain or spatial domain will be used (Kuhn and Seitz, 2005; Wild-Pfeiffer and Heck, 2007). Hirt and Kuhn (2014) presented a review of both spectral-domain and spatial domain methods. In the case of the spectral domain, the Newton's integral is evaluated through transformation into the spectral domain (e.g. Wieczorek, 2007; Novák, 2010; Hirt and Kuhn, 2012).

In the space domain methods for global or regional scale, the problem can be formulated in a spherical coordinate system and the subsurface density distributions are typically discretized into tesseroid elements to consider the curvature of the Earth problems (Heck and Seitz, 2007; Grombein et al., 2013; Uieda et al., 2016). For local scale problems, in the spatial domain, it is classically formulated in a Cartesian coordinate-system when the planar approximation of the earth's surface is acceptable.

In the approach which is implemented in this work, the geometries of the subsurface cells are fixed and the physical property values of the cells are varied to model the target. In this case, the subsurface density distributions are discretized into structured polygonal grid elements commonly rectangles or squares (for 2D) and right rectangular prisms (for 3D case). Since rectangular prisms are commonly used bodies, the methods that use this type of discretization are called rectangular prism methods. A

detailed comparison between the geometric methods that use polyhedron and rectangular prism method is given by Snopek (2005).

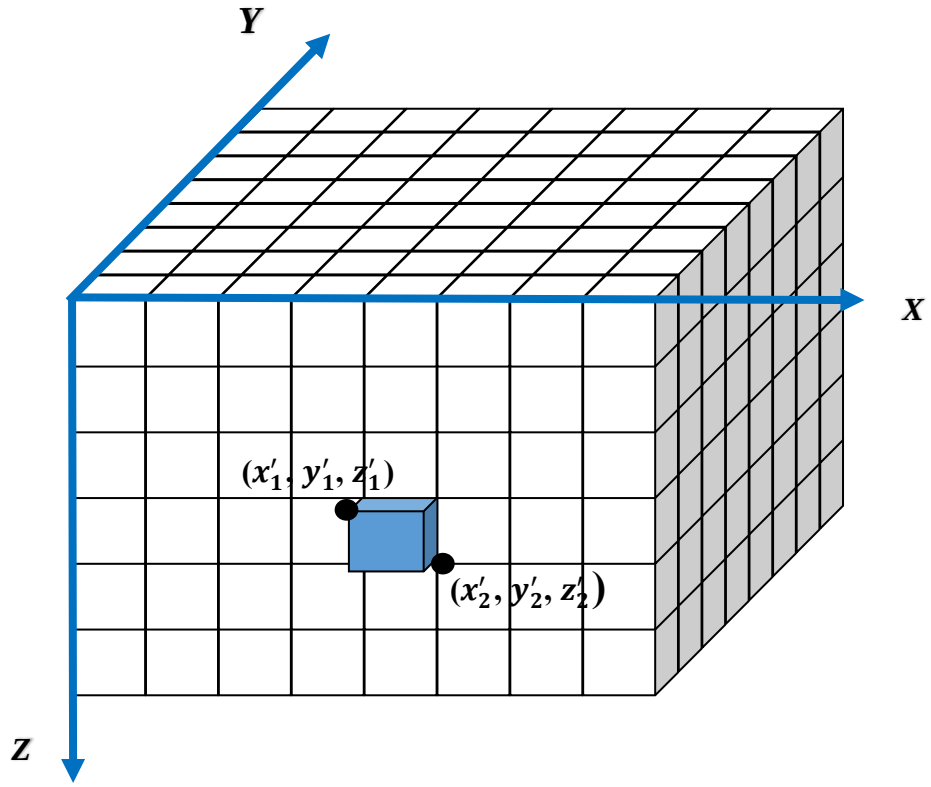

Figure 2.1: 3D subsurface model discretization.

In forward gravity modelling, digitizing the Earth by a finite number of right rectangular prisms provides a relatively simple and useful way to approximate complicated density sources (Caratori Tontini et al., 2009). Because of its simplicity, such type discretization is very common and have been implemented in several gravity modeling approaches for instance Boulanger and Chouteau (2001); Commer (2011) and many others. The subdivision of the subsurface under the survey area into a set of rectangular prismatic elements (for 3D case) is illustrated in Figure 2.1.

As parallelepipeds are used as building blocks for 3D modelling, parallelograms are used as building blocks for 2D gravity modelling. The 2D approximation of the subsurface model can be obtained from the 3D one by assuming that each rectangular prism is infinitely long in the Y-direction and has invariant density, with variations in densities are only allowed for the X and Z directions. Figure 2.2 illustrates the cross-section of the 2D discretization of the subsurface under a gravity profile. This 2D discretization has been applied in numerous 2D gravity modelling methods proposed by number investigators (e.g. Last and Kubik, 1983; Vatankhaha, 2014; Grandis and

Dahrin, 2014; Ghalehnoee et al., 2016). In the present work to perform inverse modelling and the forward gravity data computation data the subsurface under the survey area is discretized into a number of rectangular cells of known sizes and positions depending on the target of interest.

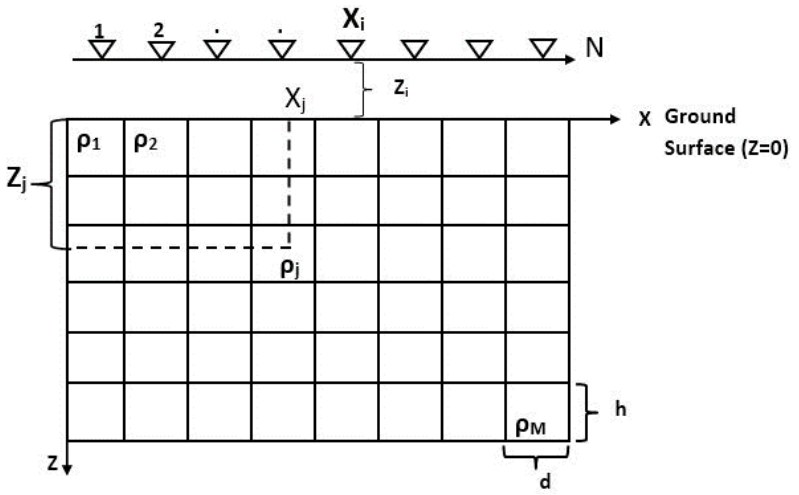

ρ: Density contrast, j=1…….*M*	n_X: Number of blocks in X
▽ : Gravity Station, i =1……*N*	n_Z: Number of blocks in Z
d: Width of the block	h: Height of the block

Figure 2.2: 2D Discretization of the earth model under the survey area with square cells. Gravity stations at the ground surface are located at centers of the blocks indicated by the ▽ symbols and dimensions of square cells are equal to the distances between two observation points.

As mentioned above, in this thesis the formulation of the forward gravity modelling was addressed by considering rectangular discretization of the model space as illustrated in Figure 2.2. For such discretized model, the geometry of each cell in the model structure remains constant and the only variable parameters are the densities of the cells. This leads to a linear relationship between the model parameters of each block and the resulting vertical gravitational field. In that case, the vertical gravitational attraction at the point caused by each cell can be calculated individually by using known analytical expression. Then the sum of the contributions from each of the individual cells produces the vertical gravity field data g_i at i^{th} measurement point, which can be mathematically formulated by:

$$g_i = \sum_{j=1}^{M} a_{ij}\rho_j + e_i \qquad j = 1,2,\ldots\ldots M \tag{2.1}$$

where M is the total number of cells (number of model parameters), ρ_j is the density of j^{th} rectangular block and it is assumed to be constant within the cell and e_i is a random noise associated with i^{th}measurement point. In equation 2.1 a_{ij} is a kernel matrix element, it depends on the geometry of the discretization, which represents the influence of the j^{th} cell on the i^{th} observation point gravity value and its computation will be described in the next section. If $\boldsymbol{\rho}$ denotes the model parameters that represent the density contrast vector of the cells, its components are then given in vector form as $[\rho_1, \rho_2, \ldots\ldots \rho_M]^T$. Here T represents the vector transpose. Similarly, the vertical gravity data vector is represented by $\boldsymbol{g}$ and its elements are given in a vector form as $[g_1, g_2, \ldots\ldots g_N]^T$, where N is the total number of available observation points and the superscript T denotes transpose. Then the linear forward modelling problem, relating the model parameter vector $\boldsymbol{\rho}$ to the gravity field data vector $\boldsymbol{g}$, can be formulated using the following mathematical equation in matrix notation:

$$\mathbf{g}_{\mathrm{Nx1}} = \mathbf{A}_{\mathrm{NxM}}\,\boldsymbol{\rho}_{\mathrm{Mx1}} + \mathbf{e}_{\mathrm{Nx1}} \qquad M > N \tag{2.2}$$

where $\boldsymbol{e}$ is the noise vector with N-dimensional and $\boldsymbol{A}$ is the kernel matrix that has a_{ij} ($i = 1,2\ldots N;\ j = 1,2,\ldots,M$) as it elements. In this thesis, the forward problem or the process of computing the gravity field from a given model is made using equation 2.2.

2.3 **Solution of Integral Equation**

As explained in section 2.2, rectangular prismatic cell or parallelepipeds (for 3D) and rectangle or square cell (for 2D) discretization permits the use of simple analytical formulas to compute the vertical gravitational attraction caused by each block. In this approach, because the geometry of the discretized model remains constant, the relationship between the density of each block and the vertical gravitational attraction is linear. This makes things easier in achieving the objective in solving the forward problem which is the determination of the predicted gravity data from the known model parameters using the kernel or mapping function. Different analytical formulas, based on the well-known Newton's integral equation, have been developed and used by

different researchers for both 3D and 2D cases. In the following, the mathematical expressions used to compute the elements of the kernel matrix, in both 3D and 2D cases are described separately.

The vertical gravitational attraction due to a three-dimensional arbitrary shape body with a volume V' at i^{th} measurement point located at $r_i = (x, y, z)$ in a Cartesian coordinates system is represented by the integral equation:

$$g_z(r_i) = \gamma \int_{V'} \rho(r') \frac{z' - z}{|r' - r_i|^3} dv' \qquad 2.3$$

where γ is Newton's gravitational constant ($\gamma = 6.67259\, x\, 10^{-11}\ m^3 kg^{-1} s^{-2}$) and $\rho(r')$ is the density of the infinitesimal volume dv' of the causative body, located at the location $r' = (x', y', z')$. Here, a right-handed Cartesian coordinate system having its origin on the Earth's surface with the z-axis pointing vertically downward is implemented. Similar to those 3D gravity forward problems we employ a rectangular prismatic cell discretization illustrated in Figure 2.1. For such discretization, the assumption is that the density contrast of each cell is assumed to be homogeneous and hence constant. In this case, using equation 2.3 we can express the vertical gravitational attraction due to the j^{th} rectangular prismatic cell as:

$$g_{zj}(r_i) = \rho_j \left[\gamma \int_{v'_j} \frac{z' - z}{|r' - r_i|^3} dv' \right] \qquad 2.4$$

where v'_j is the rectangular prismatic volume within j^{th} cell. The term in the square bracket is the element of the 3D kernel matrix **A** in equation 2.2 and with its elements denoted by a_{ij}. The elements of a_{ij} represent the influence of the j^{th} prism on the i^{th} gravity value which can be written as:

$$a_{ij} = \gamma \int_{v_j} \frac{z' - z}{|r' - r_i|^3} dv' \qquad 2.5$$

After the computation of the gravitational effect of each cell, the total gravitational anomaly at i^{th} observation point is obtained by the well-known superposition principle with respect to each individual source element. That means the gravitational anomaly of the body at any point could be approximated by summing the effects of all the

prismatic cells by using equation 2.1. The closed-form solution for the integral in equation 2.5 have different forms and has been derived by several authors (Nagy, 1966; Plouff, 1976; Banerjee and Gupta, 1977; Li and Chouteau, 1998; Nagy et al., 2000). For example, the 3D kernel element can be computed by using the analytical expression in equation 2.6 presented by Nagy et al. (2000).

$$a_{ij} = \gamma|||x\, ln(y+r) + yln(x+r) - z\, tan^{-1}\frac{xy}{zr}|_{x_1'}^{x_2'}|_{y_1'}^{y_2'}|_{z_1'}^{z_2'} \qquad 2.6$$

where $r = \sqrt{x^2 + y^2 + z^2}$ and $(x_1',\ x_2');(\ y_1',\ y_2');(z_1',\ z_2')$ are the edge coordinates of j^{th} the rectangular prism along the x, y, and z axes of a right-handed Cartesian system illustrated in Figure 2.1. As the main objective of this thesis work is the development of an applicable inversion method, the main focus is given to the 2D case, which doesn't demand large computational memory and time. However, the method can easily be extended to the 3D case, using the kernel function given in equation 2.6. Therefore, hereafter the discussion will focus on the 2D case only.

In exploring geologic structures such as faults, dikes, and rift zones for which the length of the source body in one direction is much longer than its extension in other directions, it is more efficient to model the subsurface with a 2-D algorithm rather than a 3-D approach. Moreover, 2-D sources are both easier to conceptualize and model than their 3-D counterparts (Blakely, 1996). Thus, like the 3D case, the mathematical expression for the analytical calculation of the 2D kernel matrix element from a 2-D cell is presented here. The vertical component of the gravitational attraction g_{zij} at the origin in Cartesian coordinate system, attributable to a 2D geological body is given by (Blakely, 1996):

$$g_{zij} = \rho_j\left[2\gamma\iint\frac{zdxdz}{x^2+z^2}\right] \qquad 2.7$$

where ρ_j the corresponding 2D density contrast of jth rectangular or square cell and assumed to be constant within the cell (Figure 2.2). Like the 3D case, the term in the square bracket is the element of the 2D kernel matrix **A** in equation 2.2 and is again denoted by a_{ij}. a_{ij} represents the influence of the j^{th} rectangular cell on the i^{th} gravity measurement point, which can be written as:

$$a_{ij} = 2\gamma \iint \frac{zdxdz}{x^2 + z^2} \tag{2.8}$$

Considering the 2D model in Figure 2.2 the solution for the integral in equation 2.8 can be expressed as follows (Last and Kubik, 1983):

$$a_{ij} = 2\gamma \left[\left(X_i - X_j + \frac{d}{2} \right) log \left(\frac{r_2 r_3}{r_1 r_4} \right) + dlog \left(\frac{r_4}{r_3} \right) - \left(Z_j + \frac{h}{2} \right) (\theta_4 - \theta_3) + \left(Z_j - \frac{h}{2} \right) (\theta_3 - \theta_1) \right] \tag{2.9}$$

here h and d are height and width of each cell respectively; X_j and Z_j are the horizontal and the vertical distance from the center of the reference point to the center of the j^{th} each cell (see Figure 2.2 for details) *and* γ is the universal gravitational constant and where:

$$r_1^2 = \left(Z_j - \tfrac{h}{2} \right)^2 + \left(X_i - X_j + \tfrac{d}{2} \right)^2, \qquad r_2^2 = \left(Z_j + \tfrac{h}{2} \right)^2 + \left(X_i - X_j + \tfrac{d}{2} \right)^2$$

$$r_3^2 = \left(Z_j - \tfrac{h}{2} \right)^2 + \left(X_i - X_j - \tfrac{d}{2} \right)^2, \qquad r_4^2 = \left(Z_j + \tfrac{h}{2} \right)^2 + \left(X_i - X_j - \tfrac{d}{2} \right)^2$$

$$\theta_1 = arctan \left(\frac{X_i - X_j + \frac{d}{2}}{Z_j - \frac{h}{2}} \right), \qquad \theta_2 = arctan \left(\frac{X_i - X_j + \frac{d}{2}}{Z_j + \frac{h}{2}} \right)$$

$$\theta_3 = arctan \left(\frac{X_i - X_j - \frac{d}{2}}{Z_j - \frac{h}{2}} \right), \qquad \theta_4 = arctan \left(\frac{X_i - X_j - \frac{d}{2}}{Z_j + \frac{h}{2}} \right)$$

In the present work, the mathematical expression of the 2D kernel in equation 2.9 is used to compute the kernel element as a solution for the 2D forward problem and the inverse modelling, which is also used by several authors (e.g. Last and Kubik, 1983; Guillen and Menichetti, 1984; Ghalehnoee et al., 2016).

2.4 **Brief Description of the Forward Modelling and Visualization Programs**

As part of this Ph.D. thesis work, a number of modules and packages have been developed to perform the discretization of model space, for data plotting and visualization, to implement equation 2.7 (which is the solution to the forward problem) and to carry out inverse modelling. The modules and packages are clumped together

into a **PyGM** package. The **PyGM** package is written in Python and hence have core dependencies on SciPy, NumPy, Pandas, and Matplotlib which are standard scientific computing packages in Python (Oliphant, 2007; Hunter, 2007; McKinney, 2012; Virtanen, et al., 2020). Python programming language was chosen for its free of charge, modern, and multi-platform interpreted object-oriented high-level language (Dubois et al., 1996; Lutz, 2013). The Python programs are easy to read, write and debug, which shortens the development cycle, and are easily extensible and embeddable, providing access to libraries and system-calls. Moreover, Python supports interactive coding, has extensive support for documentation, and has a large and growing open-source scientific community (Lin, 2012). Further detailed information about Python can be found on the Python Homepage (Van Rossum, 2005).

As noted earlier, the **PyGM** package consists of a number of Python modules and packages which are described in two different parts of this thesis. The inverse modelling implementation modules and functions will be described in Chapter 4. In this section, the modules developed for creating a mesh (i.e. discretization of the model space) and performing the Forward modelling, based on the above-discussed procedures, are described. In addition, the data plotting and model visualization, and data file reading modules are also described in this section. The list of the main available modules developed to perform these tasks are given in Table 2.1

PyGM.mesh2.py is a 2D structured mesh generating module that is developed based on the work of Uieda et al. (2013). The **PyGM.mesh2.py** module contains classes that generate a collection of geometric elements. For example, a model mesh consisting of rectangular elements is constructed by the SquareMesh class. The model mesh can be passed to functions that ask for a list of rectangular elements. Moreover, density values can be assigned to each element of the mesh using the "*addprop"* method. The forward modelling is performed by the module **PyGM.gra_2d.py**, which consists of a number of functions to handle it. The computation procedure, according to the theory explained in sections 2.2 and 2.3 is described as follows. Firstly, the function **PyGM.gra_2d.**kernel.py performs the calculation of the kernel matrix, using the expression in equation 2.9, taking the model mesh from the **PyGM.mesh2.py** module and the measurement location as in input. The kernel matrix provides the forward mapping from the model to the data (equation 2.2) during the entire modelling process.

Table 2.1 Developed codes for model space discretization, data plotting and for implementing the solution for forward problem.

No	Written module	Uses of the module
1	**PyGM.mesh2.py**	Includes a number of functions and Python classes to creates two-dimensional rectangular mesh (performs discretization of the model space)
2	**PyGM.meplot.py**	Plotting module (e.g. the density distribution of the model, and error between observed and calculated data).
3	**PyGM.gra_2d.py**	The FM module (calculates the kernel and the vertical gravitational attraction
4	**PyGM.rdata.py**	Data reading module (e.g. reads gravity or density data file)

Rather than computing each time the kernel matrix is computed once and stored to be used when it is required during forward or inverse modelling. This greatly increases computational performance while marginally increasing memory requirements. Secondly, the module **PyGM.gra_2d**.gzm.py calculates the synthetic gravity data taking the kernel matrix and the assigned density values as an input parameter. Finally, the **PyGM.meplot.py** module contains functions to carry out plotting and model visualization tasks. Python language libraries such as matplotlib (Hunter, 2007), Tkinter (Grayson, 2000), and pandas (McKinney, 2011), are used to write **PyGM.meplot.py** module.

CHAPTER 3: INVERSE PROBLEMS AND SOLUTION METHODS

3.1 Introduction

As it has been introduced in Chapter 1, geophysical inversion is a process that is used to determine the physical properties (model parameters) of the Earth from a set of measured data. One component of geophysical inversion is potential-field inversion which involves the reconstruction of density and/or magnetic source distributions from measured potential-field data. The present thesis particularly focuses on the development of a gravity inversion algorithm. The principal aim of the gravity inverse problem is to find a geologically plausible model based on the given observed gravity data. In other words, the objective in solving the gravity inverse problem is given the observed gravity data, it is to estimate density distribution, geometry, and location of the anomalous bodies in the subsurface of the Earth, by using mathematical modelling techniques. In Chapter 2, the equations that relate the density distribution to the gravity response, for a collection of rectangular cells making up a discrete Earth, has been discussed. In this chapter, a review of the basic principles and theory needed to solve the gravity inverse modelling will be made. Moreover, the basic concepts of some of the most popular potential field inversion algorithms will be discussed. The explanations will in particular serve as a basis for newly developed method that will be presented in more detail in the later chapters.

The remaining part of this chapter is arranged as follows. The second section presents the general ideas about geophysical inverse problem, focusing on a gravity inverse problem, including its mathematical framework. The third section discusses the fundamental concepts of regularization in geophysical inversion. In the fourth section, a variety of norms and general measures of the length of a vector are introduced including their mathematical definition, since they are very essential to define both the misfit and stabilizing functions. The fifth section, explains important concepts of the most popular smooth potential field inversion algorithms with their objective function and associated minimization methods. In the sixth section, the concept of widely used non-smooth inversion method including the corresponding regularization, and minimization approaches are described.

3.2 **Defining and Formulating the Inverse Problem**

This section presents a detailed explanation of the basic concepts and formulation of the inverse problem. As already mentioned, in geophysics the establishment of solution to the forward problem is a process of generating synthetic data from a given Earth model. This then can be used in the forward or inverse modelling. In the present work, the solution of the forward problem is established by making use of the linear equations relating the subsurface density distribution to the gravity response, as given in section 2.2 (equation 2.2). On the contrary, geophysical inversion is the process of estimating model parameters from observed data by using different mathematical modelling techniques. Accordingly, geophysical inversion of gravity data constitutes an important step in the quantitative interpretation since the recovery of the model parameters remarkably increases the amount of information that can be extracted from the given observed data. Consequently, many problems in geophysics can be formulated as inverse problems and have become an inevitable part of current geophysical studies.

In the context of gravity inversion, the inverse problem can be defined as follows: considering the linear system of equation given in (equation 2.2), solving gravity inverse problem involves using the known observed gravity data ($\mathbf{g}^{obs}$) and the kernel matrix ($\mathbf{A}$), estimating the density distribution vector ($\boldsymbol{\rho}$) which predicts the observed data with a certain noise level and at the same time satisfies certain constraints. Mathematically, the gravity inverse problem is often formulated by discretized linear system of equations relating the unknown model parameter vector $\boldsymbol{\rho}$ to the given gravity data $\mathbf{g}^{obs}$ and it can be written as:

$$\mathbf{A}_{Nx\ M}\boldsymbol{\rho}_{Mx1} + \mathbf{e}_{\mathrm{Nx1}} = \mathbf{g}^{\mathrm{obs}}_{\mathrm{Nx1}} \qquad 3.1$$

Equation 3.1 represents the simplest and best-understood linear system of equations of the inverse problem. Many important inverse problems that arise in the physical sciences involve precisely this equation.

Usually, gravity inverse problem is under-determined problem, that means the number of the model parameter vector $\boldsymbol{\rho}$, that has M number of parameters, exceeds the number of observations, represented by N, that is $M > N$. Consequently, like the majority of practical inverse problems arising in geophysical modelling, gravity

inversion is ill-posed problem (see section 1.3) which results in non-uniqueness and instability in the solution. The presence of noise associated with the measurement of field data further complicates the problem. Silva et al. (2001) also pointed out that a non-unique or unstable solution (characterizing an ill-posed problem) results from an imbalance between the information contained in data and the information the interpreter intends to extract from the data. Solving equation 3.1, for density distribution vector $\boldsymbol{\rho}$, in a least-squares sense yields unstable, and an approximate solution which may differ significantly from the real substance density distribution due to the non-uniqueness of the problem. That means a number of different models can still lead to the same solution. Regularization methods must be used in order to overcome the difficulties in solving an ill-posed problem and a priori information are also crucial. Often an ill-posed inverse problem is solved via a regularized data fitting approach, which chooses an optimal model by minimizing an objective function that takes into account both fitness to data and prior knowledge. In the following section, the basic concepts of regularization and the formulation of the general framework in geophysical inversion will be described.

3.3 **Regularization of Inverse Problems**

In this section, a short overview about the basic principles of the regularization theory and its general mathematical framework in geophysical inversion will be presented. As introduced earlier, regularization (stabilization) methods that incorporate a priori information must be used in order to overcome the non-uniqueness and instabilities in solving the ill-posed problems. Regularization, in geophysical inversion, refers to a process of introducing additional information in order to solve an ill-posed problem. The regularization has a dual purpose such that it is improving the conditioning of the linear systems and it imposes constraints on the solution which in turn helps to reduce the number of possible solutions to those that are meaningful (Hansen, 1998). Additional information used in the regularization process is usually based on prior knowledge we have about the study area. This information is usually incorporated in the form of stabilizing (regularization) functions.

As we will see later in more detail, there are two popular forms of regularization. The first common forms of regularization called the Tikhonov regularization introduces an L_2-norm regularization function in order to retrieve smooth solutions (Tikhonov and

Arsenin, 1977; Fuhry and Reichel, 2012; Tikhonov et al., 2013). The second common form of regularization aims at recovering non-smooth solutions. This is achieved by non L_2-norm regularization function. In this context, we have sparsity-based regularization, which is at the core of this work. In both forms of regularization, the standard strategy to solve the gravity inverse problem is to recover the model parameters $\boldsymbol{\rho}$, which is consistent with the data set and at the same time with some a priori assumptions, by minimizing an objective function (Tikhonov parametric functional). The objective function (Φ) is generally a combination of two functions such as a data fidelity or misfit functional Φ_d and stabilizing (regularization) functional $S(\rho)$ or sometimes also called the model objective function. A popular mathematical representation of the objective function, for the solution of the ill-posed geophysical inverse problem, can be given as follows (Tikhonov and Arsenin, 1977; Tikhonov et al., 2013):

$$\Phi = \Phi_d + \mu^2 S(\rho) \qquad 3.2$$

where μ is the regularization or damping parameter which controls the trade-off between the data misfit and the stabilizing term. Equation 3.2 can be regarded as a general mathematical framework that transforms the inverse problem to an optimization problem when minimized, produces a model that is acceptable.

In equation 3.2 the misfit functional measures how well, the predicted data reproduce the observed data and the stabilizing functional is a measure of model complexity. Designing the objective function with different assumptions to define the misfit and the stabilizing functional have dominated the literature over the past few decades. Clearly, imposing different assumptions leads to different regularization techniques, but also to different solutions (Gholami and Hosseini 2013). The next step in setting up the inversion is to define the misfit and the regularization functions. Hence, the following section discusses different measures of the length of a vector that help to define the misfit and the stabilizing functional in subsequent sections.

3.4 **Norms and General Measures of the Length of a Vector**

A norm of a vector is a real non-negative value representing intuitively the length or magnitude of the vector and denoted by $\|\cdot\|$. In this work, as an example, the elements of the vector are the misfits between observed and predicted data, or the

parameters describing a model (density contrast). The mathematical definition of several measures of the length of a vector, which have been used in geophysical inversion, will now be briefly reviewed. Consider the model parameter vector $\boldsymbol{\rho}$ that represents the density contrast of the rectangular cells with each component of the vector $[\rho_1, \rho_2, \ldots . \rho_M]^T$. Then the most widely used Euclidian norm of this vector is given by:

$$\|\boldsymbol{\rho}\|_2 = \left(\sum_{j=1}^{M} {\rho_j}^2\right)^{1/2} = \sqrt{{\rho_1}^2 + {\rho_2}^2 + {\rho_3}^2 \ldots \ldots {\rho_M}^2} \qquad 3.3$$

For convenience, in geophysical inversion, the square of the Euclidian norm is used which has the following form:

$$\|\boldsymbol{\rho}\|_2^2 = \left(\sum_{j=1}^{M} {\rho_j}^2\right) = {\rho_1}^2 + {\rho_2}^2 + {\rho_3}^2 \ldots \ldots {\rho_M}^2 \qquad 3.4$$

A more general and commonly used norm of a vector is p-norm, or L_p–norm which is defined as:

$$\|\boldsymbol{\rho}\|_p^p = \left(\sum_{j=1}^{M} |\rho_j|^p\right) = |\rho_1|^p + |\rho_2|^p + |\rho_3|^p \ldots \ldots |\rho_M|^p \qquad 3.5$$

In equation 3.5 $\|\cdot\|_p^p$ denotes L_p–norm of a vector. The subscript p denotes the L_p–norm, and the superscript p denotes the power of the L_p–norm. The value of p can be ≥ 1 depending on the chosen norm and controls the weight put on each and every element of the vector. For example, it can easily be seen that when $p = 2$, this general expression results in the L_2–norm or square Euclidean norm presented in equation 3.4, and for $p = 1$ gives the L_1–norm of the vector which can be written as:

$$\|\boldsymbol{\rho}\|_1 = \sum_{j=1}^{M} |\rho_j| = |\rho_1| + |\rho_2| + |\rho_3| \ldots \ldots . + |\rho_M| \qquad 3.6$$

Even though, the general L_p–norm in equation 3.5 has favorable mathematical properties, it is discontinuous at some points which make the derivative undefined at some locations. Thus, its numerical implementation in a minimization geophysical inverse problem can be difficult. To overcome this difficulty, several approximations

to L_p–norm were proposed. Huber (1964) proposed a formula to estimate L_p–norm of a vector which is expressed as:

$$\sum_{j=1}^{M}|\rho_j|^p \approx \sum_{j=1}^{M}\begin{cases}\rho_j^2, & |\rho_j| \le \delta \\ 2\delta|\rho_j| - \delta^2, & |\rho_j| > \delta\end{cases} \qquad 3.7$$

where δ is a is a positive threshold value at which the behavior the Huber norm function changes from quadratic to linear. Similarly, a modified version of L_p–norm was suggested by Ekblom (1987) is defined as:

$$\sum_{j=1}^{M}|\rho_j|^p \approx \sum_{j=1}^{M}(\rho^2+\varepsilon^2)^{p/2} \qquad 3.8$$

where ε is a positive number having a value that should be small compared to the elements of the vector $\boldsymbol{\rho}$. When ε is insignificantly small relative to ρ_j, Ekblom norm behaves like L_p–norm, that is for instance Ekblom norm approaches L_1–norm (equation 3.6) when $p = 1$, and L_2–norm (equation 3.4) when $p = 2$. The Huber and Ekblom norms are numerically easier to deal with than the straightforward L_p–norm in equation 3.5, when a derivative-based iterative minimization technique is employed to solve the inverse problem because their derivatives exist everywhere (Farquharson, 2008). For this reason, both Huber and Ekblom norms, mainly for $p = 1$ and $p = 2$, have been widely used in geophysical data inversion and processing techniques (Gorodnitsky and Rao, 1997; Guitton and Symes, 2003; Farquharson, 2008; Daubechies et al., 2010; Sun and Li, 2014; Singh et al., 2018).

The other L_p–norm approximation that has received considerable attention in geophysical inversion, is the one proposed by Lawson (1961). The Lawson L_p–norm approximation function is expressed as:

$$\sum_{j=1}^{M}|\rho_j|^p \approx \sum_{j=1}^{M}\frac{\rho_j^2}{\left(\rho_j^2+\varepsilon^2\right)^{1-\frac{p}{2}}} \qquad 3.9$$

A Number of geophysical inversion algorithms, that employ this Lawson L_p–norm approximation, have been developed by researchers (e.g. Fournier and Oldenburg, 2019;

Fournier et al., 2020; Shang et al., 2020). Note that, $p = 0$, $p = 1$ and $p = 2$ commonly form the main applications.

There is also another option for an alternate measure of the length of a vector informally called the L_0 –norm. This norm does not satisfy all the axiomatic requirements of a norm (Elad, 2010). Hence, an approximate expression is usually adopted to convert the L_0 –norm into an equivalent norm for the suitability of computation. As a classic example, the L_0–norm can be approximated by using L_p–norm (equation 3.10) with $p \to 0$; and can be defined as (Elad, 2010):

$$\|\boldsymbol{\rho}\|_0 = \lim_{p \to 0} \|\boldsymbol{\rho}\|_p^p = \lim_{p \to 0} \sum_{j=1}^{M} |\rho_j|^p \qquad 3.10$$

The L_0–norm simply counts the number of nonzero elements in the vector $\boldsymbol{\rho}$. To demonstrate this counting behavior, Figure 3.1 presents the graph of the function $|\rho_j|^p$ for different values of p between 0.01 and 2. We can see that as p tends to zero, the value of $|\rho_j|^p$ becomes an indicator function which is equal to 0 if $\rho_j = 0$ and 1 elsewhere. Hence, the summation of $|\rho_j|^p$ for all the entries of ρ_j provides a count of the non-zero values of this vector, as claimed.

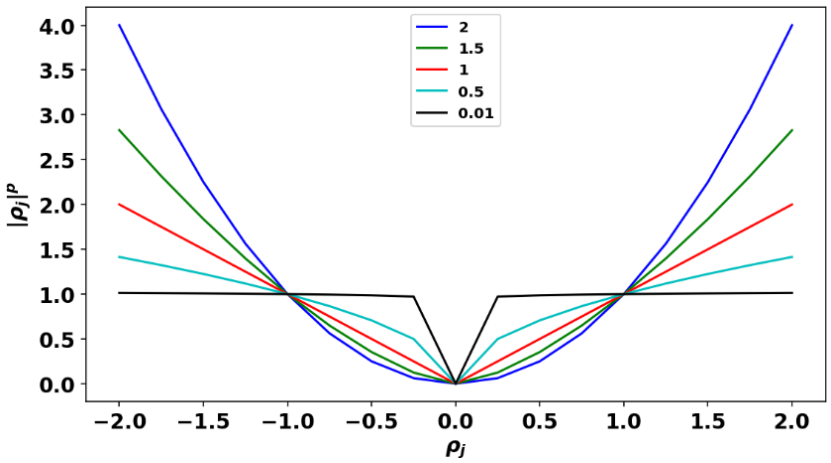

Figure 3.1: The behavior of $|\rho_j|^p$ for several decreasing values of p. As p tends to zero, $|\rho_j|^p$ gets closer and closer to the indicator function, which is 0 for ρ_j = 0 and 1 elsewhere.

The L_0–norm has been broadly utilized in many fields. For example, it was used for face recognition (Fan et al., 2015), for signal recovery (Wang et al., 2018; Xiang et

al., 2019), for image reconstruction (Wei, et al., 2018; Li et al., 2019); feature selection (Han et al., 2015). For a more detailed overview about the applications of L_0–norm, the reader is referred to a survey paper by Zhang et al. (2015). The L_0–norm has also been applied in geophysical data processing and inversion. It was utilized in the seismic data inversion (Chen et al., 2013; Liu et al., 2018), for potential field inversion (Zhao et al., 2016; Meng, 2018; Hu et al., 2019; Feng et al., 2020). Moreover, in the last decades, the L_0–norm has been implemented extensively in various potential field inversion modelling algorithms and received considerable attention in the literature. Considering this, the present thesis particularly focuses on L_0–norm and hence it will be revisited and discussed in more detail in subsection 3.6.3.

As already discussed in chapter 1, numerous potential field inversion algorithms have been developed. Each developed algorithm is characterized by a different type the data fidelity term and stabilizing functional that leads to different forms of the objective function, which in turn leads to different solutions. More commonly, different types of stabilizing functional have been used as a priori information or constraints and then to provide different inversion results. In other words, the obtained solution depends on the choice of the regularization function in the global objective function in equation 3.2. By using different measures of the length of a vector explained above several types of stabilizing function have been proposed and implemented in potential field inversion algorithms. Generally, depending on the recovered model features, resulting from the different choice stabilizing functional employed, potential field inversion algorithms can be classified into two main categories: (i) smooth, and (ii) non-smooth approaches. The following sections discuss these approaches separately.

3.5 **Smooth Inversion**

This section describes existing smooth inversion methods. As noted already, smooth inversion is not purely the topic of this thesis, but I will take away some ideas from it. Therefore, here only a general overview of the smooth inversion method is discussed. Extensive background on the regularized smooth inversion algorithms with smoothing stabilizer can be found in the literature for instance in Constable et al. (1987); Li and Oldenburg (1996, 1998); Pidlisecky et al. (2007), and many others. Moreover, for a rigorous mathematical treatment of these methods, readers are referred to the standard texts in this field (e.g. Menke 1989; Hansen 1999). Here, the subsections

(3.5.1 and 3.5.2) describe the data fidelity and stabilizing functions, which are used to define the general objective function in equation 3.2 in the case of smooth regularized inversion. Then, subsections (3.5.3 and 3.5.4) introduce physical parameter bound constraints and optimal regularization parameter choice methods respectively. Finally, commonly applied optimization algorithms for the minimization of the formulated general objective function are discussed.

3.5.1 The data misfit function

The data misfit function Φ_d usually measures how well the calculated data reproduce the observed data. Its formulation depends on the assumed distribution of the noise in the observed data. The typical noise models and their corresponding data fidelity functions are well-reviewed by (Yuan and Ghanem, 2017). Traditionally, the L_2–norm measure is the most proper measure of the data misfit if the measurement noise in the data follow a Gaussian distribution (Scales et al., 1988), which is the most commonly assumed case in geophysical inverse problems. With this assumption, L_2–norm measure data misfit is defined as:

$$\Phi_d = \sum_{i=1}^{N} \left(\boldsymbol{g}_i^{pre} - \boldsymbol{g}_i^{obs} \right)^2 \qquad 3.11$$

where N is the number of data, $\boldsymbol{g}_i^{obs}$ is the i^{th} observed datum, $\boldsymbol{g}_i^{pre}$ is the i^{th} predicted datum generated by forward modelling of the model $\boldsymbol{\rho}$. Observed data in field studies always contain different noise levels at different observation points, thus a weighting factor can be introduced to ensure that noisy data has less effect on the inversion results. This weighting coefficient can be represented by standard deviations of the repeated measurements. By incorporating the error weighting factor in equation 3.11, the data fidelity function in matrix notation can be written as:

$$\Phi_d = ||\mathbf{W}_e(\boldsymbol{g}^{pre} - \boldsymbol{g}^{obs})||_2^2 \qquad 3.12$$

where $\boldsymbol{g^{pre}} = \boldsymbol{A\rho}$, $\mathbf{W}_e$ is diagonal data or error weighting matrix (its dimension is $N \; x \; N$), whose ith element is $1/\sigma_i$, defines the relative contribution of each individual error to the total prediction error. The term σ_i represents the standard deviation of the i^{th} observation. In this thesis, the noise associated with the gravity data measurement

is assumed to be Gaussian and uncorrelated in nature and hence L_2–norm measure of data misfit, given in equation 3.12 is implemented.

3.5.2 L_2–norm Regularization

In a regularized inversion, the stabilizing functional (or the stabilizer) $S(\rho)$ is used to stabilize the solution and to allow the integration of a priori information about the desired solution such that the solution remains geologically plausible. For these reasons, various forms of regularization functions have been proposed over the last decades and added in regularized geophysical inverse problems. As introduced in section 3.3, one of the forms of regularization is Tikhonov regularization, which introduces an L_2–norm of the model parameter as stabilizing function in order to retrieve smooth solutions. Like the data misfit function the L_2–norm of model structure has been usually used in smooth geophysical inverse modelling, because its minimization results in a linear system of equations to be solved if the data equation is linear or can be linearized (Farquharson 2008). In other words, in smooth regularized inversion schemes the classical smoothing stabilizers is the L_2–norm of the model parameter that is given by:

$$S_{L_2}(\rho) = \sum_{j=1}^{M} {\rho_j}^2 = \|\boldsymbol{\rho}\|_2^2 \qquad 3.13$$

To incorporate additional priori information in the stabilizing functional model weights can be introduced to equation 3.13. In this case, the widely used, general form of the L_2–norm, which is weighted stabilizing functional can be defined as follows:

$$S_{WL_2}(\rho) = \|\boldsymbol{W}_m(\boldsymbol{\rho} - \boldsymbol{\rho}_F)\|_2^2 \qquad 3.14$$

where $\boldsymbol{\rho}_F$ is a prior reference model vector. The reference model is sometimes omitted by setting $\boldsymbol{\rho}_F = \mathbf{0}$. $\boldsymbol{W}_m$ is a general regularization matrix also known as a model weighting matrix (its dimension is $M \times M$) which is designed so that a model with specific characteristics is produced. Furthermore, both $\boldsymbol{\rho}_F$ and $\boldsymbol{W}_m$ allow for a priori information to be incorporated into the inversion that may come from other geological or geophysical investigations.

With the definitions given above, it is now possible to redefine the typical objective function used in regularized smooth geophysical inverse problems.

Substituting equations 3.12 and 3.14 in equation 3.2 the conventional, Tikhonov or L_2–norm regularization (Tikhonov and Arsenin, 1977; Tikhonov et al., 2013), objective function can be written in the following form:

$$\Phi_{L_2} = ||\mathbf{W}_e(\boldsymbol{A\rho} - \boldsymbol{g}^{obs})||_2^2 + \mu^2 \|\boldsymbol{W}_m(\boldsymbol{\rho} - \boldsymbol{\rho}_F)\|_2^2 \qquad 3.15$$

As it can be seen, in equation 3.15 the L_2-norm measure is applied on both the data misfit and stabilizing functions. Regardless of the optimization scheme used, most regularized smooth geophysical inversion algorithms seek to minimize this form of objective function. For example, it has been applied for inversion of electromagnetic (EM) sounding by Constable et al. (1987), for resistivity inversion by Pidlisecky et al. (2007), and for 3-D inversion of magnetic and gravity data by Li and Oldenburg (1996) and Li and Oldenburg (1998) respectively.

The weighting matrix $\mathbf{W}_m$, in equation 3.13, can take many forms depending on the desired solution and the type of a priori information that may be available. By taking $\boldsymbol{W}_m$ = I (where I is the identity matrix) and $\boldsymbol{\rho}_F = 0$ the overall size of the solution is assumed to be small (i.e. model parameters are concentrated close to zero). In this case, the minimization process of the objective function becomes numerically simpler than other choices of $\boldsymbol{W}_m$ however it results in geologically unreasonable smooth solution (Hansen 1999) and hence, in many applications this choice is not optimal. Therefore, choosing $\boldsymbol{W}_m \neq I$ can often lead to a much better approximate solution. Thus, a first or second-order derivative operator is used, depending on the assumption that the solution is smooth in the appropriate sense. The first and the second derivatives are usually referred to as 'flatness' and 'smoothness' constraints in the literature (Boulanger and Chouteau, 2001). A discrete approximation of the first and the second derivative operator can be modeled in form of matrix as given by equations 3.16 and 3.17 respectively.

$$\nabla = \begin{bmatrix} 1 & -1 & 0 & \dots & \dots & 0 \\ 0 & 1 & -1 & 0 & \dots & \vdots \\ \vdots & 0 & \ddots & \ddots & & \vdots \\ \vdots & \vdots & \ddots & \ddots & \ddots & \vdots \\ \vdots & \vdots & & & \ddots & \ddots \\ 0 & \dots & \dots & 0 & 1 & -1 \end{bmatrix} \qquad 3.16$$

$$\nabla^2 = \begin{bmatrix} -1 & 2 & -1 & 0 & \dots & 0 \\ 0 & -1 & 2 & -1 & & \vdots \\ \vdots & 0 & \ddots & \ddots & \ddots & \\ \vdots & \vdots & \ddots & \ddots & \ddots & \vdots \\ \vdots & \vdots & & \ddots & \ddots & \ddots \\ 0 & \dots & 0 & -1 & 2 & -1 \end{bmatrix} \qquad 3.17$$

3.5.3 Depth Weighting

Most often, the model weighting matrix $\mathbf{W}_m$ is not only flatness or smoothness weighting matrix, also include other constraint or weighting matrices. Note that, the weighting matrices must be expressed by the same dimension. For example, a depth (Li and Oldenburg, 1996, 1998) or a sensitivity (Zhdanov, 2002) weighting matrix is generally incorporated into the stabilizer term in potential field inversion. The model weighting matrix $\mathbf{W}_m$, given by the product of depth weighting and flatness or smoothness matrices, has been successfully applied in smooth regularized potential field inversion schemes **(**Li and Oldenburg 1996, 1998; Boulanger and Chouteau, 2001). The purpose of the sensitivity or depth weighting matrix is to counteract the decay of potential fields as a function of depth from the observation point. This in turn prevents the tendency of the recovered model structure to concentrate near the surface. A more detailed discussion about the depth weighting function, and comparative analysis between previously known and newly introduced depth weighting functions will be given in Chapter 4.

3.5.4 Physical Parameter Bound Constraints

As mentioned already, the objective function in equation 3.15 has the flexibility to incorporate many types of prior knowledge into the inversion equations to obtain inversion results with more realistic physical and geological meaning. For instance, physical property data from rock and core samples (Lelièvre et al., 2009), structural knowledge (Lelievre and Oldenburg, 2009). Particularly, implementation of physical parameter equality or inequality constraints can improve the solution of inverse problem by producing stable and geologically plausible results and also effective in reducing solution ambiguity (Oldenburg and Li, 2005). In the context of gravity inversion, lower and upper bound density constraints on the recovered density contrasts provide a powerful means to restrict the density values within the imaging volume to

be within the geologically acceptable or reasonable range. A number of real data interpretations that integrate lower and upper bound density constraints in the inversion procedure are given in Phillips (2002) and Farquharson et al. (2008). In potential field inversion, several strategies that incorporate the physical parameter equality or inequality constraints in the optimization process have been proposed. Further details about the physical parameter constraint including some of the strategies followed to incorporate it in the inversion process will be discussed in section 4.8.

3.5.5 Choosing the Regularization Parameter

Selecting an optimal regularization parameter μ in equations (3.2 and 3.15) is a crucial part of the solution process because it directly affects the inversion results. A large value of μ (equivalent to over-regularization) favors a small solution semi norm at the cost of a large residual norm, while a small, (i.e., under regularization) has the opposite effect. Thus, the regularization parameter is an important parameter which controls the properties of the obtained regularized solution, and should therefore be chosen with care (Zhdanov, 2015).

Several strategies have been proposed for estimating a suitable regularization parameter. These techniques can be divided into two classes (Hansen, 1998): (I) those that are based on knowledge or a good estimate of the error in the observations, such as Morozov's discrepancy principle (MDP), and (ii) those that, in contrast, seek to extract such information from the observations, such as the L-Curve (LC) or Generalized Cross-Validation (GCV) methods. The other alternative method is adaptive regularization (Zhdanov, 2002), which can be considered in the second category. A general review including the advantages and disadvantages of the LC, MDP and GCV approaches can found in literature (e.g. Kilmer and O'Leary, 2001; Farquharson and Oldenburg, 2004). Moreover, several other approaches for selecting regularization parameters exist, and some are reviewed in standard texts (e.g. Vogel, 2002; Aster et al., 2018). In most practical applications, little knowledge about the noise or error in the data measurements is available. To deal with these situations, in the context of potential field inversion methods that do not require a good estimate of the error such as LC and the adaptive regularization techniques are successfully applied (e.g. Farquharson and Oldenburg, 2004; Vatankhah et al., 2014, Rezaie et al., 2016). Further

discussions about the regularization parameter choice methods including the one introduced in the present work will be given in the next chapter.

3.5.6 Optimization Algorithms for L_2–norm Regularized Inversion

In the previous section, the formulation of the general objective function, within the framework of the classical Tikhonov regularization, which promotes smooth solutions is described. Through this objective function, like majority of geophysical inverse problems, the gravity inverse problem is transformed into an optimization problem. Consequently, the standard way to find the solution of the gravity inverse problem is minimization of the objective function for the model parameter $\boldsymbol{\rho}$. In other words, the goal of the inversion procedure becomes to find a model $\boldsymbol{\rho}$ that minimizes the objective function described by equation 3.15. Once the inverse problem has been stated in an optimization framework an appropriate optimization technique should be selected. In this section, a short review of the optimization tools that are used to minimize the L_2–norm regularized objective function (equation 3.15) will be presented.

Depending on the scale of the inverse problem, numerous mathematical optimization methodologies have been proposed and applied to minimize the objective function given in equation 3.15. For small-scale problems, that is when the forward-modelling operator matrix $\boldsymbol{A} \in R^{Nx\,M}$ with M and N relatively small, Generalized Singular Value Decomposition (GSVD), or Singular Value Decomposition (SVD) provide a physically acceptable solution through minimization of equation 3.15 in a computationally convenient form (Chung et al. 2008; Chasseriau and Chouteau 2003). However, these direct solving methods are not computationally feasible for large-scale problems, whether in terms of computational time or memory requirements (Li and Oldenburg, 2003). In large-scale problems, especially for large enough M, it is not possible to carry out the matrix SVD computation and matrix-matrix multiplications can consume more time. Moreover, as M increases, the storage requirements for the appropriate matrices quickly become prohibitive. For these reasons, to overcome the computational challenge iterative minimization methods are more attractive approach. Iterative algorithms such as Gauss-Newton, steepest descent, and conjugate gradient have been widely used for different geophysical inversions to recover physical properties.

As this thesis focuses on the non-smooth inversion algorithms, further discussions about the optimization techniques in the case of smooth inversion approaches are beyond the scope of this work. For a rigorous mathematical treatment of L_2–norm regularized methods, I refer readers to the classical text books in this field (e.g. Menke 1989; Hansen 1999; Aster et al. 2005). In addition, a more extensive background on numerical optimization can be found in Boyd and Vandenberghe (2004), Nocedal and Wright (2006). The next section discusses the concept of non-smooth inversion approaches, including the formulation of its objective function and minimization algorithms.

3.6 **Non-Smooth Inversion**

As previously mentioned, the minimization L_2-norm measure objective function have been widely used in potential filed inverse modelling algorithms (Li and Oldenburg, 1996, 1998; Cella and Fedi, 2012; Paoletti et al., 2013) and are proven to be a powerful tool for the stable inversion of geophysical data. Despite the good stability that can be achieved through such methods, the resulting solutions are typically characterized by smooth features, especially blurred boundaries (Portniaguine and Zhdanov, 1999; Farquharson, 2008). The solutions of the inversion method are smooth in the sense that sharp discontinuities in the recovered model are smoothed out and do not show up well in the inverse solution. So smooth inverse solutions may not able to recover blocky structures, and their results are difficult to interpret in terms of sharp boundaries between the structures.

Even though, smooth solutions are desirable in many applications, they are undesirable in other application where the solutions are known to have discontinuities. Many interesting geological structures, for example ore-bodies, salt flanks, etc., that are the targets of geophysical explorations are not smooth spatially and have non-smooth density distribution. Applying smooth inversion algorithms in such areas where the geology of the study area is known to have sharp discontinuities such as the presence localized bodies might be problematic. To deal with the above-mentioned problem, designing an objective function that use non L_2-norm measures on the stabilizing function has been dominating the literature over the past few decades. In other words, the goal of recovering non-smooth models, which have sharp and localized features, have been accomplished with the use of non-smoothing regularization. The classical

non-smoothing stabilizers are L_1 and L_0 -norm stabilizers. Non-smoothing regularization, through L_1 or L_0 -norm stabilizer, is also known as sparsity regularization and the stabilizers are sparse stabilizers. Hence, hereafter these names are used inter-changeably. From the introduction section, we know that the focus of this thesis is to develop a gravity inversion method which can yield non-smooth solutions. Thus, to provide a good theoretical background to non-smooth inversion the fundamental concepts of sparse regularization methods including its application in geophysical inversion are discussed in the following subsections.

3.6.1 Sparse regularization

Presently, sparse regularization methods are the most developing and promising methods for solving inverse problems arising in various fields of study. Sparse regularization techniques have successfully been applied in many areas, including compressive sensing (Li et al., 2020), signal recovery (Huang and Tran, 2018; Xiang et al., 2019), for image reconstruction (Qi et al., 2015; Li et al., 2019), seismic data inversion (Fang and Zhang, 2014; Liu et al., 2018), for potential field inversion (Vatankhah, et al., 2017; Hu et al., 2019; Feng, et al., 2020; Li and Yao, 2020), to mention only a few. For more detail overview about the applications of sparse regularization techniques the reader is referred to a survey paper by Zhang et al. (2015). Up to now, scholars have proposed a variety of sparsity regularization methods. In geophysical inversion, in terms of the different norms utilized on the stabilizer, the commonly used sparse regularization approaches can be grouped into two categories. The first is sparse regularization with the L_1 -norm, and the second is sparse regularization with the L_0 -norm. These sparsity regularization methods have been widely-used to facilitate the recovery of the sharp and focused images of the subsurface (Portniaguine and Zhdanov, 1999; Vatankhah, et al., 2017; Meng, 2018; Rezaie, 2019). In what follows, the discussion focuses on L_1 and L_0–norm regularization methods.

3.6.2 The L_1–norm regularization

As already highlighted, L_1-norm based stabilizing function is one form of sparse regularization methods. In L_1-norm based regularized geophysical inversion, L_1-norm measure of the model or the spatial derivatives of the model are minimized with L_2 measure of data misfit to recover sharp interfaces and discontinuities in the

subsurface. In geophysical non-smooth regularized inversion, one of the commonly used L_1-norm stabilizing function is L_1-norm of the model parameter. The mathematical form, in the context of gravity inversion (i.e. using $\boldsymbol{\rho}$ as a model parameter), can be written as follows:

$$S_{L_1}(\boldsymbol{\rho}) = \sum_{j=1}^{M} |\rho_j| = \|\boldsymbol{\rho}\|_1 \qquad 3.18$$

Like L_2-norm inversion methods, L_1-norm regularized inversion minimizes an objective function which contains L_1-norm type stabilizing function similar to the one shown in equation 3.18. Substituting equation 3.18, instead of the L_2-norm regularization term, in equation 3.15 the L_1-norm regularized objective function can be given by the following expression:

$$\Phi_{L_1} = ||\boldsymbol{W}_e(\boldsymbol{A\rho} - \boldsymbol{g}^{obs})||_2^2 + \mu^2 \|\boldsymbol{\rho}\|_1 \qquad 3.19$$

Irrespective of the optimization scheme used, most L_1-norm regularized sparse geophysical inversion algorithms seek to minimize an objective function of the form presented in equation 3.19. As previously emphasized, this sparse regularization method is known to have a tendency to recover non-smooth models and has, therefore, been immensely popular in various research fields in recent years. In geophysical research, there have been several inversion algorithms dedicated to the use of L_1-norm regularization, for example, in gravity inversion (e.g., Farquharson, 2008; Vatankhah, et al., 2017), in seismic tomography studies (e.g., Fang and Zhang 2014; Liu et al. 2015), in magnetic inversion (e.g., Utsugi, 2019); in electrical imaging (e.g., Loke et al., 2003).

Another well-known form of L_1-norm based regularization function is the L_1-norm of the gradient of model parameter, also known as Total Variation (TV) regularization (Rudin et al., 1992). Mathematically, the TV regularization function can be expressed as:

$$S_{TV}(\boldsymbol{\rho}) = \sum_{j=1}^{M} |\nabla \rho_j| = \|\boldsymbol{\nabla\rho}\|_1 \qquad 3.20$$

where ∇ is the gradient operator. The TV stabilizing functional given by equation 3.20 is not differentiable at zero. To avoid this singularity at zero Acar and Vogel (1994) introduced a modified TV stabilizing functional which is given as:

$$S_{\beta TV}(\boldsymbol{\rho}) = \sum_{j=1}^{M} \left(\sqrt{|\nabla \rho_j|^2 + \beta^2} \right) \qquad 3.21$$

The TV regularization method is also an alternative candidate of non-smooth stabilizer in recovering discontinuities in physical-property distribution. This regularization scheme has been extensively applied in image processing (Vogel and Oman, 1998; Babacan et al., 2009; Wu et al., 2019). The TV stabilization has also been used by many researchers in several regularized geophysical inversion algorithms. For example, to estimate a density-contrast distribution from gravity data inversion (Bertete-Aguirre et al. 2002; Vatankhah et al., 2018), to obtain depth-to-basement estimates from gravity inversion (Martins et al., 2011), in full-waveform seismic inversion (Peters and Herrmann, 2017; Esser et al., 2018), in seismic tomography studies (Loris and Verhoeven, 2012; Jiang and Zhang, 2017) and many others. However, Portniaguine and Zhdanov (1999) pointed out that TV regularization is still weak in describing the sharp boundaries between different geological formations.

In summary, according to the above discussion, in L_1-norm type regularized inversion the objective function Φ_{L_1} consists of L_1 measure of the model or the spatial derivatives of the model and L_2 measure of misfit are minimized to obtain the model parameters of the subsurface. Unlike the L_2-norm regularization, this regularization method imposes lesser smoothness on the obtained solution and hence, used to recover non smooth models. The other advantage of L_1-norm regularization is that, though it is not straight forward as L_2-norm regularization, it can be reformulated as a linear program and thus easily solved by standard optimization techniques (Rish and Grabarnik, 2014). Nevertheless, unlike for L_2-norm minimization they cannot be expressed in a linear form and standard gradient based techniques cannot be directly applied in minimization of L_1-norm regularized inversion algorithms.

3.6.3 The L_0–norm Regularization

In the last decades, L_0–norm has been implemented extensively in various areas of inverse modelling algorithms and received considerable attention in literature. The L_0–norm is commonly defined as the number of nonzero elements in a vector. More references on current developments on L_0–norm, and also for tutorials and application examples, the readers are referred to the online repository available at the Rice University website (3http://dsp.rice.edu/cs.), and to other online resources (e.g. at http://nuit-blanche.blogspot.com). Moreover, there are several recent books that focus on particular aspects of the L_0–norm sparse representation and its applications in various areas (e.g. Elad, 2010; Rish and Grabarnik, 2014)

The popular L_0–norm type sparse stabilizer is the L_0–norm of the model parameter which can expressed as:

$$S_{L_0}(\boldsymbol{\rho}) = \|\boldsymbol{\rho}\|_0 \qquad 3.22$$

Analogous to the L_1–norm regularized objective function presented in equation 3.19, using equation 3.22 as a stabilizer, we arrive at the following form of L_0–norm regularized objective function:

$$\Phi_{L_0} = ||\boldsymbol{W}_e(\boldsymbol{A\rho} - \boldsymbol{g}^{obs})||_2^2 + \mu^2\|\boldsymbol{\rho}\|_0 \qquad 3.23$$

Minimization of Φ_{L_0} (equation 3.23) type formulation of the objective function has received considerable attention in the literature and emerged as an important method in many real-world applications. For example, it was used for face recognition (Fan et al., 2015), for signal recovery (Wang et al., 2018; Xiang et al., 2019), for image reconstruction (Wei, et al., 2018; Li et al., 2019) and feature selection (Han et al., 2015). For further detail about the applications of L_0–norm based regularized objective function, the readers are referred to the review papers by Zhang et al. (2015) and Marques et al. (2018). Minimization of L_0–norm type regularized objective function (equation 3.23) has also been widely applied geophysical data processing and inversion and attracted much attention in recent years. For instance, it was utilized in the seismic data inversion (Chen et al., 2013; Liu et al., 2018), for potential field inversion (Zhao et al., 2016; Meng, 2018; Hu et al., 2019; Feng et al., 2020) and many others. Taking

this into account and for the reasons described well in subsection 3.6.4 the present thesis implements the L_0–norm regularization approach.

3.6.4 Optimization Algorithms in Sparsity Regularized Inversion

In order to apply sparse recovery approaches in practice, efficient algorithms are required that solve the optimization problem (i.e. minimization of the sparsity regularized objective function). Several sparse recovery algorithms have been proposed by researchers in the last years. Focusing will be given to iteratively re-weighted least squares algorithm one of the widely known approaches, which will be utilized in the current work. This section presents a detailed explanation of the basic concepts of some of the most popular algorithms. The explanations serve in particular as fundamental for the presented work in the next chapter.

Equations 3.19 and 3.23 represent the two commonly adopted formulations of sparse regularization in inverse problems. Minimization of these equations constitutes the main idea of sparse recovery optimization. It is well-known and already stated that, inversion algorithms that employ minimization of such sparsity regularized objective functions yield sparse and focused images of the subsurface structures. For this reason, these have been extensively used in several geophysical inversion algorithms, particularly when it can be assumed that the subsurface targets are localized and compact and/or have sharp edges (Farquharson, 2008; Chen et al., 2013; Sun and Li 2014; Rezaie et al., 2016; Vatankhah et al. 2017, Utsugi, 2019).

Clearly, dealing with L_1-norm regularization is substantially easier. This is because the objective function in equation 3.19 is a convex and its derivatives can be easily obtained (Wang et al. 2013). Consequently, there are efficient and accurate numerical solvers that can deal with such problems (Daubechies et al., 2004; Donoho, 2006 Schmidt et al., 2007). However, it is well-known that the L_1- norm stabilizer is not the sparsest norm and hence the obtained result is not sparsest solution. To deal with this situation, a widespread and successful approach is the use L_0-norm regularized objective function (equation 3.23). The reason for this is that the L_0-norm of a vector, defined as the number of its nonzero elements, measures the sparsity of a vector more appropriately. Additionally, previous investigations have demonstrated that the L_0-

norm stabilizer can yield a sparser solution than that obtained using the convex L_1-norm stabilizer (Chartrand, 2007; Fournier, 2015; Vatankhah et al., 2020). It was already noted that the intent of this work is to develop gravity inversion algorithm which yields sharp and compact image. Thus, considering the above-mentioned benefits the current study uses L_0-norm based regularization. Consequently, hereafter the main focus is to discuss the optimization methods that have been developed to solve L_0 –norm regularized objective function (equation 3.23).

While minimization of equation 3.23 delivers the sparsest solutions, it is well known that solving L_0-norm minimization leads to a Nondeterministic Polynomial (NP) complex problem in combinatorial optimization, which indicates that optimization algorithms solving the problem cannot be completed in polynomial terms (Mohimani et al. 2009; Cui, Zhang and Lu 2010; Wang et al. 2013; Qiu et al. 2014). Hence, it is very difficult to directly find the solution with the L_0-norm minimization. This is due to the presence of the L_0-norm, which is not convex (Boyd and Vandenberghe, 2004). To overcome this issue, several approximate optimization approaches have been developed by researchers and employed successfully in variety of applications. Here, these optimization approaches will be discussed, focusing on the one that will be implemented in the next chapter. For more detail description about L_0-norm based sparse optimization methods and their possible applications, the reader can refer to the review papers by Zhang et al. (2015); Marques et al, (2018), and the references therein.

As it was mentioned above, the minimization Φ_{L_0} defined in equation 3.23 is NP-hard problem, consequently it is very difficult to directly find the solution. Therefore, approximate solution methods are necessary. Numerous approximate minimization algorithms have been developed and employed successfully. The developed minimization algorithms are usually classified into three main categories (Carmi et al., 2014):

(1) Greedy algorithm.

(2) Convex relaxation algorithm.

(3) Non-convex relaxation algorithm.

The most popular approaches in the greedy algorithms are the Matching Pursuit (MP) (Cotter and Rao, 2002; Do et al., 2008), Orthogonal Matching Pursuit (OMP) (Wang et al., 2012; Wen et al., 2016), Compressed Sampling Matching Pursuit (CoSaMP) (Needell and Tropp, 2010), and Regularized Orthogonal Matching Pursuit (ROMP) (Needell and Vershynin, 2010). The disadvantage of greedy algorithm is that it is sensitive to noise (Wang et al., 2018; Wang et al., 2019). For this reason and as it is not used in the present work, this method will not be discussed in detail.

The main idea of convex relaxation algorithm is to replace the non-convex L_0-norm with approximate convex function that is easier to solve. In other words, this approach seeks convex approximate reformulation of the non-convex problem. The popular convex relation approach is to replace the L_0-norm with L_1-norm which relaxes the non-convex L_0-norm regularization into the convex L_1-norm regularization. Then solve the minimization using convex minimization algorithms such as: Basis Pursuit (BP) (Che et al., 2001; Ekanadham et. al), Least Absolute Shrinkage and Selection Operator (LASSO) (Tibshirani, 2011), Basis Pursuit Denoising (BPDN) (Zibulevsky and Elad, 2010).

The non-convex relaxation algorithms seek non-convex approximate reformulations of the L_0-norm function. That is relax the L_0-norm problem to a related non-convex problem and then attempt solve it. Non-convex relaxation minimization algorithms includes the FOcal Underdetermined System Solver (FOCUSS) (Gorodnitsky and Rao, 1997; He et al., 2008), Bayesian approach (Kolehmainen et al., 2012; Oliveri et al., 2017), Iterative Re-weighted Least Squares (IRLS) (Daubechies et al., 2010; Lai et al., 2013). Among these algorthms the IRLS algorithm is an efficient and easy-to-implement (Scales et al.1988; Trad, et al., 2003; Chen et al., 2013). Accordingly, IRLS has been suggested as an attractive alternative in the literature and it is frequently implimented. Taking this into account, the present work applies IRLS algorithm. Consquently, in section 3.8 I will recall the fundamental IRLS concept and in Chapter 4 an IRLS algorithm developed in this thesis to find the solution of eqaution 3.23 will be presented.

Recently, the relaxation methods are the most widely applied methods in inverse problems, which uses non-smooth regularization with L_0-norm penalization, arising in

various areas. The relaxation approaches reformulate Φ_{L_0}, in equation 3.23, to the following expression (Huang and Tran, 2018):

$$\Phi_{FL_0} = ||\boldsymbol{W}_e(\boldsymbol{A\rho} - \boldsymbol{g}^{obs})||_2^2 + \mu^2 F(\boldsymbol{\rho}) \qquad 3.24$$

where $F(\boldsymbol{\rho})$ is a suitable stabilizing function which replaces $\|\boldsymbol{\rho}\|_0$ depending on the desired relaxation type. For example, we can get a non-convex relaxation of equation 3.23 by selecting $F(\boldsymbol{\rho})$ to be some approximate function that is non convex. A proper $F(\boldsymbol{\rho})$ is critical to the success of the sparse solution: it should favor sparse solutions, and the corresponding problem Φ_{FL_0} can be solved efficiently (Huang and Tran, 2018). In other words, the relaxed alternative objective function (Φ_{FL_0}) should be able to quantify the sparsity level of $\boldsymbol{\rho}$ and easy to optimize (Hurley and Rickard, 2009).

In the case of convex relaxation approach, as noted earlier, the most widely used form of $F(\boldsymbol{\rho})$ is L_1-norm stabilizer, which relaxes the L_0-norm regularization into the L_1-norm regularization. Though the L_1-norm is the best convex approximation of the L_0-norm this only holds in noiseless data cases. If the data is noisy then they are not exactly equivalent to the L_1-norm (Xiang et al., 2018). Moreover, there is already quite a lot of evidence that non-convex regularization terms can provide better reconstruction results than convex regularization functions (Wang, 2020). Accordingly, the present thesis applies the non-convex relaxation of L_0-norm regularization. For this reason, the following section focuses on different forms of F($\boldsymbol{\rho}$) that have been proposed for non-convex relaxation of the L_0-norm regularization.

3.7 Approximate L_0–norm Sparce stablizers

In the last decades, several different forms of F($\boldsymbol{\rho}$), which approximates the L_0–norm, have been proposed and broadly utilized in many fields. Particularly, this subsection focuses on different forms of F($\boldsymbol{\rho}$) proposed in the literature and applied in potential field inversion algorithms as a stabilizing functional to obtain compact or focused images of the subsurface.

Last and Kubik (1983) introduced L_0–norm type stabilizer as a compactness constraint, for the recovery of a compact gravity model, which is expressed as:

$$\mathrm{F}_C(\boldsymbol{\rho}) = \sum_{j=1}^{M} \frac{\rho_j^2}{\rho_j^2 + \varepsilon} \qquad 3.25$$

where ε is a focusing parameter. This approximate L_0–norm has been borrowed by other researchers in various branches of geophysics (Ajo-Franklin et al., 2007; Stocco et al., 2009; Rezaie, et al., 2017b; Feng et al., 2020). The compactness constraint $\mathrm{F}_C(\boldsymbol{\rho})$ is further developed by Portniaguine and Zhdanov (1999) through the addition of prior model information, leading to the minimum support constraint ($F_{MS}(\boldsymbol{\rho})$). Modifying equation 3.25 by introducing the prior model $\boldsymbol{\rho}^{apr}$ yields:

$$F_{MS}(\boldsymbol{\rho}) = \sum_{j=1}^{M} \frac{\left(\rho_j - \rho_j^{apr}\right)^2}{\left(\rho_j - \rho_j^{apr}\right)^2 + \varepsilon} \qquad 3.26$$

The $F_{MS}(\boldsymbol{\rho})$ function has been successfully used in varies geophysical inversion schemes (e.g. Portniaguine and Zhdanov, 2002; Zhdanov et al., 2004).

To recover focused inversion images Portniaguine and Zhdanov (1999) proposed a minimum gradient support ($F_{MGS}(\boldsymbol{\rho})$) stabilizer, which minimizes the area where a strong model parameter variations and discontinuity occur. Following Zhdanov (2002) the discrete form of the minimum gradient support stabilizer is defined as follows:

$$F_{MGS}(\boldsymbol{\rho}) = \sum_{j=1}^{M} \frac{\nabla\left(\rho_j - \rho_j^{apr}\right).\nabla\left(\rho_j - \rho_j^{apr}\right)}{\nabla\left(\rho_j - \rho_j^{apr}\right).\nabla\left(\rho_j - \rho_j^{apr}\right) + \varepsilon} \qquad 3.27$$

The minimum gradient support functional $F_{MGS}(\boldsymbol{\rho})$ has been implemented by many researchers for example Zhang et al. (2012) used to invert 2-D and 3-D magnetotelluric (MT) data and obtained clear images of geo-electrical interfaces, Zhdanov (2009) applied the $F_{MGS}(\boldsymbol{\rho})$ functional to invert gravity and EM data, Čuma et al. (2012) applied the $F_{MGS}(\boldsymbol{\rho})$ to a 3D inversion of potential field data, to mention only few.

Based on the exponential varying property of the inverted model parameters Zhao et al. (2016) proposed an exponential type stabilizing functional ($F_{EX}(\boldsymbol{\rho})$) that can generate a focused inversion image. The $F_{EX}(\boldsymbol{\rho})$ stabilizing functional is defined as:

$$F_{EX}(\boldsymbol{\rho}) = \sum_{j=1}^{M}\left(1 - e^{-\left|\rho_j - \rho_j^{apr}\right|}\right) \quad 3.28$$

Zhao et al. (2016) applied this stabilizing functional to invert gravity and magnetic data, and a case study results proved its effectiveness in recovering the sharp boundary of the anomalous bodies. Wang et al. (2019) used the exponential stabilizer proposed by Zhao et al. (2016) for focusing inversion of MT data.

To obtain a sharp-boundary and still a well-focused image in the 3D focusing inversion, Hu et al. (2019) proposed an adjustable exponential stabilizing functional ($F_{AES}(\boldsymbol{\rho})$), based on the exponential stabilizer $F_{EX}(\boldsymbol{\rho})$, which is given in equation 3.28. The adjustable exponential stabilizing functional ($F_{AES}(\boldsymbol{\rho})$) is determined by the following expression:

$$F_{AES}(\boldsymbol{\rho}) = \sum_{j=1}^{M}\left(1 - \varepsilon_1^{-\varepsilon_2(\rho_j - \rho_j^{apr})^2}\right) \quad 3.29$$

where ε_1 in the base and ε_2 in the exponent are focusing parameters. Hu et al. (2019) applied this $F_{AES}(\boldsymbol{\rho})$ to 3D field and synthetic gravity and magnetics data and the inversion recovered focused images with sharp boundaries.

Based on the idea of approximation, Mohimani et al. (2009) employed the Gauss function to approximate the L_0-norm. The mathematical form of the approximate L_0-norm Gauss function ($F_G(\boldsymbol{\rho})$) is written as:

$$F_G(\boldsymbol{\rho}) = \sum_{j=1}^{M} exp^{-\left(\frac{\rho_j^2}{2\sigma^2}\right)} \quad 3.30$$

where σ is a parameter to control the degree of the smoothness and sharpness of $F_G(\boldsymbol{\rho})$. When σ is a small enough positive value, the Gauss function is almost equal to the L_0-norm. This function has been used by a number of researchers for signal and image recovery (e.g. Mohimani et al., 2009; Ye et al., 2013; Guo et al., 2017). Meng, et al. (2018) used the $F_G(\boldsymbol{\rho})$ function as a sparsity stabilizer in 3D gravity inversion to determine the subsurface density distribution with a clear boundary. Meng (2016) adopted and reformulated the $F_G(\boldsymbol{\rho})$ function to a hyperbolic tangent function to

approximate the L_0–norm. The approximation of L_0-norm with hyperbolic tangent function ($F_{HT}(\boldsymbol{\rho})$) can be expressed as follows:

$$F_{HT}(\boldsymbol{\rho}) = \sum_{j=1}^{M} \frac{e^{\frac{\rho_j^2}{2\sigma^2}} - e^{-\frac{\rho_j^2}{2\sigma^2}}}{e^{\frac{\rho_j^2}{2\sigma^2}} + e^{-\frac{\rho_j^2}{2\sigma^2}}} = \sum_{j=1}^{M} tanh\frac{\rho_j^2}{2\sigma^2} \qquad 3.31$$

Meng (2016) applied this hyperbolic tangent function $F_{HT}(\boldsymbol{\rho})$ for 3D inversion of gravity gradient tensor data. In addition, Meng (2018) developed a 3D potential field data inversion algorithm, with the aim of obtaining blocky inversion results, by using $F_{HT}(\rho)$ as quasinorm sparse constraint.

Another approach to obtain focused inverse models with sharp boundaries was considered by Ramos, et al. (1999) who introduced entropic regularization method based on entropy stabilizing functional. They applied this regularization method for non-smooth 2D inversion of magneto telluric data. In addition, the entropic stabilization method was used in 2D MT data inversion (Candansayar, 2008), in apparent density mapping (Silva et al., 2007) and for the inversion of gravity data (Silva et al., 2010; Woodbury, 2011; Rezaie, 2019). Following Ramos et al. (1999) and Rezaie (2019) the zero order minimum entropy stabilizing functional ($F_{EN}(\boldsymbol{\rho})$) can be expressed as:

$$F_{EN}(\boldsymbol{\rho}) = \sum_{j=1}^{M} \frac{(|\rho_j| + \delta)}{Q} \ln\left(\frac{(|\rho_j| + \delta)}{Q}\right) \qquad 3.32$$

where δ is a small positive value in the order of 10^{-15}, which is used to avoid singularity and $Q = \sum_{j=1}^{M}(|\rho_j| + \delta)$.

The other alternative sparsity-promoting regularization to relax the L_0-norm is an L_p-norm (where $0 < p < 1$). In this case, the L_p-norm stabilizing functional ($F_{L_p}(\boldsymbol{\rho})$), which is used to replace $\|\boldsymbol{\rho}\|_0$ in equation 3.23, can be defined as follows:

$$F_{L_p}(\boldsymbol{\rho}) = \|\boldsymbol{\rho}\|_p^p \quad \text{where } 0 < p < 1 \qquad 3.33$$

In this regard, it should be noted that different approximate formulation of $\|\boldsymbol{\rho}\|_p^p$, presented in section 3.4 are used to replace the L_0-norm. In recent years, many scholars have shown that using the non-convex L_p-norm, with the power p valued in the range of $0 < p < 1$, to relax the L_0-norm is a better choice than using L_1-norm, and has

attracted much attention and has been verified in a number of studies such as in Chen et al., (2010) and Lai and Wang (2011). The L_p-norm ($0 < p < 1$) regularized sparse optimization has been widely applied in signal and image processing and in geophysical inverse problems. For example, in seismic reflectivity inversion (Li et al., 2017; Li et al., 2018), for sparse reconstruction of electrical impedance tomography (Wang, 2020), in medical image reconstruction scheme (Wang, et al., 2017; Gao et al., 2019), and many others.

In general, out of the different forms of $F(\rho)$ which are described above the compactness constraint $F_C(\rho)$ (Last and Kubik, 1983) also known as the minimum support stabilizer $F_{MS}(\rho)$ (Portniaguine and Zhdanov, 1999; Zhdanov, 2002) is one of the most popular stabilizing functions for non-smooth inversion of geophysical data. It was successfully used by different researchers for example Čuma et al. (2012), Zhdanov et al. (2014), Fei et al. (2018), Rezaie et al. (2016), Ji et al. (2019), Feng et al. (2020). This stabilizer is known to yield a compact and focused geophysical model with sharp boundaries (Rezaie et al., 2016). As indicated earlier, the aim of this PhD research is to develop a gravity inversion algorithm that can generate a compact model with sharp edges, and hence the minimum support stabilizer is utilized.

3.8 **Iterative Re-weighted Least Squares Algorithm (IRLS)**

In the present section a brief review of the IRLS Algorithm, which is the central part of the inversion algorithm, will be presented in the next chapter. The IRLS algorithm was originally presented in the doctoral thesis of Lawson in 1961. Since then IRLS algorithm has been extensively studied and extended by many scholars (Gholami and Gheymasi, 2016; Wang et al., 2019; Zhou and Yu, 2019). The reader is refered to the paper by Ochs et al. (2015) for an updated and rather general view about IRLS algorithm. Discussions about the stability and convergence of the IRLS algorithm from both theoretical and empirical point of view also exist in literature (Wolke and Schwetlick, 1988; O'Leary, 1990; Farquharson and Oldenburg, 1998; Ba et al., 2013; Cai and Li, 2017). The core idea of IRLS algorithm, in L_0-norm regularized minimization, is to replace L_0-norm with re-weighted L_2-norm and find the approximate solution via updating weights iteratively. In other words, at each iteration of an iterative scheme, the L_0-norm is approximated by the weighted L_2-norm using the model obtained from the previous iteration to construct the weights for the next

iterations. Accordingly, the L_0-norm regularized objective function (similar to the one shown given in equation 3.23 is transformed into a weighted least square problem.

In recent years, IRLS has become a standard minimization method and it has been applied by many researchers in different fields. In mathematical statistics for robust regression, the reader is refferred to O'Leary (1990) for a survey on IRLS methods applied to robust regression. In signal and image processing, IRLS has been used as a technique to build algorithms for sparse reconstruction (Chartrand and Yin, 2008; Saab et al., 2008; Carrillo and Barner, 2009; Wei et al., 2018). The IRLS has been also successfully used in various geophysical inversion methods such as seismic tomographic inversion (Scales et al., 1988; Ajo-Franklin et al., 2007), in magnetic inversion (Barbosa and Silva, 2006; Stocco et al., 2009; Li and Yao, 2020), in gravity data inversion (Last and Kubik, 1983; Silva and Barbosa, 2006; Farquharson, 2008).

3.9 **Summary**

In this chapter, the general principles and theory of the geophysical inversion methods focusing on gravity inverse problem have been described. First, I briefly described geophysical inverse problem and fundamental concepts of regularization in geophysical inversion including its mathematical framework. Secondly, the different measures of the length of a vector are well discussed. Thirdly, I reviewed smooth potential field inversion algorithms, which uses the L_2-norm stabilizer, with their associated objective function and the methods of minimizing the objective function. Then I have discussed the non-smooth potential field inversion algorithms. Simultaneously, I reviewed sparse (L_1-norm and L_0-norm) regularization approaches, and several sparse optimization algorithms that promote compact and non-smooth solutions. In particular, I explained the IRLS algorithm for minimization of L_0-norm regularized objective function Φ_{L_0}. Additionally, I introduced several different forms of approximate functions that have been proposed, to deal with the L_0-norm sparse regularization. In summary the L_0-norm regularization can aid the recovery of compact and sharp models in gravity inversion and the goal of this research is to develop a method that makes use of this regularization approach. In the following chapter, the development of the newly proposed gravity inversion algorithm, which makes use of the theory discussed in this chapter will be presented.

CHAPTER 4: A NEW APPROACH TO COMPACT GRAVITY INVERSION ALGORITHM

4.1 Introduction

Geophysical inversion is the process of constructing a model that can explain the cause of a set of measurements by using different mathematical modelling techniques. Particularly, as noted in previous chapters, the principal aim of gravity data inversion in geophysical exploration is to estimate the density distribution and geometrical properties (i.e. shape and location) of the causative bodies in the subsurface of the Earth. Thus, inversion of gravity data constitutes an important step in the quantitative interpretation since the reconstruction of density contrast models markedly increases the amount of information that can be extracted from the gravity data. Nevertheless, there are well-known major problems in gravity inverse modelling, which are already described with detail in chapter 1 such as non-uniqueness of the solution, lack of depth resolution, and insatiability of the process. The standard way to overcome these difficulties and solve an ill-posed gravity inverse problem, according to the regularization theory (Tikhonov et al., 2013; Zhdanov, 2015), is a minimization of a general objective function which consists of the data fidelity or misfit functional and stabilizing functional stabilizer term.

In chapter 3, I have discussed the fundamental concepts of regularization in geophysical inversion including its mathematical framework. I have also briefly described the smooth and non-smooth potential field inversion algorithms with their associated objective functions and the minimization methods. Predominantly, in subsection 3.6.1, I reviewed sparse regularization approaches and several sparse optimization algorithms that promote sparse and blocky solutions. In general, I have discussed the theory needed to solve the inverse problem specifically focusing on the concepts related to non-smooth inversion algorithms. This is important as it provides a solid foundation for the gravity inversion algorithm presented in the current chapter.

This chapter, presents a gravity inversion method that can produce compact and sharp models of the subsurface density distribution, to assist the recovery of non-smooth, blocky geologic features with sharp boundaries. The presented approach is based on the minimization of an objective function, which consists of data misfit and

L_0-norm stabilizing functions, by IRLS algorithm. Python programs that are written to implement the presented gravity inversion algorithm in this chapter have the following new contributions which can also be incorporated in other inversion approach for further advancements. The first two are an auto-adaptive regularization parameter estimation technique and an error weighting function that can improve the fast convergence of the method while keeping its stability. The second is a new depth weighting function to counteract the natural decay of the gravity kernel so that the inversion process can provide realistic depth information without giving emphasis to shallow structures. The advantage of the newly introduced depth weighting function is that its parameters can be determined automatically and they are not subjected to the interpreter judgment. The other improvement, that helps to obtain a physically meaningful model with more realistic geological meaning, is the implementation of the element by element physical inequality constraint algorithm. With this physical constraint algorithm facility multiple, complex, and closely placed anomalous bodies with different density contrasts can be delineated. Perhaps the other important contribution of this chapter is on the implementation of combined stopping criterion to terminate the iterative process after an appropriate number of steps. In the following sections, the features of the proposed algorithm are presented in detail.

4.2 **The Objective Function**

In this section, the objective function that has been used in the current work and the motivation for using it will be discussed. As it has been discussed in Chapter 3, the minimization of the L_0-norm regularization objective function is well-known to yield compact or focused and sharp images of the subsurface. For this reason, it has been extensively used in several geophysical inversion algorithms, particularly when it can be assumed that the subsurface targets are localized and compact and/or have sharp edges. It was already mentioned that the intent of this chapter is to develop a gravity inversion algorithm that can produce compact and sharp images and hence L_0-norm regularized objective function is an appropriate choice. Recalling from chapter 3, the L_0-norm regularized objective function minimized to obtain the density model $\boldsymbol{\rho}$ in the present inversion scheme is given by:

$$\Phi_{L_0} = ||\boldsymbol{W}_e(\boldsymbol{A\rho} - \boldsymbol{g}^{obs})||_2^2 + \mu^2 \|\boldsymbol{\rho}\|_0 \qquad 4.1$$

An efficient algorithm is required that solve the optimization problem (i.e. minimization of the L_0-norm regularized objective function). As it was mentioned in section 3.6.4, it is well-known that the minimization of Φ_{L_0}, defined in equation 4.1, is Nondeterministic Polynomial (NP) complex problem. Consequently, it is very difficult to directly find a solution (Mohimani et al. 2009; Chen et al., 2013; Wang et al. 2013). This is because of the presence of the L_0-norm term ($\|\boldsymbol{\rho}\|_0$), which is not convex (Boyd and Vandenberghe, 2004). To overcome this issue, several approximate L_0-norm functions have been developed and employed successfully in a variety of applications (see section 3.7). The following section describes the approximate L_0-norm function implemented in the present work to replace $\|\boldsymbol{\rho}\|_0$ term in equation 4.1.

4.3 The L_0–norm Compactness Constraint

Approximate expressions are usually used to convert the L_0-norm into an equivalent norm for the suitability of computation. Accordingly, several forms of L_0-norm approximate stabilization functions, that have been proposed and implemented in inversion of potential field algorithms, were discussed in section 3.7. Among the different forms of L_0-norm type stabilizers, the compactness constraint introduced by Last and Kubik (1983) seeks to minimize the area (in 2D) or volume (in 3D) occupied by the causative body. This stabilizer is further developed by Portniaguine and Zhdanov (1999) who used the term "minimum support stabilizer", and is one of the most popular and successfully implemented L_0-norm stabilizing function (Čuma et al., 2012; Zhdanov et al., 2014; Fei et al., 2018; Ji et al., 2019). As this stabilizer does not penalize sharp or blocky features, it is a suitable stabilizer for non-smooth geologic structures such as faults, dikes, or cavities which have properties that are relatively localized within the area under consideration. In other words, as it was demonstrated by a number of researchers (e.g. Zhdanov 2002, Rezaie et al., 2016; Feng et al. 2020), this stabilizer is known to yield a compact or focused geophysical model with sharp boundaries effectively. This suggests that the minimum support stabilizer is a suitable choice with which to obtain the desired solutions in accordance with the aim of this Ph.D. research (i.e. to develop a gravity inversion algorithm that can generate a compact model with sharp edges). Therefore, the minimum support stabilizer is utilized in this work.

Equation 3.26, repeated below, defines the minimum support stabilizer:

$$F_{MS}(\boldsymbol{\rho}) = \sum_{j=1}^{M} \frac{\left(\rho_j - \rho_j^{apr}\right)^2}{\left(\rho_j - \rho_j^{apr}\right)^2 + \varepsilon} \qquad 4.2$$

Usually a prior model $\boldsymbol{\rho}^{apr}$ may not be available and hence the requirement of the prior model can be circumvented by setting $\boldsymbol{\rho}^{apr} = 0$. Then modifying equation 4.2 using $\boldsymbol{\rho}^{apr} = 0$ yields the L_0–norm compactness stabilizer given in equation 4.3.

$$F_C(\boldsymbol{\rho}) = S_{CL_0}(\boldsymbol{\rho}) = \sum_{j=1}^{M} \frac{\rho_j^2}{\rho_j^2 + \varepsilon} \qquad 4.3$$

In equations 4.2 and 4.3 ε is a focusing parameter and methods for the selection of a suitable ε are discussed later. Using the function in equation 4.3 as stabilizing functional in the objective function (like the one in equation 4.1) is equivalent to using L_0-norm based stabilization (Sun and Li, 2014). Thus, by substituting equation 4.3 into equation 4.1, one can arrive at the following expression for the L_0-norm regularized objective function:

$$\Phi_{L_0} = ||\boldsymbol{W}_e(\boldsymbol{A\rho} - \boldsymbol{g}^{obs})||_2^2 + \mu^2 \sum_{j=1}^{M} \frac{\rho_j^2}{\rho_j^2 + \varepsilon} \qquad 4.4$$

Equation 4.4 represents the L_0-norm stabilized objective function minimized to obtain the desired solution in this work. The minimization procedure will be described in section 4.4

4.3.1 The focusing parameter

The focusing parameter ε is a very important parameter for both minimum support and compactness constraint L_0–norm type stablizers. Its main purpose is to avoid singularities (for example as $\rho_j \to 0$ in equation 4.3 and to provide stability. The parameter ε is a small number and in general we are interested in the case where parameter $\varepsilon \to 0$, because its small value leads to very compact models. However, this may introduce instability or unwanted oscillations in the model, especially when noise is present in the data. On the other hand, if ε is chosen large, compactness constraint has no influence on the compactness of the model. To further demonstrate this Figure 4.1 shows the comparison of the compactness constraint in equation 4.3 for different

values of ε. From the figure, we see that as ε becomes large, the compactness constraint function loses its property and behaves more like the minimum length L_2-norm stabilizer (see Figure 3.1) which results in undesirable smoothness in the model though it improves the stability. This also pointed out by Ajo-Franklin et.al (2007) and Zhdanov and Tolstaya (2004).

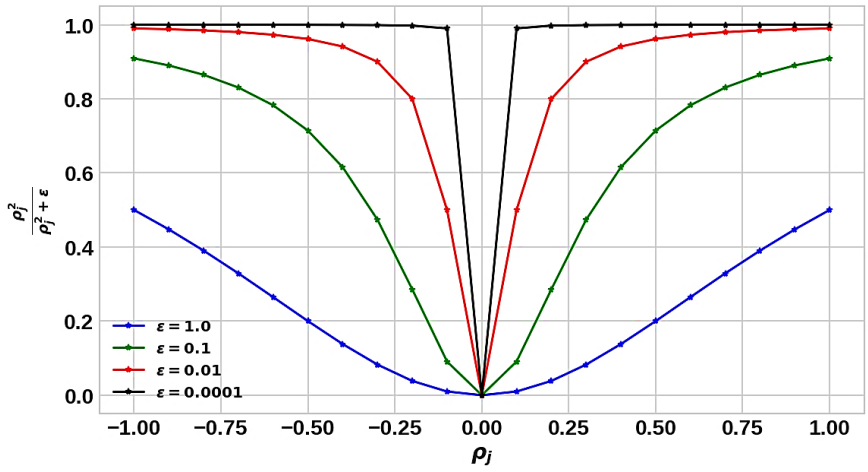

Figure 4.1: Comparison of the compactness stabilizing term defined in equation 4.3 for different values of ε

Based on the above discussions it is very essential to choose an optimal value of ε. In previous studies for instance the pioneering work of Last and Kubik (1983), and Lewi (1997) the parameter ε was assigned a value close to machine precision (10^{-11} to 10^{-15}). Alternatively, Zhdanov and Tolstaya (2004) introduced a trade-off curve method, similar to the L-curve technique, to select ε by computing model objective for the current model estimate over a range of values for ε. However, as pointed out by Ajo-Franklin et al. (2007) setting ε to values near machine precision results in severe instability as $\rho_j \rightarrow 0$ and the approach of Zhdanov and Tolstaya (2004) often yields trade-off curves with poorly defined corners. Therefore, it is better to fix ε at a reasonable value determined by experience, typically between 10^{-4} to 10^{-7} (Ajo-Franklin et al., 2007). Consequently, in the present work based on several numerical simulation tests the value 10^{-6} is assigned for in all inversions.

4.4 L_0–norm Minimization via Re-weighted L_2–norm: IRLS Algorithm

This section presents the optimization procedure implemented in this work to minimize the L_0-norm stabilized objective function in equation 4.4. There are different optimization procedures available to minimize different forms of L_0-norm regularized objective functions (like the one shown in equation 4.4 and some of them reviewed in section 3.6.4. In particular, I recall the effective and easy-to-implement IRLS, briefly reviewed in section 3.8, is one of the most popular techniques. Further, the IRLS has been suggested as an attractive alternative in the literature, and has superior performance in a variety of geophysical inversion methods (e.g. Stocco et al. 2009; Sun and Li, 2014; Gholami and Aghamiry, 2017). In fact, a number of scholars have demonstrated that IRLS is an efficient minimization technique rivaling standard state-of-the-art algorithms (Chartrand and Yin, 2008; Saab et al., 2008; Carrillo and Barner, 2009; Ba et al., 2013). The fundamental idea of this algorithm is to replace the direct solution of the inverse problem by an equivalent iterative procedure having an explicit and unique solution at each iterative step, and the model obtained is used to construct the weights for the next iterations. In the current work, the IRLS algorithm is implemented considering its flexibility advantage and improved convergence. In other words, the L_0-norm minimization problem in equation 4.4 is solved by iteratively re-weighted L_2-norm minimization and it is carried out next paragraphs.

As noted above the IRLS method solves the L_0-norm regularized minimization problem by transforming it to an iterative L_2-norm regularized minimization problem. That is to say, the main step in an IRLS algorithm is replacing L_0-norm with reweighted L_2-norm and finding the approximate solution via updating weights iteratively. Equation 3.15, repeated below, is L_2-norm regularized objective function in matrix form that can be solved in weighted least square sense.

$$\Phi_{L_2} = ||\mathbf{W}_e(\boldsymbol{A\rho} - \boldsymbol{g}^{obs})||_2^2 + \mu^2||\boldsymbol{W}_m(\boldsymbol{\rho} - \boldsymbol{\rho}_F)||_2^2 \qquad 4.5$$

Taking the flexibility advantage offered by IRLS algorithm and using a suitably chosen weighting matrix $\boldsymbol{W}_m$ the solution for equation 4.4 is obtained by minimizing equation 4.5 (Chen et al., 2013; Wang et al., 2019). Accordingly, minimizing the L_2-norm objective function Φ_{L_2} in equation 4.5 using the standard weighted-damped least-

square optimization, which is described in detail in standard texts such as Menke (1989), the estimated density distribution ($\boldsymbol{\rho}^{k+1}$) at $k+1$ iteration in matrix notation can be given by:

$$\boldsymbol{\rho}^{k+1} = \boldsymbol{\rho}_F^k + \left[\left[\boldsymbol{W}_m{}^k\right]^{-1}\boldsymbol{A}^T(\boldsymbol{A}[\mathbf{W}_m^k]^{-1}\boldsymbol{A}^T + (\mu^2)^k[\boldsymbol{W}_e^k]^{-1})^{-1}\boldsymbol{g}_r^k\right] \qquad 4.6$$

where $\boldsymbol{\rho}_F^k$ is the k^{th} iteration reference density vector, which is from prior information or calculated at each iteration. $\boldsymbol{g}_r^k = \boldsymbol{g}^{\boldsymbol{obs}} - \boldsymbol{A}\boldsymbol{\rho}_F^k$ represents the residual data vector computed at each iteration. The computation of $\boldsymbol{\rho}_F^k$ and $\boldsymbol{W}_e^{\mathrm{k}}$ will be explained in detail in sections 4.8 and 4.5 respectively. Here, $\boldsymbol{W}_m^k$ is a product of three different diagonal matrices such as the L_0-norm compactness stabilizer $\left(\boldsymbol{W}_{L_o}^k\right)$, hard constraint $\boldsymbol{W}_h^k$, and depth weighting $\boldsymbol{W}_{zn}$. Mathematically, $\boldsymbol{W}_m^k$ can be expressed as follows:

$$\boldsymbol{W}_m^k = \boldsymbol{W}_{L_0}^k \boldsymbol{W}_{zn}\, \boldsymbol{W}_h^k \qquad 4.7$$

More details regarding the matrices $\boldsymbol{W}_h^k$ and $\boldsymbol{W}_{zn}$ will be provided in sections 4.8 and 4.7 respectively. The L_0-norm compactness stabilizing matrix $\boldsymbol{W}_{L_0}^k$ depends on model parameter and computed at each iterative step. Application of the L_0 –norm compactness constraint (equation 4.3) as stabilizer leads to the following choice of compactness constraint weighting matrix $\boldsymbol{W}_{L_0}^k$ which is explicitly given by (Last and Kubik, 1983):

$$\left[\boldsymbol{W}_{L_o}{}^k\right]_{jj}^{-1} = \left[\rho_j^k\right]^2 + \varepsilon \qquad 4.8$$

where ε is again focusing parameters discussed in subsection 4.3.1. In all inversions considered in the present work based on several numerical experiments the value of ε is assigned to be 10^{-6}. Updating the matrix $\boldsymbol{W}_{L_0}^k$ (equation 4.8) at each iteration and applying in the regularized least square solution (equation 4.6), is exactly equivalent to minimization of objective function with L_0-norm stabilizer in equation 4.4 (Sun and Li, 2014). That is to say, L_0-norm stabilization that leads to compact and sharp solution is implemented using $\boldsymbol{W}_{L_0}^k$.

4.5 **Error Weighting**

The focus of this section is to introduce a new error weighting matrix which plays a very important role in improving the stability of the current inversion method. In the context of the compact gravity inversion scheme, as suggested by Last and Kubik (1983), the error weighting matrix $\boldsymbol{W}_e^k$ computed at each iteration and it is given by:

$$\boldsymbol{W}_e^k = \boldsymbol{diag}\left(\boldsymbol{A}\left[\boldsymbol{W}_{L_o}{}^k\right]^{-1}\boldsymbol{A}^T\right) \tag{4.9}$$

where $\boldsymbol{diag}$ stands for diagonal. This expression is used by money authors (e.g. Guillen and Menichetti, 1984; Barbosa and Silva, 1994; Stocco et al., 2009; Ghalehnoee et al., 2016). Nevertheless, some instability was reported by Lewi (1997) in using $\boldsymbol{W}_e^k$ together with compactness weighting in scenarios such as complicated geological geometry and when the data is contaminated with error. To overcome this issue, Lewi (1997) proposed to put the term $(\mu^2)^k[\boldsymbol{W}_e^k]^{-1}$ in equation 4.6 as $\frac{(\delta_\rho^2)^k}{1+(\delta_e^2)^k}\boldsymbol{I}$, where **I** is an identity matrix while $(\delta_\rho^2)^k$ is the density variances and $(\delta_e^2)^k$ is the variance of the misfit between successive iteration. Based on several numerical experiments done in the present work it was observed that the term $\frac{(\delta_\rho^2)^k}{1+(\delta_e^2)^k}\boldsymbol{I}$ can sometimes ends up in a larger value which may cause over regularization. For this reason, in the present study a new error weighting matrix ($\boldsymbol{W}_{ne}^k$) is proposed and it is expressed as:

$$\boldsymbol{W}_{ne}^k = \boldsymbol{diag}\left(\boldsymbol{A}\,\boldsymbol{W}_{zn}\left[\left(\frac{\left[\delta_\rho^2\right]^k}{1+[\delta_e^2]^k}\right)\boldsymbol{W}_h{}^k\right]\boldsymbol{A}^T\right) \tag{4.10}$$

According to Lewi (1997) at k[th] iteration $[\delta_e^2]^k$ is defined as:

$$[\delta_e^2]^k = \frac{\sum_{i=1}^{N}\{g_i - \sum_{j=1}^{M} a_{ij}[\rho_j^k]\}}{N-1} \tag{4.11}$$

The density variance $\left[\delta_\rho^2\right]^k$ applied here uses the standard variance formula expressed as follows:

$$\left[\delta_\rho^2\right]^k = \frac{\sum_{j=1}^{M}\left[\rho_j^k - \rho_{mean}^k\right]^2}{M-1} \tag{4.12}$$

In equation 4.10 only the terms in the square brackets are computed at each successive step. Whereas the terms outside the square brackets such as $\boldsymbol{A}^T$ and the product $\boldsymbol{A}\,\boldsymbol{W}_{zn}$ are independent of the iteration. Therefore, these values can be calculated once and stored at the beginning of the inversion process. This in turn reduces the computation time required for $\boldsymbol{W}_e^k$ recalculation in every iteration.

4.6 **Regularization Parameter Estimation Method**

The regularization parameter μ controls the tradeoff between the data fit and the stabilization term. Using large value of μ leads to big misfit value between the observed and predicted data which is equivalent to over-regularizing the solution. In contrast, small value of μ improves the data fit but the reconstructed models have highly oscillatory artificial structures which is the same as under-regularizing the solution. Consequently, choosing an appropriate value of the regularization parameter μ is a crucial part of the regularized inversion scheme to obtain a reasonable model, and also to achieve stability and improve convergence. The precise value of regularization parameter depends on the noise level associated with the observed data. Thus, the higher noise level of the data requires greater value of regularization parameter (Oldenburg and Li, 2005).

Estimation of an appropriate value for the regularization parameter μ in regularized inversion methods is a topic of much previous research. Several techniques have been proposed to choose a suitable μ that works well under certain conditions and new methods are being developed too. The well-known methods that are used commonly in geophysical inversion include: LC (Hansen and O'Leary, 1993; Hansen, 2001), GCV (Hansen, 1998; Vatankhah et al., 2014), MDP (Morozov, 1984; Vatankhah, 2014), unbiased predictive risk estimator (Lin and Wohlberg, 2008; Vatankhah et al., 2015) and adaptive regularization (Zhdanov, 2015). A general review together with the advantages and disadvantages of the LC, MDP and GCV approaches can found in literatures (e.g. Kilmer and O'Leary, 2001; Farquharson and Oldenburg, 2004; Lima et al., 2019). Several other approaches for selecting regularization parameters exist, and some are reviewed in standard texts (e.g. Vogel, 2002; Aster et al., 2018). As two of the most commonly used methods for determining the regularization parameter, in the context of geophysical inversion methods that can yield sharp and compact models, the LC method and adaptive regularization have been applied by numerous researchers.

Bassrei et al. (2007) employed LC in seismic traveltime tomography, Vatankhah et al. (2014) applied the LC method for the focusing inversion of surface gravity data, and Zhao et al. (2016) applied for magnetic inversion. Zhdanov (2009) and Rezaie et al. (2016, 2019) applied the adaptive regularization in 3D focusing inversion of gravity data, Ji et al. (2019) used the adaptive regularization in magnetic gradient tensor data inversion.

Properly estimated constant value of μ throughout the inversion scheme has been used in number of gravity inversion procedures developed by researchers (e.g. Silva and Barbosa, 2006; Zhang et al., 2015; Ghalehnoee et al., 2016). In contrast, there are several previous works where the parameter μ is changing in each iterative step (e.g. Portniaguine and Zhdanov, 2002; Farquharson, 2008; Zhdanov, 2009; Gholami and Gheymasi, 2016; Ji, et al., 2019). As pointed out by Farquharson and Oldenburg (2004) and Gholami and Aghamiry (2017) instead of using fixed value of μ, dynamic re-adjustment throughout the iterative scheme might be a superior approach. Taking this into consideration, in this thesis a simple and effective iterative regularization parameter estimation procedure, named an auto-adaptive regularization, is proposed. A detail discussion about the auto-adaptive regularization parameter estimation technique is given in the following subsection.

4.6.1 Auto-adaptive regularization parameter choice method

The fundamental idea of the auto-adaptive regularization method used to compute the regularization parameter μ in relation to the formerly known adaptive regularization approach, which was presented in Zhdanov (2015), is described as follows. In adaptive regularization approach the initial value of the regularization parameter μ^1 is updated at each iteration step by (Zhdanov, 2015):

$$\mu^k = \mu^1 q^k \qquad 4.13$$

where q is damping factor, which is decreasing geometric sequence from iteration to iteration. Its initial value is empirically determined having a value between zero and one. It is obvious that the trial and error selection of the value for q is cumbersome. The newly proposed auto-adaptive regularization method overcomes this problem and its values are determined iteratively using the following formula:

$$\mu^k = \mu^{k-1}\left[\frac{|\boldsymbol{g}^{obs} - \boldsymbol{A\rho}|^{k-1}_{max}}{|\boldsymbol{g}^{obs} - \boldsymbol{A\rho}|^{k}_{max}}\right] \qquad 4.14$$

where the term in the square bracket is an adjusting factor that is automatically determined at each iterative step. In the auto-adaptive regularization method, choosing a suitable initial value of (μ^1) is essential. Based on a number of synthetic and real data simulations done in this work recommend the following in choosing a reasonable value of μ^1: Firstly, the initial value of μ should be within the range $0 < \mu \leq 1$. Secondly the precise value of μ^1 depends on the noise level related with the observed data. When the probable or expected noise level of the data is higher, a larger value of μ^1 is a reasonable choice to avoid unwanted and false anomalies due to noise. In contrast, when the probable or expected noise level is less a small value of μ^1 should be chosen. Once an appropriate initial value of μ^1 is given as an input, then for subsequent iterations equation 4.14 gives an easy way to determine the current regularization parameter μ^k in each iterative step by multiplying the former μ^{k-1} with the adjusting factor. As it can be observed from equation 4.14 the advantage of the auto-adaptive regularization scheme is not only the automatic determination of the determine a suitable regularization parameter it also adjusts itself in the course of the iterative inversion process until the stopping criteria become satisfied. Consequently, it eliminates the need to manually estimate the regularization parameter for other than the first step.

4.7 **Depth Weighting**

In this section, a new depth weighting function with automatic determination of its parameter is introduced. It is a well-known fact that gravity data inversion has no inherent depth resolution. As a result of this, the reconstructed model from the inversion process tends to concentrate near the surface, regardless of the true depth of the causative body. This is a direct manifestation of the natural decay of the gravity kernel values with increasing depth from observation locations. The decay of the kernel with depth from the surface observation point is demonstrated in Figure 4.2 where panels (a) and (b) show kernel decay for different cell sizes discretization. The kernel values were calculated using equation 2.9 for a mesh along a single column of cells at a single observation point. In order to overcome this problem several approaches have been developed, by a number of researchers (e.g. Portniaguine and Zhdanov, 2002; Commer, 2011; Cella and Fedi, 2012). Particularly, the first and the most common approach to

counteract the kernel's decay and hence solve the lack of depth resolution is to use a depth weighting function which was introduced by Li and Oldenburg (1996) for 3D magnetic inversion. It has been proved that the application of the depth weighting function in magnetic inversion prevented the concentration of recovered susceptibility at the surface (Li and Oldenburg, 1996). Similarly, Li and Oldenburg (1998) introduced and used a depth weighting function that approximately compensates for the gravity kernel's decay in gravity inversion. The depth weighting function formerly suggested by Li and Oldenburg (1996, 1998) has the form:

$$w_z(z) = \frac{1}{(z_j + z_o)^{\frac{\beta}{2}}} \qquad 4.15$$

where z_j is the mean depth variable of the j^{th} cell and z_o and β are adjustable parameters. The parameter z_o depends on the cell size and the observation height of the data. z_o is calculated in such a way that the decay of weighting function mimics the decay of the kernel at an observation point with $w_z(z)$ for a known value of β.

The commonly chosen β value is to reproduce the power-law decay of the gravity kernel. Hence based on numerical tests Li and Oldenburg, (1998) suggested the β values be $1.5 < \beta \leq 2$, and the most acceptable value of β is 2 for gravity inversion. Oldenburg and Li (2005) pointed out that the appropriate value of β used in a particular inversion could be chosen in the range between 1.5 and 2, by finding the best performance of different β values applied on synthetic data from forward models that resembles the expected solution. Nevertheless, the choice of a test model that resembles the real one might not always be an easy task and there are no other methods mentioned so far on how to choose an acceptable value of β for specific inversion. The exponent β is very crucial in determining the final model. Hence, it is extremely important to look for a method that determines an optimal value to get geologically plausible results. Moreover, comparative analysis between $w_z(z)$ (equation 4.15) and the gravity kernel is also very important, it is only so far being done for the magnetic inversion (e.g. Li and Oldenburg, 1996; Oldenburg and Li, 2005; Cheyney et al., 2015). Hence, one of the goals of this research work is to investigate this function: compare it with the gravity kernel, and analyze how the solution changes with variable β values, and then propose a new depth weighting function which overcomes the limitation of the old function in equation 4.15.

Comparison of the gravity kernel with weighting function (equation 4.15) as a function of depth is shown in Figure 4.2. The values for the weighting function were computed for different values of β such as 1.5, 2, as suggested by Li and Oldenburg, (1998) and additionally with 3. Then optimum z_o value is approximated by using the standard least-squares optimization between the actual kernel values and $w_z(z)$ for these β values. The obtained optimum parameters for different cell sizes are also presented in Figure 4.2. We can see that z_o values insignificantly vary with β values for the same cell size. In contrast, comparing the values in Figure 4.2a and b, z_o values

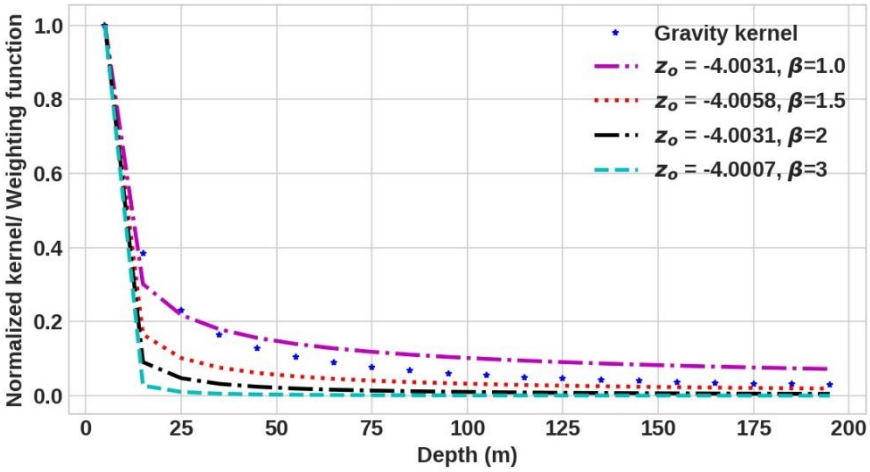

(a)

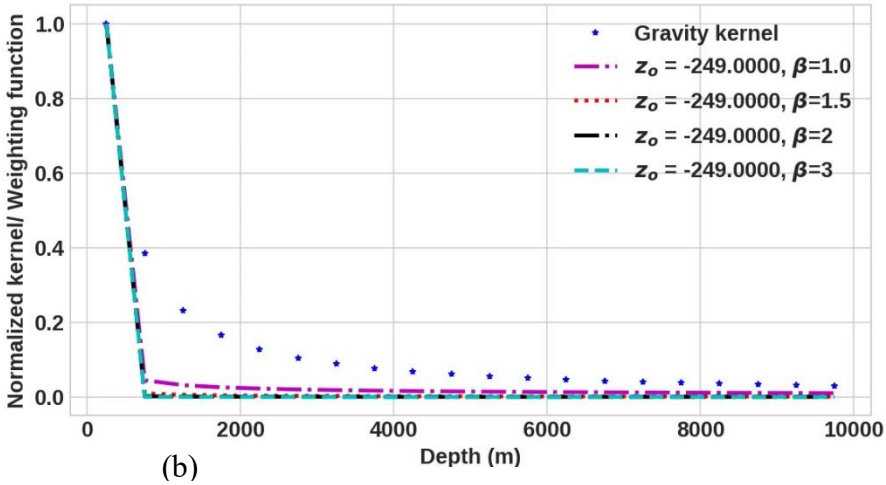

(b)

Figure 4.2: Comparison of the gravity kernel decay and $w_z(z)$ (equation 4.15) directly beneath the observation point for three different values of β. The corresponding computed z_o values are also presented. Both curves are normalized with their respective maximum value. (a) Displays for 10 x 10 m cell size discretization. (b) Displays for 500 x 500 m cell size discretization.

dramatically vary with cell size for the same β value. The values for the weighting function were computed using the parameters obtained this way. In Figure 4.2 all the values are normalized with respect to their maximum value. As we can see from the figure, $w_z(z)$ decays in the same manner as the gravity kernel at very shallow depths, up to about the cell size and then more rapidly in shallower depths greater than the cell size. At higher depths, both curves asymptotically approach 0 value. This is found to be true for all discretization schemes. Finally, at deeper depth, it decays smoothly but still at a different rate relative to the gravity kernel. In all the presented cases one can notice a significant discrepancy between $w_z(z)$and the gravity kernel especially near the elbow of the curves. As shown in Figure 4.2b for large cell size the behavior of the weighting function curve becomes the same for all β. Hence, we can say that for large cell size the behavior of the curve is independent of β values in ranges $1.5 < \beta \leq 3$. In contrast, for small cell size the curve shows some differences for different β values (Figure 4.2a). This variation of the characteristic of $w_z(z)$ with cell size, could make it hard to choose the best β value for specific inversion. Consequently, this behavior of the weighting function curve may also yield some effect on the inversion result. Moreover, numerical tests done for $\beta = 3.5$ and $\beta = 4$, where the results not presented here demonstrate that $w_z(z)$ shows different unacceptable characteristics depending on the cell size as compared to the kernel function. Hence, based on the results, I suggest the appropriate range of β values to be $1.0 < \beta \leq 3$. The implementation of different values β within the suggested range will be tested with synthetic examples in subsection 5.2.2

Considering the aforementioned shortcomings, it was necessary to modify the depth weighting function (equation 4.15) by introducing a better function that can counteract the natural decay of the kernel functions. Towards this a new depth weighting function $w_{zn}(z)$, which is given in equation 4.16, is proposed. The corresponding diagonal elements of the depth weighting matrix $\boldsymbol{W}_{zn}$ is also shown.

$$w_{zn}(z) = \left(az_j + c_o\right)^{-\tau}$$

$$\boldsymbol{W}_{zn} = \boldsymbol{diag}\left(w_{zn}(z)\right) \qquad 4.16$$

where z_j is the mean depth variable of the j^{th} cell and a, c_o and τ are adjustable parameters. The values of the three parameters were calculated by optimizing $w_{zn}(z)$ to match with the gravity kernel function.

Figure 4.3 shows, the result of the optimization using equation 4.16, for those two examples in Figure 4.2. The parameters were estimated by the standard least-squares optimization. As it can be seen from Figure 4.3, the graph of the depth weighting function and the kernel matches very well at all depths for all cell sizes. This

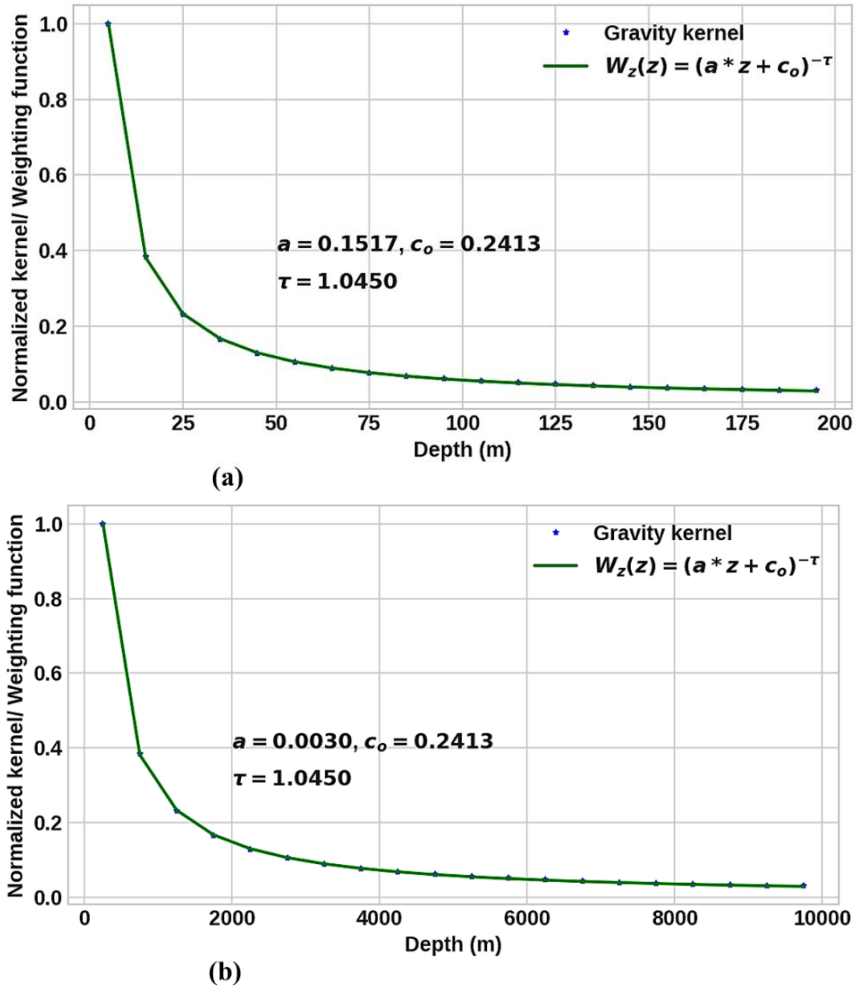

Figure 4.3: Comparison of the gravity kernel and $w_{zn}(z)$ from equation 4.16 directly beneath the observation point. Both curves are normalized with their respective maximum value. (a) Displays for 10 x 10 m cell size discretization. (b) Displays for 500 x 500 m cell size discretization.

is also found to be true in many other tests, whose results are not presented here. Thus, the new depth weighting function approximates the kernel decay more properly and hence it is more appropriate to compensate for the kernel's natural decay in a better way at any depths provided that a reasonable value is determined for all three

parameters. The implementation of $w_{zn}(z)$ will be tested in the following chapter by inverting synthetic and measured data.

4.8 Physical Parameter Inequality Constraints and its Implementation Algorithm

To obtain a physically meaningful model with more realistic geological meaning, potential field inverse solutions should be constrained with real and accurate range of physical parameters. In other words, incorporating physical parameter inequality constraints in potential field inverse modelling procedure can reduce ambiguity, enhance stability and improve the overall accuracy of the inversion results leading to geologically plausible model (Silva et al., 2001; Oldenburg and Li, 2005). For this reason, in geophysical inverse modelling, several physical parameter constraint functions have been proposed and implemented. Kim et al. (1999) introduced a logarithmic transformation function to restrict the conductivity values within the imaging volume to be within the reasonable range. This function has been successfully applied to electrical resistivity tomography by Cardarelli and Fischanger (2006). A hyperbolic tangent transformation function has been proposed by Commer and Newman (2008) to restrict the conductivity parameters and ensured rationality of the conductivity. Commer (2011) applied the hyperbolic transformation function for gravity inversion to constrain the density contrast values and obtained a similar benefit. Lelievre and Oldenburg (2006) suggested a square root transform function which is also applied by Pilkington (2008) in his magnetic invertion procedure to constrain the obtained magnetic susceptibility values within reasonable range. Other physical parameter constraint strategies that have been applied in different inversion schemes include gradient projection approach (Wang and Ma, 2007; Lelièvre et al., 2009) and the logarithmic barrier approach (Li and Oldenburg, 2003; Oldenburg and Li, 2005). In all of the mentioned literature the inversion results are dramatically improved with the use of physical parameter constraints.

In the context of compact or focused gravity inversion methods, as compared to the above-cited approaches, a direct upper and lower bound density constraint function is the simplest and most effective method, which does not require adjustment of additional parameters and is hence widely applied (Barbosa and Silva, 1994;

Portniaguine and Zhdanov, 1999; Silva et al., 2009; Meng, 2018; Rezaie, 2020). Therefore, in this study, I adopted and implemented the direct minimum and maximum physical parameter (density contrasts) values as a constraint function to limit the inversion results within the reasonable range. In this situation, the density contrast values in the obtained model will be between the minimum and maximum physical parameter bounds. In other words, at every iterative step the density contrast of each cell must full fill element wise physical parameter inequality constraint which can be expressed by:

$$\boldsymbol{\rho}_{min} \leq \boldsymbol{\rho}^{k} \leq \boldsymbol{\rho}_{max} \qquad 4.17$$

where vectors $\boldsymbol{\rho}_{min}$ and $\boldsymbol{\rho}_{max}$ represent the minimum and maximum density limits for specific cells. Values of the minimum and maximum bounds of the physical parameter constraints can be obtained from a prior information such as geological maps in conjunction with published density values of rocks, well-logging, and/or laboratory tests. Because, the developed inversion method recovers density contrasts not true densities, the minimum ($\boldsymbol{\rho}_{min}$) and maximum ($\boldsymbol{\rho}_{max}$) density constraints of each cells must be provided as density contrast values rather than true densities. Density contrasts are determined by subtracting the background density value from the target anomalous density value where both are obtained from previous investigations.

To impose the inequality constraint on the estimated density distribution I have developed a Physical Parameter Inequality Constraint Algorithm (PPICA). The PPICA is incorporated and executed at each iteration within the presented inversion algorithm. The inequality constraint algorithm imposes the minimum and maximum bounds by computing the hard constraint matrix ($\boldsymbol{W}_h{}^k$) (Boulanger and Chouteau, 2001) and the reference density contrast vector $\boldsymbol{\rho}_F^k$ as follows: The diagonal elements of $\boldsymbol{W}_h{}^k$ are fixed at ε or 1.0. When a prior geological or geophysical information are able to provide the initial value of density contrast of the j^{th} specific cells ($\boldsymbol{\rho}_j^{apr}$), then these values are assigned to the corresponding $[\boldsymbol{\rho}_F]_j$. Similarly, the corresponding diagonal elements of $\left[\boldsymbol{W}_h{}^k\right]_{jj}$ are fixed at ε. During the inversion process, if the j^{th} elements of estimated density values ($[\boldsymbol{\rho}^k]_j$) falls out of any of the inequality constraint limits defined by $[\boldsymbol{\rho}_{min}]_j$ and $[\boldsymbol{\rho}_{max}]_j$ then $[\boldsymbol{\rho}_F^k]_j$ and of estimated density values $[\boldsymbol{\rho}^k]_j$ will be fixed at the violated bound density itself and $\left[\boldsymbol{W}_h{}^k\right]_{jj}$ is fixed at ε. On the other hand, if

$[\boldsymbol{\rho}^k]_j$ did not exceed its bounds (i.e. lies between the limits), $\left[\boldsymbol{W}_h{}^k\right]_{jj}$ and $[\boldsymbol{\rho}_F^k]_j$ are assigned to be 1.0 and 0.0 respectively and elements of $[\boldsymbol{\rho}^k]_j$ remains unchanged. Mathematically, in the case of $[\boldsymbol{\rho}^k]_j$ takes a value beyond the limits can be described as:

$$if \quad [\boldsymbol{\rho}^k]_j \geq [\boldsymbol{\rho}_{max}]_j \begin{cases} [\boldsymbol{\rho}_F^k]_j = [\boldsymbol{\rho}_{max}]_j \\ [\boldsymbol{\rho}^k]_j = [\boldsymbol{\rho}_{max}]_j \\ \left[\boldsymbol{W}_h{}^k\right]_{jj} = \varepsilon \end{cases} \tag{4.18}$$

Or

$$if \quad [\boldsymbol{\rho}^k]_j \leq [\boldsymbol{\rho}_{min}]_j \begin{cases} \left[\boldsymbol{\rho}_F^k\right]_j = [\boldsymbol{\rho}_{min}]_j \\ [\boldsymbol{\rho}^k]_j = [\boldsymbol{\rho}_{min}]_j \\ \left[\boldsymbol{W}_h{}^k\right]_{jj} = \varepsilon \end{cases} \tag{4.19}$$

Note that, using PPICA one can assign different values of upper and lower bounds for each cell in the model space. Therefore, unlike the previous works (e.g. Last and Kubik 1983; Lewi 1997) which used the same minimum and maximum density limits for the whole model, this algorithm allows the possibility of assigning different density values for the upper and lower bounds in different regions of the model space. As a result, multiple anomalous bodies with different densities located at different parts the of the subsurface can be recovered.

By means of $\boldsymbol{W}_h{}^k$ when any blocks whose density is known from a priori information or exceeds the density constraint limit, the algorithm will force the value back to the exceeded limit or known value and automatically freezes this block in the next iteration by assigning a very small weight to it. Whereas, $\boldsymbol{\rho}_F^k$ is used to remove the gravity effects of those cells that violated the density constraint limit or equal to the target density from the observed gravity data at each iteration. In other words, it is applied to compute reduced gravity data vector $\boldsymbol{g}_r^k = \boldsymbol{g}^{\boldsymbol{obs}} - \boldsymbol{A}\boldsymbol{\rho}_F^k$ in equation 4.6. Then the inversion of subsequent iteration will be performed using reduced gravity data vector $\boldsymbol{g}_r^k$. $\boldsymbol{\rho}_F^k$ is also applied to estimate the density contrast values in the next iteration by equation 4.6.

4.9 **Stopping Criteria**

In this section, I introduced an effective combined stopping criterion to terminate the iterative process after optimal number of iterations. It is clear that if the iterations are stopped too early, then a reasonable solution of the inverse problem may not be obtained. Despite that, too many iterations may waste computer time without increasing the overall solution qualities. In other words, a well-chosen stopping criterion can result in either computational time saving or improved solution quality. Thus, one of the important aspects of any iterative inversion method is to decide when the iterations should be terminated. A number of stopping criteria have been proposed and employed to terminate iterative inversion algorithms (e.g. Borges et al., 2015; Levin and Meltzer, 2017). Commonly used stopping criteria are based on a norm of the residual vector (i.e. the norm of the difference between estimated and observed data). For instance, a noise level, i.e. $\chi^2 = \|\boldsymbol{W}_d(\boldsymbol{g}^{obs} - \boldsymbol{A\rho})\|_2^2$, is used by Boulanger and Chouteau (2001) and Vatankhah et al. (2017). In the last equation the diagonal matrix $\boldsymbol{W}_d$ is the data weighting matrix whose i^{th} element is the inverse of the standard deviation of the noise at each data point. Other frequently applied criteria for stopping the inversion procedure are based on simple misfit or the Root Mean Square Error ($RMSE$) between the observed data and computed data produced by the predicted model (e.g. Rezaie and Moazam, 2017; Feng et al., 2018). The expressions used to estimate these criteria are the following:

$$misfit = \left(\frac{\sum_{i=1}^{N}(g_i^{obs} - g_i^{cal})^2}{\sum_{i=1}^{N}(g_i^{obs})^2}\right)^{1/2} \leq \delta \qquad 4.20$$

$$RMSE = \left(\frac{\sum_{i=1}^{N}(g_i^{obs} - g_i^{cal})^2}{N}\right)^{1/2} \leq \delta \qquad 4.21$$

where δ is the tolerance, assumed given. Ekinci (2008) also proposed and implemented other possible criterion, namely parameter variation function (smy), for stopping the iteration process in compact gravity inversion algorithms. According to Ekinci (2008) smy is defined as:

$$smy = \left(\sum_{j=1}^{M} \left(\rho_j^k - \rho_j^{k-1} \right)^2 \right)^{1/2} \qquad 4.22$$

As pointed out by Ekinci (2008) the parameter variation function smy was only tested for noise free synthetic data and recommended to test it for noise contaminated data. Moreover, Ekinci (2008) does not present a precise threshold value of the function to stop the iteration but simply suggests that the iteration should stop when smy is minimum.

The widely used approach is to quit the iterative process when one of the above criteria are below a given tolerance (e.g. the level of observational error). In other terms, most geophysical inverse modelling algorithms have been designed to implement a single criterion. However, in practical applications a precise value for such tolerance is rarely known; rather, only some possibly vague idea of the desired quality of the numerical approximation is at hand. Moreover, it has been pointed out by Rao, et al. (2018) that stopping iteration based solely on the norm of the residual is neither safe nor a robust solution. The non-uniqueness and instability of the gravity inverse problem further complicates the usage of only one of the aforementioned stopping criteria.

To overcome the above-mentioned issues, in the present work the $misfit$ and smy stopping criteria are jointly used as a combined criterion. The fundamental idea of the presented combined stopping criterion is as follows. According to numerous simulations, the $misfit$ and smy values from one iteration to the other decreases as it is supposed to converge. Consequently, the absolute value of the differences, in both of these quantities, from one iteration to the other can be used as a stopping criterion. Therefore, to terminate the iterative inversion process one of the following stopping criteria must be satisfied:

(I) the maximum number of iterations (k_{max}) is reached

(II) The difference between two consecutive iteration values of smy and $misfit$, have reached the target threshold values. In other words, both the conditions $|smy^{k-1} - smy^k| \leq \tau$ and $|misfit^{k-1} - misfit^k| \leq \varphi$ must be satisfied at the same time.

Before implementing the above combined criterion, in this work for the first time the smy function was tested with noise contaminated data and further improved by setting the precise threshold value of the function to stop the iteration in combination with $misfit$. Accordingly, for the inversion considered here, based on a number of tests done, parameter τ and μ are assigned to be $\sqrt{2M}$ and $\varphi = 0.005$ respectively. Where M is again the total number of model parameters. The advantage of this stopping criterion is that: first, unlike the common termination techniques it does not require the level of the noise level to set as tolerance; secondly, it avoids premature or delayed termination of the iterative process observed in using the common single criterion. The efficiency and practicality of this stopping criteria is verified in section 5.2 with synthetic examples and in section 5.3 with real examples.

4.10 Computational Procedure for the Developed Inversion Algorithm

The inverse modelling consists of an iterative procedure in which the weighting matrices are changing at each iteration until an acceptable convergence of the solution is obtained. The input parameters for the inversion procedure are: (1) Kernel matrix ($\boldsymbol{A}$) and discretized subsurface model (mesh) and its initial approximation reference density model $\boldsymbol{\rho}_F$ if exits based on a priori information; (2) Observed gravity anomaly ($\boldsymbol{g}^{obs}$) with its measurement points (x); (3) Maximum number of iterations (k_{max}); (4) Lower $\boldsymbol{\rho}_{min}$ and upper $\boldsymbol{\rho}_{max}$ density contrast bounds and initial μ^1 value. In summary, the steps taken to carry out the inversion process by means of the proposed methodology consists the followings.

1) Chose the depth weighting function either w_z (equation 4.15) or w_{zn} (equation 4.16) then compute the corresponding $\boldsymbol{W}_z$ or $\boldsymbol{W}_{zn}$ with equation 4.17.
2) Compute $\boldsymbol{A^T}$, and depending on the selected depth weighting function evaluate $\boldsymbol{AW_{zn}}$ or $\boldsymbol{AW_z}$
3) At iteration k = 1, solution for $\boldsymbol{\rho}$ satisfying the inequality constraints is obtained by using equation 4.6 and setting $\boldsymbol{W}_h{}^k = \boldsymbol{W}_{L_0}^k = \mathbf{I}$; $\boldsymbol{\rho}_F^k$ = zero vector, and with initial given value of μ^1.
4) Forward modelling: compute the predicted gravity anomaly pre

5) Commence the next iteration and evaluate $\boldsymbol{W}_h{}^k$ and $\boldsymbol{\rho}_F^k$ with **PPICA** using previous iteration result and then $\boldsymbol{g}_r^k$ using the inversion result from the previous iteration.
6) Compute $\boldsymbol{W}_{L_0}^k$ using equation 4.8 and subsequently $\boldsymbol{W}_m^k$ with equation 4.7
7) Calculate μ^k, $[\delta_e^2]^k$ and $\left[\delta_\rho^2\right]^k$ using equations 4.14, 4.11 and 4.12 respectively.
8) Compute $\boldsymbol{W}_{ne}^k$ with equation 4.10
9) Carrying out the inversion using equation 4.6.
10) Impose the inequality constraints on $\boldsymbol{\rho}^k$as discussed in the preceding section.
11) Test for stopping criteria. If the stopping criterion is satisfied, the iteration terminates and obtained results are stored and plotted. Otherwise, using the current estimated contrast density model, increment k and go to the fourth step and continue the iterative procedure until the stopping criteria are fulfilled.

4.11 **Brief Description of the Inversion Algorithm Python Programs**

In chapter 2 section 2.4 I have discussed the FM and the plotting python modules developed and bundled in **PyGM** package which is presented as part of this Ph.D. research work. In this section, I briefly describe the developed inversion algorithm python modules. As noted in section 2.4, all programming work done in the present thesis are based on multiple packages from the Python environment. Thus, accreditation to open-source algorithms have been made wherever necessary. The inversion package consists of a number of modules that allow the implementation of the newly developed inversion method based on the above described procedures. The list of the main available modules developed to implement the inversion method are given in Table 4.1.

The PyGM.Weighting.py module consists of several functions that help to perform the calculation of different weighting matrices, for example depth weighting, the L_0-norm or compactness weighting and the hard constraint, which are to be used by

the **PyGM.inv_2d** inversion module. The **PyGM.inv_2d** performs all the inversion tasks.

Table 4.1 Written codes for the developed inversion method

No	Developed modules	Uses of the developed module
1	**PyGM.Weighting.py**	Calculates different weighting matrix (e.g. compact weighting matrix)
2	**PyGM.Comon.py**	Comprises common useful functions (e.g. misfit, and density constraint functions)
3	**PyGM.inv_2d.py**	Inversion algorithm module including the new inversion approach, and consists a number of functions.

4.12 Chapter Summary

Delineating localized and blocky geologic features through the inversion of gravity data is an important goal in a range of geophysical investigations. In order to recover such geologic features, developing non-smooth inversion algorithms attracted much attention in the last decades and it is an active area of research. Taking this into account, in the current chapter, I have presented a non-smooth gravity inversion method that can yield a compact and sharp image of the subsurface density distribution. The method is based on the minimization of an objective function, which consists of L_2-norm data misfit and L_0-norm stabilizing functions, by iteratively reweighted least-squares (IRLS) algorithm. Further details of the features of the proposed algorithm are well presented in different sections of this chapter.

Besides the development of the python programs to implement the method, the following major contributions are introduced and described. The first, presented in section 4.5, is a new iterative error weighting strategy, which improves the stability of the inversion method. The second, discussed in section 4.6, is the auto-adaptive regularization parameter estimation method. The third, presented in section 4.7, is a

new depth weighting function to counteract the natural decay of the kernel function. The fourth, described in section 4.10, is a combined stopping criterion that helps to terminate the iterative process after an optimal number of iterations. Apart from these, to impose the physical inequality constraints on density contrasts from the inversion process an efficient algorithm named Physical Parameter Inequality Constraint Algorithm (PPICA) has also been developed and incorporated in the inversion procedure. The PPICA allows enforcing localized density constraints at different localities of the model space to allow the recovery of multiple causative bodies having different densities. Finally, in the last part of this chapter, a detailed description of the written python programs for the implementation of the developed inversion method was given. I carry out extensive synthetic and real data test examples in the next chapter to illustrate the applicability and effectiveness of the proposed inversion method.

CHAPTER 5: SYNTHETIC AND REAL DATA TESTS

5.1 Introduction

In the previous chapter a gravity inversion method, which produces a compact and sharp model to recover non-smooth or blocky geologic causative bodies, was developed. The features of the method were well described in different sections of the chapter. In this chapter, the developed gravity inversion method is applied to a number of synthetic and real data sets to illustrate and prove its efficiency, and practical utility. Additionally, the major contributions of this Ph.D. research work such as the auto-adaptive regularization parameter estimation method (equation 4.14), the improved error weighting function (equation 4.10), the new depth weighting function (equation 4.16), and the combined stopping criterion are examined.

The first part of this chapter presents the applications of the inversion method to different synthetic models. The models vary in geological complexity or geometry, and dimensions. In the second part of this chapter, the method is applied on different real data sets measured over different geological settings. The inversion of both synthetic and real data sets are taken as tests of the proper functionality and applicability of the method. In general, all synthetic and real data tests are performed with the following objectives: (I) to investigate the capability of the developed inversion methods' to recover multiple anomalies with acceptable vertical and horizontal resolution; (II) to study the performance of the method in producing compact and sharp images of the causative bodies; (III) to examine the robustness of the method for different noise levels. These all, in turn, can prove applicability and effectiveness of the major contributions incorporated in the developed method. Moreover, specific aims of performing the different tests are also mentioned in the following separate sections.

5.2 Synthetic Model Test

Before the proposed inversion approach is applied to real observed data it was tested on a number of synthetic gravity data. In all the tests made the inversion process yielded very good results. Since it is not possible to present all tests made, in this section, a series of selected synthetic model tests that are believed to imitate some real-world situation are presented. Based on the results the efficiency and applicability of the

proposed algorithm in resolving the location both vertically and horizontally, recovering the geometry and densities of the causative bodies is evaluated. In general, the detailed reason for carrying out the different synthetic model tests will be described in the following separate subsections.

The solution to the forward problem and the inverse modeling were strictly carried out using the procedures and/or python programs described in chapter 2 and 4 respectively. In the inversion of synthetic examples, the same subsurface discretization with the one used in generating the synthetic data (Forward modeling) is implemented.

5.2.1 Synthetic model tests to evaluate the robustness of the method

The purpose of this section is to test and analyze the robustness of the developed inversion scheme to different noise levels. Besides, the capability of the inversion scheme to efficiently produce compact and sharp models is demonstrated by comparing the results with smooth (L_2-norm regularized) inversion. In order to assess and analyze the robustness and stability, the developed inversion algorithm has been applied to a noise-free and noise-contaminated data set.

The first synthetic model examples consist of a single rectangular block anomalous source buried at a different depth (Figure 5.1). The density contrast of the anomalous block was set to be $2000\ \frac{kg}{m^3}$ with zero background density. In order to test for two different cell size discretization schemes, the dimension of each cell for the model shown in Figure 5.1a is set to 10 m x 10 m, and for the model in Figure 5.1b is set to 100 m x 100 m, both in the X and Z directions, respectively. In these synthetic models, the entire model domain is divided into 60 x 20 = 1200 square cells in the horizontal and vertical directions respectively. In the case of the 10 m x 10 m discretization scheme, the top of the anomalous body is located at 50 m depth. For the second case, which is for 100 m x 100 m cell size, the top of the causative body is located at 500 m depth. In all cases, the computed gravity data at the surface consists of 60 total observation points with regular sample spacing 10 m and 100 m for the first and second cases respectively, and it is shown in Figure 5.1 top panels with star dots.

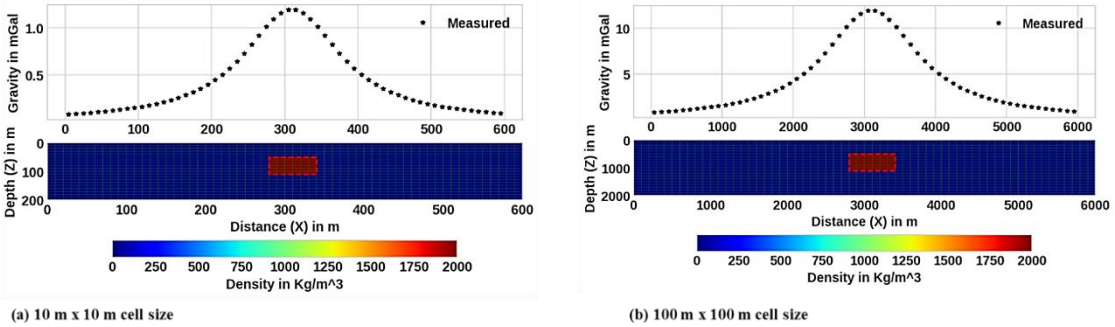

Figure 5.1. Synthetic model examples consisting a single rectangular shaped anomalous source for two different discretization schemes and two different depths and size of the causative body. The corresponding gravity anomaly (star dots) is shown on the top panels.

After generating the synthetic data using the solution of the forward problem, the presented inversion algorithm was applied to the noise-free data set to recover density-contrast models. In addition, for the sake of comparison the noise-free data set were also inverted with the classical smooth inversion approach. In the course of the inversion process, the initial value of the regularization parameter μ^1 was taken as 10^{-4}, and the elements of the minimum density limit $\boldsymbol{\rho}_{min}$ and the maximum density limit $\boldsymbol{\rho}_{max}$ were assigned a value of 0.0 and 2000 $^{kg}/_{m^3}$ respectively, for all inversions done in these examples. The final inversion results produced by the smooth inversion method are displayed in Figure 5.2 where the green dashed line represents the outline of the true boundary. Even though the anomalous rectangular block is recovered roughly at the right location, the edges of the block are not defined adequately.

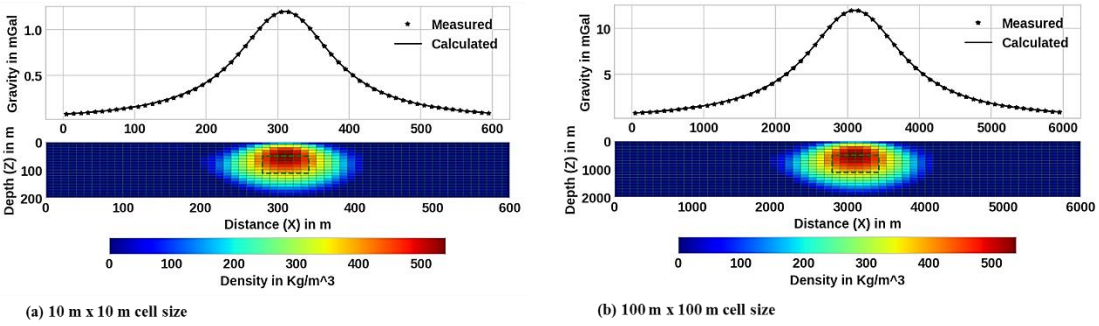

Figure 5.2: Noise free data smooth inversion results for the synthetic models shown in Figure 5.1. The bottom panels show the final recovered density contrast model and the top panels show the noise free data and the corresponding predicted data. The doted red lines show the true boundaries of the causative bodies that were used to derive the synthetic data.

As expected from L_2-norm regularized inversion, the recovered model is smooth (characterized by smeared-out boundaries). This is also pointed out by a number of scholars (e.g. Sun and Li, 2014; Utsugi, 2019). The other concern, as can be seen from the result (Figure 5.2), is that the target density contrast values are underestimated which can make the interpretation of the inverted model more difficult.

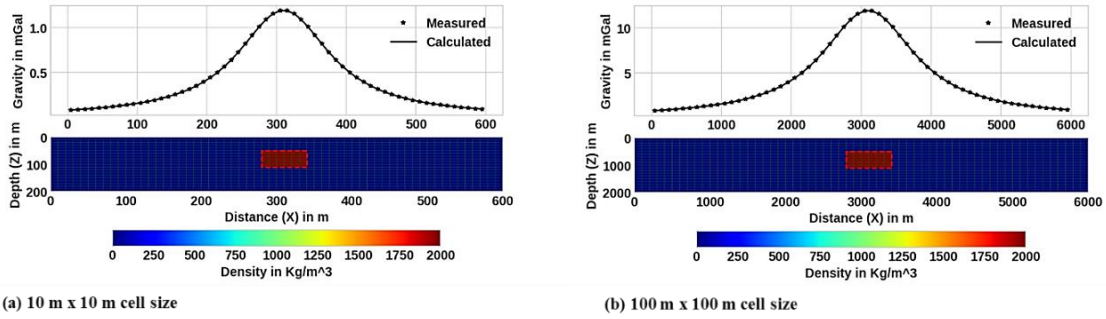

Figure 5.3. Noise free data inversion results, using the presented algorithm, for the synthetic models shown in Figure 5.1. The top panels show the noise free data and the corresponding predicted data. The bottom panels show the final recovered density contrast model. The doted red lines show the true boundaries of the causative bodies that were used to derive the synthetic data.

On the other hand, the developed algorithm unlike the smooth inversion successfully recovered the true density contrast values, geometry, and location of the rectangular buried body for both discretization schemes (see Figure 5.3 bottom panels). The anomalous rectangular block in the recovered density models is compact with sharp boundaries which is exactly the same as the true boundaries of the bodies, suggesting that the proposed algorithm can resolve blocky or localized structures with sharp boundaries. Note that the corresponding observed data (star dots) and predicted response (solid line) are completely matching with each other (see Figure 5.3 top panels). Several other tests of the method were made on noise-free synthetic data for different hypothetical geological settings. In all the tests, the method has successfully reproduced the actual model exactly. The results presented above also verify this observation. Notice that the results also indicate the applicability of the proposed auto-adaptive regularization technique (equation 4.14) and error weighting function (equation 4.10), in the case of noise-free data inversion. However, in the real world, data would contain a certain level of noise that could not be corrected or eliminated by data processing and usually affects the result of the inversion process. Thus, in the followings, the robustness of the method for the same models but with different noise levels is investigated.

Here the synthetic model shown in Figure 5.1a and the corresponding noise-free data are considered again. Before running the inversion, the noise-free data is contaminated with Gaussian noise with varying levels. Each noise level was separately generated using zero mean and standard deviation that amounts to 1, 4, 5, and 7% of the magnitude at each data point. This was then, added to the noise-free data to obtain four separate data sets. Using these data sets four separate inversion runs were performed with the developed inversion algorithm. The inversion results for different noise levels are shown in Figure (5.4a-d).

We can see from the results in Figure 5.4 that, the developed inversion technique can reliably reconstruct the model that has been used to derive the synthetic data, including its location, geometry and density, with acceptable accuracy. Further, like the noise-free inversion results (Figure 5.3) the anomalous rectangular shaped block in the recovered density models are compact with sharp boundaries, which are satisfactorily consistent with true boundary. This suggests that the developed inversion method perform very well in resolving blocky structure with sharp boundaries. The presence of the noise in the data is also managed very well and it does not strongly affect the result of the inversion.

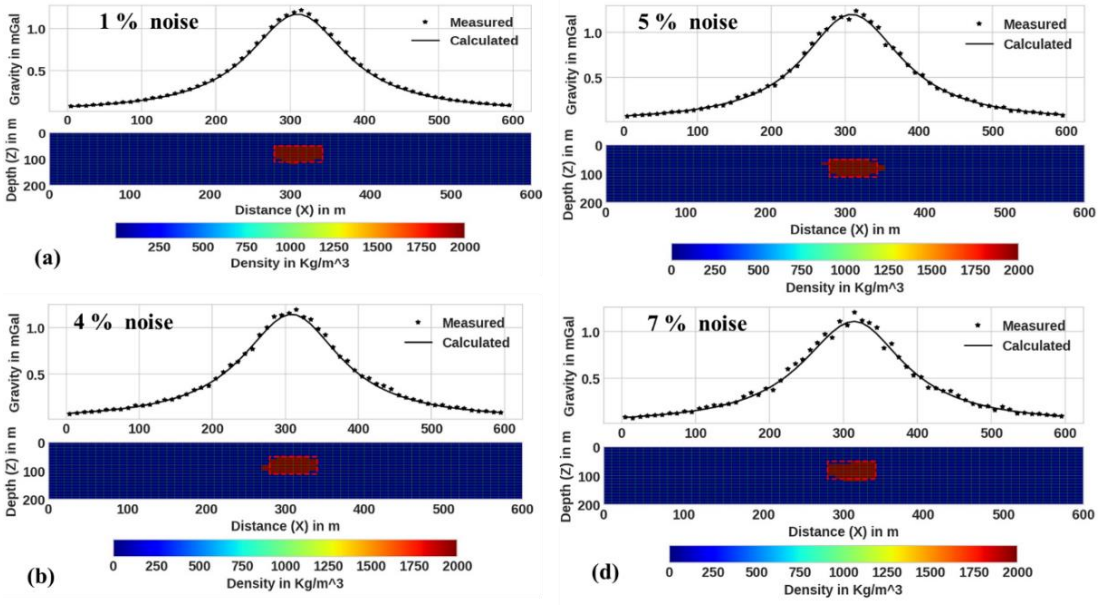

Figure 5.4: Inversion results, using the proposed method, for different noise levels in the data. The red dashes lines show the outlines of the actual model.

As we can also see from Figure 5.4 top panels, the synthetic data (star dots) and predicted response (solid line) are acceptably coincident with each other. According to

the obtained results, the algorithm behaved well with different noise levels embedded in data and it still retained its stability. This can confirm the robustness and stability of the developed inversion method for different noise levels that are commonly encountered during real data measurement, and thereby indicate the applicability of the proposed auto-adaptive regularization technique (equation 4.14) and error weighting function (equation 4.10) when the data is corrupted with different noise levels.

5.2.2 Synthetic model tests for the new depth weighting function

In this subsection, the synthetic model tests were performed for the following two major objectives. The first one is to investigate and illustrate the role of the new depth weighting function $w_{zn}(z)$ (equation 4.16), and later to evaluate the capability of the method in resolving the location of multiple causative bodies both vertically and horizontally. In addition, the performance of the method to produce compact and sharp images is demonstrated. The second one is to test and demonstrate the implementation of $w_z(z)$ (equation 4.15) with different values β within the range $[1,3]$ which is outside the proposed limit by Li and Oldenburg (1998) for gravity data inversion. In each example different cell size digitization was applied in order to test the effectiveness of the newly proposed depth weighing function $w_{zn}(z)$ (equation 4.16).

For the first synthetic model examples, again, a similar model to that shown in Figure 5.1 are reconsidered. In order to perform the test for three separate scenarios, here the rectangular shaped anomalous source is buried at three different depths. Accordingly, in the case of the 10 m x 10 m discretization scheme, the top of the anomalous body is located at 20 m, 50 m, and 70 m depths as shown in Figure 5.5a with a red solid line. For the second case, which is for 100 m x 100 m cell size, the top of the causative body is located at three different depths that amount to 200 m, 500 m, and 700 m (see Figure 5.5b red solid line). For all separate scenarios, the FM is performed to obtain gravity data, which consists of 60 total observation points with a regular sample spacing of 10 m and 100 m for the 10 m x 10 m and 100 m x 100 m cell size discretization schemes respectively. Then the computed data were contaminated with Gaussian noise with zero mean and standard deviation that amounts to 3 % of the magnitude at each data point.

Using the noise-contaminated data sets the inversion process was performed first without the use of depth weighting, and secondly by applying the proposed depth weighing function $w_{zn}(z)$. The three parameters of the new depth weighting function are determined automatically according to the procedure described in section 4.7. For both cases, during the inversion, the minimum density limit for the inequality constraint was chosen as $\boldsymbol{\rho}_{min} = 0.0$ and the elements of the maximum density limit $\boldsymbol{\rho}_{max}$ were assigned a value of $2000\ {}^{kg}/_{m^3}$. The initial value μ^1 has given a value of 0.3 for all inversions in these examples.

The inversion results, including the outlines of the true synthetic model (red solid line), without the implementation of the depth weighting were shown in Figure 5.5. In Figure 5.5a the obtained results for the 10 m x 10 m cell size discretization were shown, with each panel showing the location of the causative bodies at different depths.

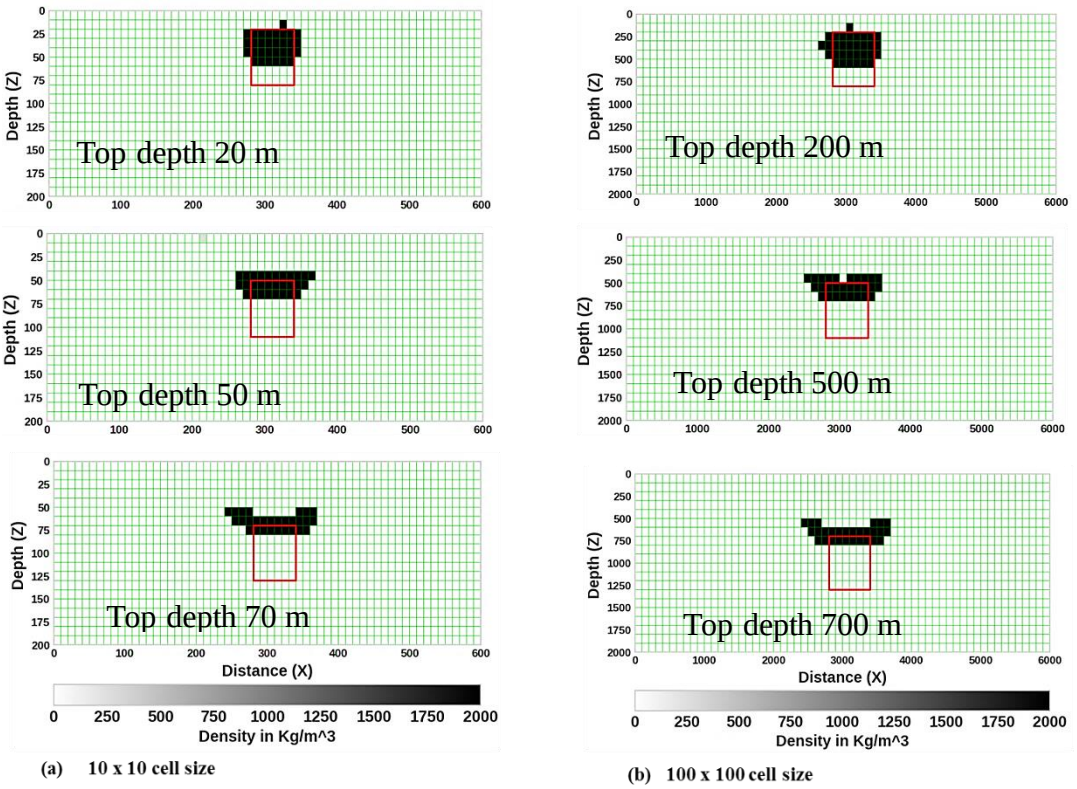

Figure 5.5: Results of synthetic data inversion without depth weighting function. The three rows are results from the inversion of the synthetic data, when the anomalous rectangular shaped block is placed at three different depths. The red solid line indicates the outlines of the true location of the causative body, which is used for the forward modelling. (a) The column in the left shows the inversion results obtained for a 10 m x 10 m cell size. (b) The column in the right shows the inversion results obtained for 100 m x 100 m cell size.

Similarly, the three panels on the right-hand side (Figure 5.5b) display the result of the inversion for a 100 m x 100 m cell size discretization. For all cases, as shown in the figures, the density contrast values in the reconstructed model match with true values. Nevertheless, inversion without depth weighting shows a shallow anomaly irrespective of the true source depth. In other terms, the depth of the reconstructed model did not coincide with the true depth of the anomalous block. Moreover, the lateral extent of the anomalous body is not defined properly.

Figure 5.6 shows the inversion results for the case when the proposed depth weighting function is incorporated into the developed inversion algorithm. As can be seen from all the panels in Figure 5.6, unlike the results in Figure 5.5, the inversion using $w_{zn}(z)$ recovered the causative body sufficiently in all cases. No matter where the true source is placed, all the recovered models are at a reasonable location and coincide with the true model's shape and boundary adequately.

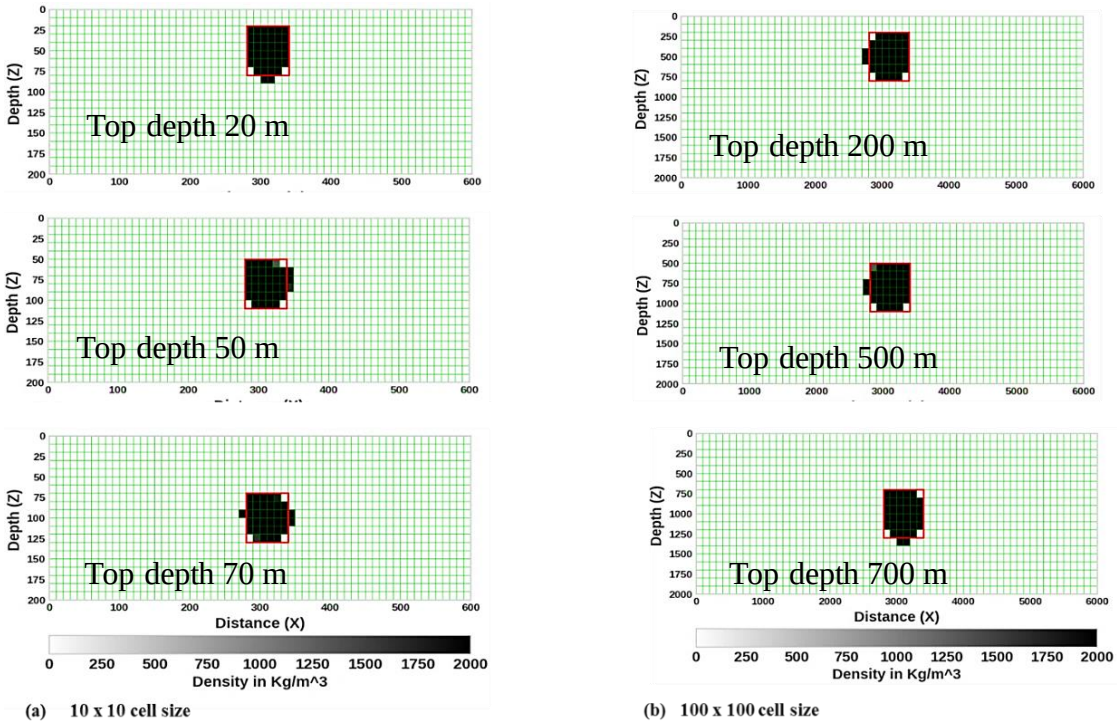

Figure 5.6: Results of synthetic data inversion, for anomalous rectangular shaped block, to illustrate the capabilities of the proposed depth weighting function $w_{zn}(z)$. The three rows are results from the inversion of the synthetic data, when the rectangular block, is placed at three different depths. The red solid line indicates the outlines of the true location of the causative body, which is used for the forward modelling. (a) The column in the left shows the inversion results obtained for a 10 m x 10 m cell size. (b) The column in the right shows the inversion results obtained for 100 m x 100 m cell size.

Furthermore, the recovered density contrast value also matches with the true density contrast of the models. The obtained results in turn show that the proposed depth weighting function is effective in placing the recovered model at a depth consistent with the true depth of the anomalous body and in reproducing the true shape and density. Moreover, as one can see from Figure 5.6, the reconstructed models of the causative bodies are compact and sharp as was required.

For the second example in this subsection, the anomalous source consists of two separate vertical and horizontal rectangular blocks. With this example, the resolving capability and the effectiveness of the method in recovering multiple causative bodies are illustrated. The anomalous bodies have different sizes and buried at different depths (see Figure 5.8 red dashed line). The density contrast of the horizontal and vertical blocks was set to be $2000\ \frac{kg}{m^3}$ and $3000\ \frac{kg}{m^3}$ respectively with zero background density. In this synthetic test, the 2D model domain is divided into 50 x 12 = 600 square cells. In order to test the functionality of the method, when large cell sizes are used, a cell size with a dimension of 400 m x 400 m is used in the *X* and *Z* directions, respectively. The gravity data were computed at the surface (Z = 0.0) on a total of 50 points with a sampling interval of 400 m. Later the computed data were contaminated using Gaussian noise, with zero mean and standard deviation that amounts to 4 % of the magnitude at each data point.

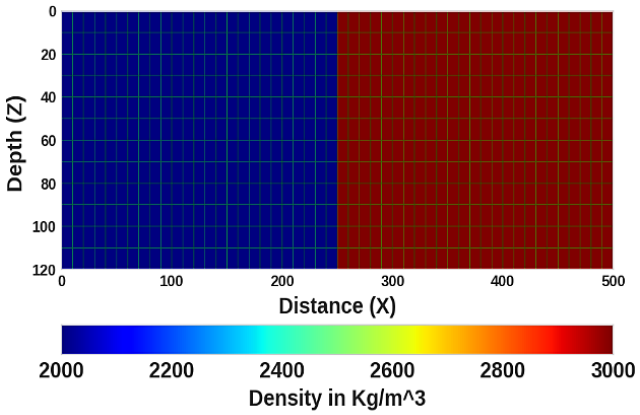

Figure 5.7: Upper density bound applied during the inversion of synthetic example which consists of two separate vertical and horizontal blocks at different depths.

The inversion was performed using the newly developed approach that utilizes the proposed depth weighting function $w_{zn}(z)$, which is given in equation 4.16. In

parallel a test has been made using the former depth weighting function $w_z(z)$ in equation 4.15 by putting $\beta = 3$. Here, during the inversion, the minimum density limits for the inequality constraint were chosen as $\boldsymbol{\rho}_{min} = 0.0$, and the maximum density limit $\boldsymbol{\rho}_{max}$ was given two different values for two different sections of the model domain. These maximum density values are $2000\ \frac{kg}{m^3}$ for the left section and $3000\ \frac{kg}{m^3}$ for the right section as shown in Figure 5.7. The initial value of μ^1 was set to 0.25. Even though, a maximum iteration of 20 was given at the commencement of the inversion, the inversion process has automatically terminated after 10 and 16 iterations in using $w_z(z)$ and $w_{zn}(z)$ repectively, because the proposed combined stopping criterion was attained. The obtained inversion results, including the outlines of the true boundary of the two blocks (red dashed line), are presented in Figure 5.8.

Figures 5.8a, presents the result obtained when using the former depth weighting function (equation 4.15) with $\beta = 3$. As shown in the figure lower panel, the algorithm recovered the source density and geometry sufficiently. This can suggest the possibility of using depth weighting function (equation 4.15) with $\beta = 3$. Notice that as compared to the shallower block the deeper block is better resolved. Thus, it better to use $\beta = 3$ for deeper sources, if one prefers to use the former weighing function. However, it should be noted that, in the real world the depth of the causative body cannot mostly be known a priori and it will be difficult to decide which value of β to use. The resulting fits between synthetic data (star dots) and calculated data (line) is at an acceptable level as shown in Figure 5.8a upper panel.

Figure 5.8b display the corresponding inversion result which is obtained using the proposed depth weighting function (equation 4.16), with all its parameter determined automatically. The inversion using $w_{zn}(z)$, as it can be seen from Figure 5.8b, recovered all the causative sources. The recovered causative bodies are at the depth consistent with the true depth and coincide with the true model's boundary adequately. Note that the shallower block is better resolved when compared to the result obtained using the former depth weighting function in equation 4.15 with $\beta = 3$. The recovered density contrast values also match with the true density of the models. In this case also, the resulting fits between synthetic data (star dots) and calculated data (solid line) is very good as shown in Figure 5.8b upper panel. Based on the results, the approach

described here is capable of producing physically realistic models, even if the model space is having variable densities at different depths.

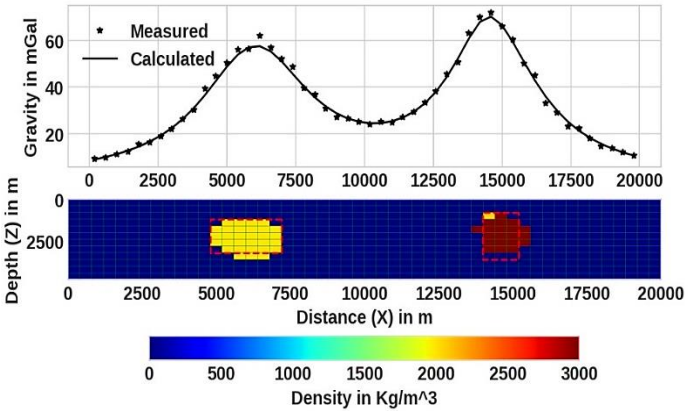

(a) Using $w_z(z)$ with $\beta = 3$

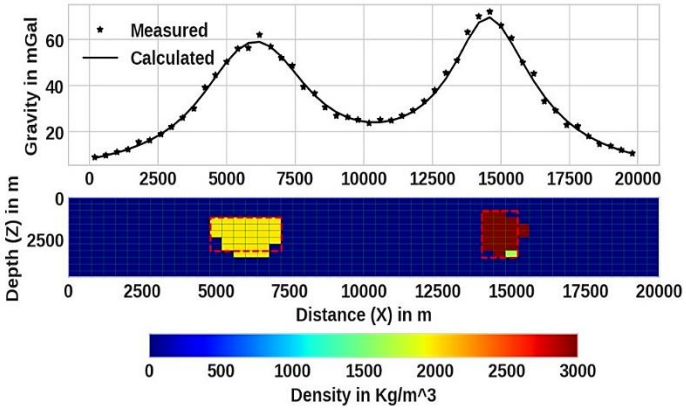

(b) Using $w_{zn}(z)$

Figure 5.8: Inversion results: lower panel showing the recovered density distribution of the synthetic source which consists of two separately placed vertical and horizontal blocks at different depths. The red dashed line indicates the outlines of the boundary of true anomaly. The top panel shows the corresponding fits between synthetic data (star dots) and computed data (solid line). The iterative step terminated when the proposed combined criterion is satisfied.

For the third example in this subsection, the synthetic source responsible for the gravity field consists of two oppositely oriented dipping dikes. The anomalous structures have different dimensions and located at different depths. The top of the first dike is placed at a depth of 40 m and its density contrast is $2000\ \frac{kg}{m^3}$ while the top of the second dike is placed at a depth of 20 m and has a density contrast of $3000\ \frac{kg}{m^3}$. The densities of the causative bodies are given relative to the zero density of the uniform background. In this synthetic test, the subsurface was discretized using a mesh of 60 x 15 square cells, and the dimension of each cell is set to 10 m x 10 m in the X and Z

directions, respectively. The gravity data is computed on 60 data points with a sample spacing of 10 m. The top panels of Figure 5.10, with star dots, show the gravity anomaly from these models after contaminating it with Gaussian noise with zero mean and standard deviation that amounts to 3% of the magnitude at each data point.

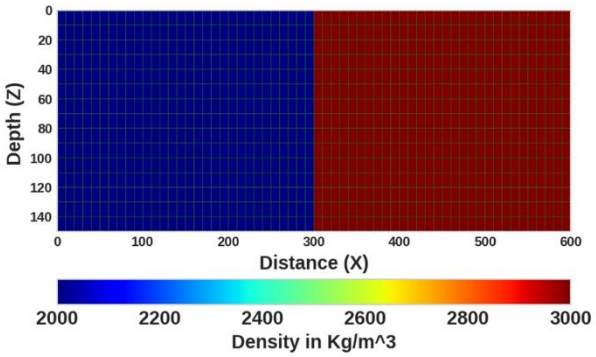

Figure 5.9: Upper density bound applied during the inversion of synthetic example which separate dike structures with different sizes, densities, and placed at different depths.

For the current synthetic example, the inversion process was commenced by setting the initial value of $\mu^1 = 0.2$. The inversion was again carried out separately using the former (equation 4.15) for three different β values and the proposed (equation 4.16) depth weighting functions. The parameters for the new depth weighting function are once again determined automatically. During the inversion, the lower density contrast limits for the inequality constraint were chosen as $\boldsymbol{\rho}_{min} = 0.0$, and the upper density contrast limit $\boldsymbol{\rho}_{max}$ was given two different values for two different sections of the model domain. These maximum density values are $2000\ \frac{kg}{m^3}$ for the left section and $3000\ \frac{kg}{m^3}$ for the right section as shown in Figure 5.9. Note that to compare old $w_z(z)$ with the proposed $w_{zn}(z)$, the same inversion parameters were taken during the inversion process for all considered cases

In Figure 5.10 the recovered density model overlain by the outlines of the boundaries of the true bodies and calculated data (solid line) are presented. As shown in Figure 5.10, panels a – c represents the result of the inversion process using different values β in the former function $w_z(z)$. The results of the three images depicted the importance choosing an appropriate value for β. For β =1 the shallower dike is resolved well and the deeper dike somewhat shifted up towards the surface (Figure 5.10a). In contrast, for β =2.5 the shallower dike is pushed down and the deeper dike is resolved

well (Figure 5.10c) but still the results can be considered as acceptable. This is similar to the case observed in previous example for $\beta = 3$. For $\beta = 2$ the inversion algorithm tends toward intermediate depths and gives relatively reasonable results with better resolution of the shallower and deeper dikes. The level of data fit for all inversions, using the existing function $w_z(z)$ with different values β are at an adequate level.

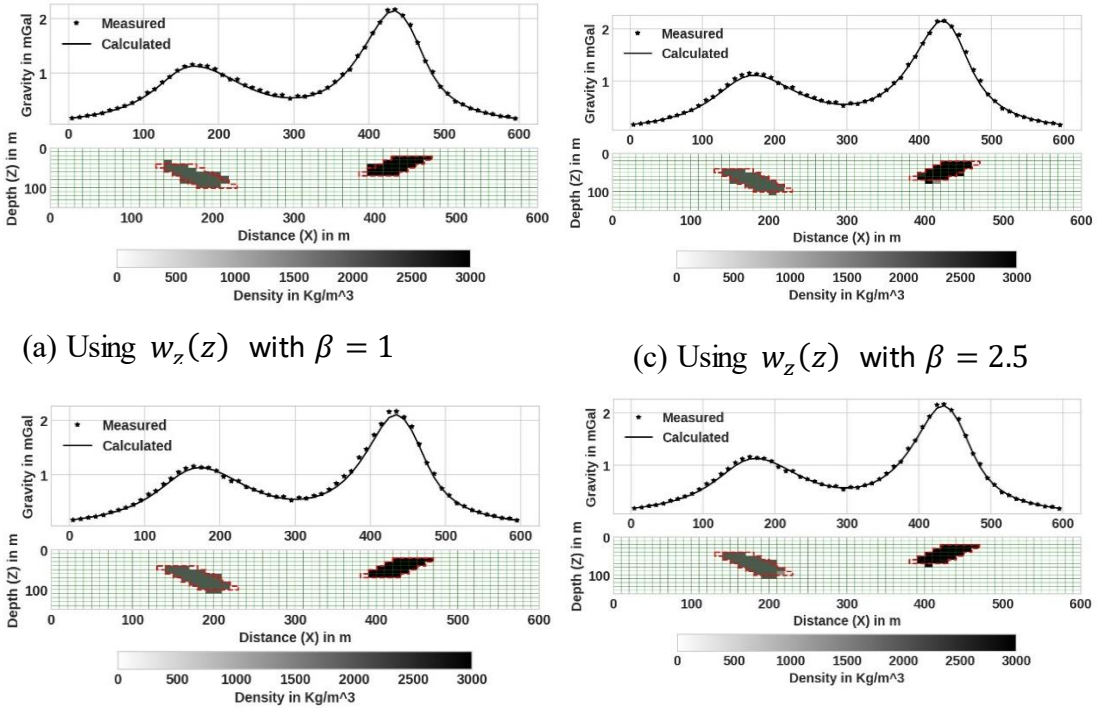

(a) Using $w_z(z)$ with $\beta = 1$

(c) Using $w_z(z)$ with $\beta = 2.5$

(b) Using $w_z(z)$ with $\beta = 2$

(d) Using $w_{zn}(z)$

Figure 5.10: Inversion results of gravity anomalies caused by two separate dike structures with different sizes, densities, dipping directions and placed at different depths. The outlines of the true causative bodies are indicated using the red dashed lines. (a), (b), and (c) show inversion results using $w_z(z)$ with β=1, 2 and 2.5 respectively and (d) shows the result when $w_{zn}(z)$ is being used. In all the panel the bottom shows the model domain and those on the top shows the data domain, with fits between the synthetic and calculated data.

Therefore, based on the synthetic tests in the last two examples and many other similar tests I for the first time propose the appropriate range of β values for gravity inversion be $1.0 < \beta \leq 3$ not $1.5 < \beta \leq 2$ as it is suggested by Li and Oldenburg (1998), if one prefers to use the depth weighting function given in equation 4.15. In addition, the results also suggest that a suitable precise value of β should be chosen depending on the depth of the anomalous source. In other words, small value of β for shallow depth anomalies and larger values for deeper, as stated by Li and Oldenburg (1996). This

however, can be materialized if we only have prior information about the depth of burial of the causative bodies. As mentioned in the previous sections and as per the result of the synthetic data inversion the major limitations of using $w_z(z)$ given in equation 4.15 is that: (I) the selection of the appropriate value of β through trial and error is tedious and challenging and (II) even if we are able to select the appropriate β value, the inversion algorithm may lead to an unrealistic solution when the anomalous sources are placed at depths different than the one anticipated in the a priori information, due to the difference in rate of decay between the kernel and the depth weighting function. This is also pointed out by Barbosa et al., (2002). The next paragraph explains how the newly proposed depth weighting function overcomes these drawbacks.

The recovered density contrast distributions, using the proposed function $w_{zn}(z)$ is given in Figure 5.10c. The location, geometry and densities of the synthetic causative bodies that were used to generate the synthetic gravity data are fully recovered as shown in the figure. In other terms, using the improved depth weighting function $w_{zn}(z)$ reproduces the subsurface causative bodies used to generate the synthetic data no matter where the sources are located. Therefore, the results obtained so far showed that the usage of the newly developed depth weighing function $w_{zn}(z)$ as given in equation 4.16, mitigate the problem that might arise by the inappropriate choice of β, when using the former depth weighing function through $w_z(z)$. Especially the function $w_{zn}(z)$ becomes even more advantageous when there is no a prior depth information, because all the parameters are determined automatically through optimization between the weighting function and the gravity kernel. This way of implementation of $w_{zn}(z)$ will avoid the inconvenience in choosing an appropriate β value and the process is not tedious. Finally, like the previous example the results of this example also confirm the capability of the method in producing compact and sharp models of localized multiple causative bodies.

The fourth synthetic model example in this subsection is rather more complicated in that it has three different geometric bodies that are placed at different depths, with different density values. The different shapes, dimensions, and depths of closely placed anomalous bodies have been considered to test the vertical and horizontal resolving power of the inversion method, and further demonstrate its capability to recover the true densities of multiple bodies. In solving the forward

problem, the top part of the first body, which is a horizontal rectangular block, is placed at 100 m depth and has a density contrast of $1000\frac{kg}{m^3}$. The second body is a vertical block and its top part is located at a depth of 200 m and has a density contrast that amounts to $2000\ \frac{kg}{m^3}$. The third body is a dipping dyke with a density contrast of $3000\ \frac{kg}{m^3}$ and its top part is located at a depth of 150 m. The densities of all the causative bodies are given relative to a zero density of a uniform background. In this synthetic test, the model space is constructed using 90 x 20=1800 square cells. Each cell has a size of 50 m in X and Z directions, which is different from the previous examples. The gravity data is then computed on 90 data points with a sample spacing of 50 m.

To demonstrate the strength of the method in recovering the true density, the noise-free data is first inverted. The inversion process was initialized by assigning an initial zero density to each cell and by setting the initial value of $\mu^1 = 10^{-4}$. The lower bound for the inequality constraint $\boldsymbol{\rho}_{min}$ is set to zero and the upper bound density constraint $\boldsymbol{\rho}_{max}$ was defined based on the location of the expected anomalous bodies, and these values are shown with different colors in Figure 5.11. The result of noise free data inversion is displayed Figure 5.12a. The model generated data (the black solid line) exactly fits the noise-free gravity data (the black stars) as presented on the top panel of Figure 5.12a. The corresponding density model, recovered using the improved inversion method is shown in Figure 5.12a lower panel. Once again, like the previous examples the inversion method is able to recover the true model completely.

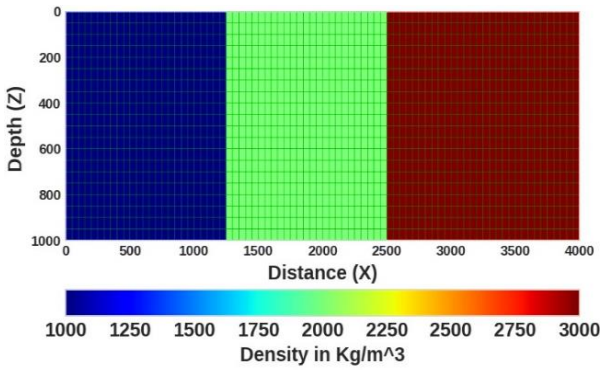

Figure 5.11: Upper density bounds applied during the inversion of the synthetic example which consists of three separate anomalous bodies having different shape and density contrast and located at different depths.

Later the computed gravity data was contaminated with uncorrelated Gaussian noise, with zero mean and a standard deviation that amounts to 3 % of the magnitude of the gravitational acceleration at each measurement point. This data is shown with black stars on the top panel of Figure 5.12b. Then, the inversion was performed using the newly developed algorithm. Similar to the previous examples, though the maximum number of iterations was set to be 20, the iterative step terminated when the proposed combined criterion is satisfied after 14 iterations. The recovered density contrast model together with the outlines of the true causative bodies (red dashed line) are presented in the lower panel of Figure 5.12b. The corresponding fits between synthetic (star dots) and calculated data (solid line) are shown in the upper panel of the same figure.

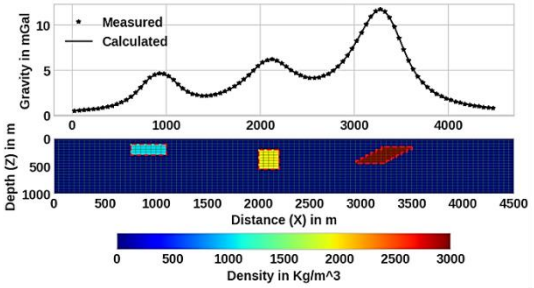

(a) The recovered model from noise free data and the corresponding data fit.

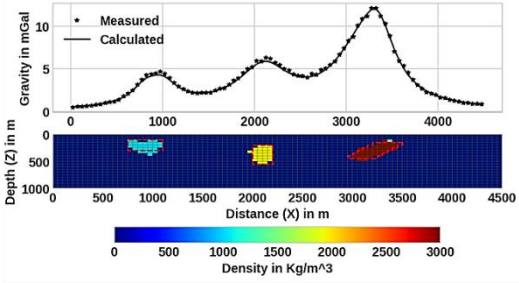

(b) The recovered model from noise contaminated data and the corresponding data fit.

Figure 5.12: The fourth example: synthetic data inversion results produced by three separate anomalous bodies having different shape and density contrast and located at different depths. The outlines of the true bodies are indicated by the red dotted lines in the recovered model. Where the top panel shows the corresponding fits between the synthetic and modeled data. Inversion was performed using the new depth weighting function $w_{zn}(z)$, and the iterative step terminated when the proposed combined criterion is fulfilled. (a) The inversion of noise free synthetic data, and (b) noise contaminated data.

As one can see from the Figure 5.12b, the level of the data fit is very good, even for the data that is contaminated with noise. Looking at the recovered density distributions, one can conclude that the inversion method has delivered an excellent result. Both depths to the top and bottom parts of the bodies and their horizontal extent and locations are determined adequately. The density contrasts of all the shallower and deeper sources are recovered sufficiently. The results from this example, therefore reconfirmed the capability of the method in recovering the subsurface causative multiple bodies that have different densities, shape, sizes, and locations. Additionally, the synthetic test results demonstrated the successful implementation of the developed inversion method in producing geologically reasonable sharp and compact results.

5.2.3 Synthetic model tests for the combined stopping criteria

The main aim of this subsection is to illustrate the performance and effectiveness of the proposed combined stopping criterion using synthetic model tests. The illustration is performed using two different synthetic test problems. Here, I reconsider the previous two synthetic model examples which consists of the Vertical and Horizontal Blocks (Figure 5.8), and three different shaped sources (Figure 5.12) as a first and second example (case) respectively.

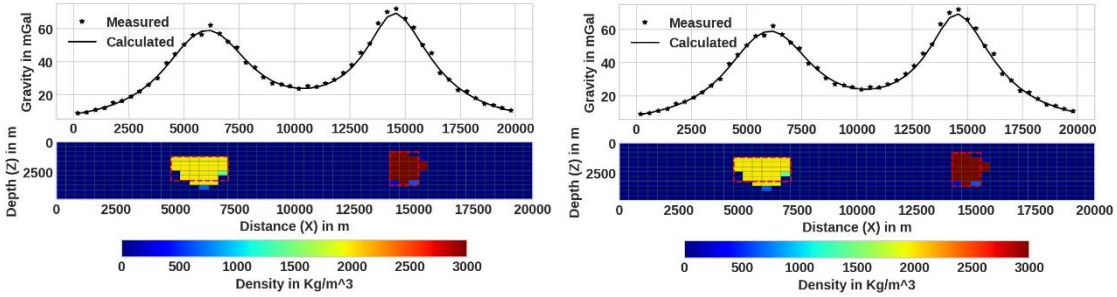

(a) Using only $|misfit^k| \leq \delta$ (b) Using only $|misfit^{k-1} - misfit^k| \leq \varphi$

Figure 5.13: Inversion results obtained using two commonly used criteria and the corresponding data fit (upper panels) for the synthetic example in Figure 5.8. (a) Using only $|misfit^k| \leq \delta$, (b) using only $|misfit^{k-1} - misfit^k| \leq \varphi$.

With this first example, the effectiveness of the proposed combined stopping criterion is illustrated by comparing it with other commonly used stopping conditions such as $|misfit^k| \leq \delta$, and its variation $|misfit^{k-1} - misfit^k| \leq \varphi$. For this example, the model shown in Figure 5.8 is reconsidered and the inversion process was performed again with the developed inversion method. Except for the stopping criteria, all the other inversion parameters are set the same as that given in subsection 5.2.2. The recovered density contrast models and the data fit as a result of using the two criteria separately are presented in Figures 5.13a and 5.13b. The corresponding values of the $misfit$ and smy as a function of iteration number are shown in Figures 5.14a and 5.14b. For comparison purpose, the $misfit$ and smy when using the combined stopping criterion for the same data set is also presented in Figure 5.14c. The model as a result of the newly developed inversion method, which makes use of the combined stopping criteria, is already presented in Figure 5.8b.

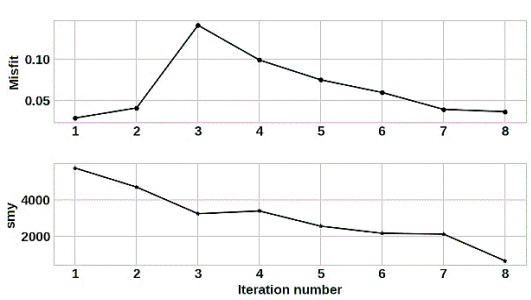

(a) Using $|misfit^k| \leq \delta$

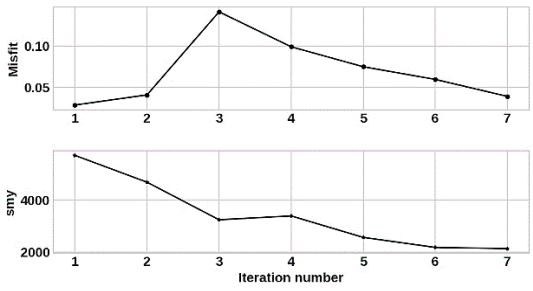

(b) Using only $|misfit^{k-1} - misfit^k| \leq \varphi$

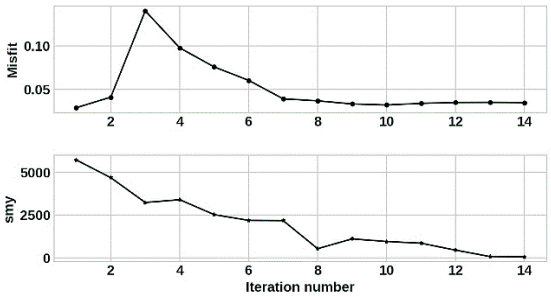

(c) Using the proposed combined

Figure 5.14: The misfit and smy values in the course of the iterative procedure during the inversion of the synthetic data given in Figure 5.8a. (a) When using the misfit ($|misfit^k| \leq \delta$) only, (b) its variation ($|misfit^{k-1} - misfit^k| \leq \varphi$) only, (c) when using the proposed combined stopping criterion.

The stopping condition $|misfit^k| \leq \delta$, where δ is the standard deviation of the Gaussian noise, was reached after 7 iterations, as shown in the curve of Figure 5.14a before the convergence of the solution. Similarly, the termination criterion $|misfit^{k-1} - misfit^k| \leq \varphi$ was fulfilled after 8 iterations (Figure 5.14b). As compared to the result presented in Figure 5.8b, where the proposed combined stopping condition is used, quitting the iterative process with $|misfit^k| \leq \delta$, and $|misfit^{k-1} - misfit^k| \leq \varphi$ criteria produces a premature solutions shown in Figures 5.13a and b respectively. In other words, unlike the combined stopping condition with which the iteration stopped at 14th iteration after convergence, the iterative process terminated at 7th and 8th iteration before the maximum compactness is achieved. In addition to the visual comparison of the obtained results, the RMS errors of the difference between the data and the predicted data, and the true and the recovered model density contrasts are considered as a measure of the quality of the solution to evaluate the performance of the three stopping criteria. Table 5.1 shows the number of iterations and the computed RMS errors associated with the obtained results from the implementation of the

developed method with the three stopping criteria. One can see from the table that the smallest RMS errors were encountered in the recovered inverse solutions with combined stopping criteria. This clearly shows the effectiveness of the proposed stopping criterion. Therefore, according to this result the proposed combined stopping criterion is effective in terminating the inversion process after optimal number of iterations, as compared to the commonly used stopping criteria.

Table 5.1 The number of iterations and the RMS errors obtained when applying the developed method with the three stopping criteria for the inversion of the synthetic example in Figure 5.8.

Stopping criterion	Number of iterations	RMS errors	
		$\sqrt{\frac{\sum_{i=1}^{N}(\boldsymbol{g}_i^{obs}-\boldsymbol{g}_i^{pre})^2}{N}}$	$\sqrt{\frac{\sum_{i=1}^{N}(\boldsymbol{\rho}_j^{tru}-\boldsymbol{\rho}_j^{reco})^2}{N}}$
$\lvert misfit^k \rvert \leq \delta$	7	1.0959	336.0249
$\lvert misfit^{k-1}\ misfit^k \leq \varphi$	8	0.9177	329.0065
Combined criterion	14	0.84056	321.5338

To further illustrate the effectiveness of the proposed criterion the iteration is allowed to continue to the 20th iteration and the model as result of this is presented in Figure 5.15b. The progression of the $misfit$ and smy in the course of the iterative procedure are shown Figure 5.15a. As it can be seen from the result (Figure 5.15b) the solution obtained at subsequent iterations, after 14th iteration where the iteration is terminated with proposed stopping condition, remain virtually unaltered. This can also be observed from the $misfit$ and smy variation curves shown in Figure 5.15a, in such that after 14th iteration the $misfit$ and smy values remain literally unchanged. Moreover, the results also indicate the appropriateness of the suggest threshold values μ and τ used in the proposed stopping criterion. The other thing one can observe from the results in Figure 5.15 is the stability of the developed inversion method. This can also illustrate the effectiveness of newly proposed auto-adaptive regularization technique (equation 4.14) and error weighting function (equation 4.10).

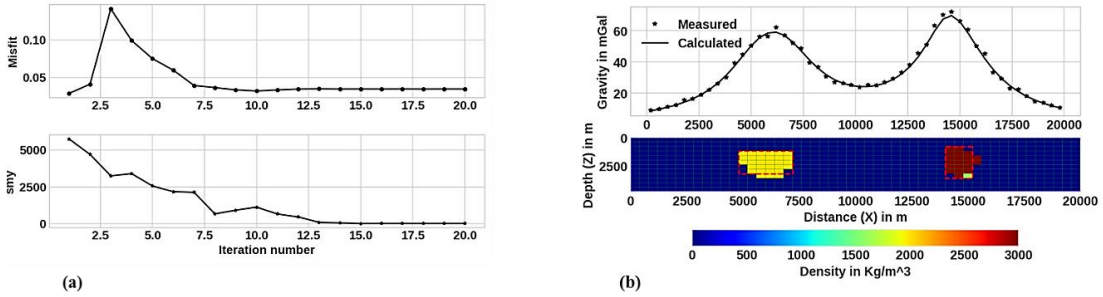

Figure 5.15: Late iteration termination (at 20th iteration) of the inversion result for the synthetic example in Figure 5.8. (a) The progression of the $misfit$ and smy in the course of the iterative process. (b) The obtained recovered density model (lower panel) and the corresponding data fit (upper panel).

The second example which is considered to illustrate the effectiveness of the proposed combined stopping criterion is the model shown in Figure 5.12. With this second example, the effectiveness of the proposed combined stopping criterion is illustrated by comparing the results obtained using only smy stopping condition $|smy^{k-1} - smy^{k}| \leq \tau$. For this purpose, the inversion process was repeated using the developed algorithm using only $|smy^{k-1} - smy^{k}| \leq \tau$ stopping condition. Note that, for comparison purpose the inversion parameters are set same, as given in section 5.2.2 where the inversion was performed with combined stopping criterion. The result of the inversion using only $|smy^{k-1} - smy^{k}| \leq \tau$ terminating condition is displayed in Figure 5.16. The corresponding progression history of the $misfit$ and

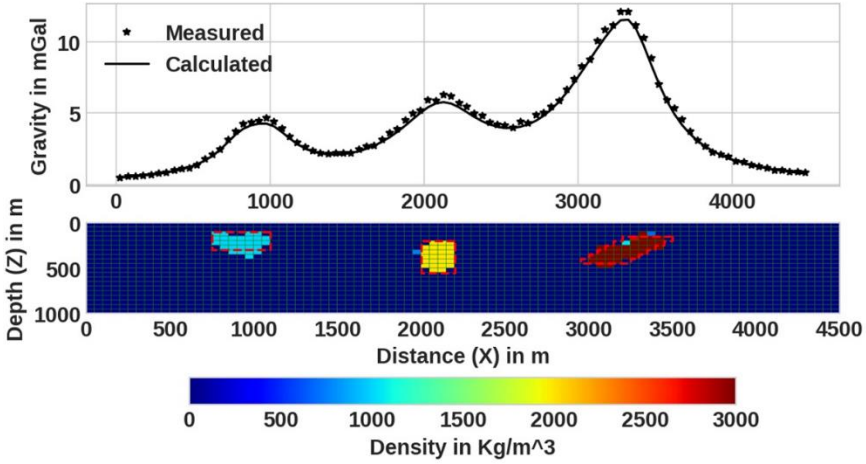

Figure 5.16: Inversion result of the synthetic data given in Figure 5.12, which is obtained through the newly developed inversion algorithm, but by only using $|smy^{k-1} - smy^{k}| \leq \tau$ stopping criterion. The top panel shows the data fit between measured and model generated data and lower panel shows the recovered density contrasts.

smy as a function of iteration number for only $|smy^{k-1} - smy^{k}| \leq \tau$ is shown in Figure 5.17a. For comparison purpose, the progression of the $misfit$ and smy for the proposed combined stopping condition, for which the corresponding results are displayed in Figure 5.12b is shown in Figure 5.17b.

As shown in Figure 5.17, the stopping condition $|smy^{k-1} - smy^{k}| \leq \tau$ is satisfied at 9th iteration before convergence. This can be clearly observed from Figure 5.16 where the maximum compactness of the recovered density distribution is not satisfactorily achieved. This result shows that, the usage of $|smy^{k-1} - smy^{k}| \leq \tau$ stopping criterion only might lead to a misleading information about the convergence the iterative procedure and the program might exit the iterative procedure before convergence, while the solution misfit is still large (as in Figure 5.17a). The inversion process stopped at the 9th iteration when the $|smy^{k-1} - smy^{k}| \leq \tau$ stopping criterion is used and at 14th iteration when the newly proposed criterion is used. By comparing the reconstructed models that are the result obtained after the 9th (Figure 5.16) and 14th (Figure 5.12b) iterations one can clearly notice the effectiveness of the proposed criterion. Besides, the visual inspection the two stopping criteria are evaluated by

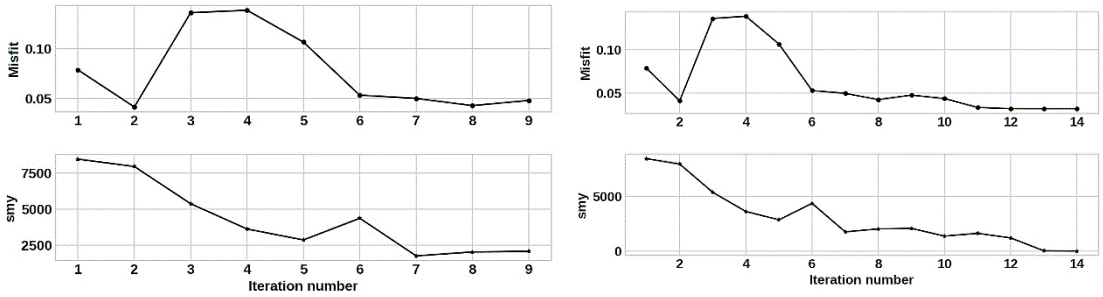

(a) Using only$|smy^{k-1} - smy^{k}| \leq \tau$ (b) Using the proposed combined criterion

Figure 5.17: The variation of the $misfit$ and smy in the course of the iterative process during the inversion of the synthetic data shown in Figure 5.12 using the newly proposed method. (a) Shows for $|smy^{k-1} - smy^{k}| \leq \tau$ criterion, for which the corresponding recovered density contrast model is shown in Figure 5.16. (b) Shows when the proposed combined stopping criterion is used, for which the corresponding recovered density contrast model is shown in Figure 5.12b.

comparing the RMS errors of the obtained results from applying the two stopping criteria. Table 5.2 displays the number of iterations and the RMS errors of each inversion. As it can be seen from the table, though nearly the same RMS error between the true and recovered density models were obtained, the lowest RMS error was

attained when the combined stopping criteria is used. This can also be considered as a prove to the effectiveness of the proposed stopping criterion.

Table 5.2 The number of iterations and the RMS errors of the obtained results with the two stopping criteria for the inversion of the synthetic example in Figure 5.12.

Stopping criterion	Number of iterations	RMS errors	
		$\sqrt{\frac{\sum_{i=1}^{N}(\boldsymbol{g}_i^{obs}-\boldsymbol{g}_i^{pre})^2}{N}}$	$\sqrt{\frac{\sum_{i=1}^{N}(\boldsymbol{\rho}_j^{tru}-\boldsymbol{\rho}_j^{reco})^2}{N}}$
$\lvert smy^{k-1}-smy^{k}\rvert \leq \tau$	9	0.2112	254.8115
Combined criterion	14	0.1573	252.0478

To demonstrate the effectiveness of the proposed criterion even further, like the pervious example, late termination (at 18th iteration) inversion result is displayed in Figure 5.18b. The corresponding variation of the misfit and smy in the course of the iterative scheme is shown Figure 5.18a. Based on the comparison between the results in Figures 5.18b and 5.12b, the inverse solutions obtained after the 14th iteration remain virtually unchanged. One can also see this by comparing the *misfit and smy* curves in Figures 5.17b and 5.18a. Again, one can also notice the stability of the method from Figure 5.18, which in turn confirms effectiveness and practicality of proposed auto-adaptive regularization technique (equation 4.14) incorporated in the developed inversion procedure.

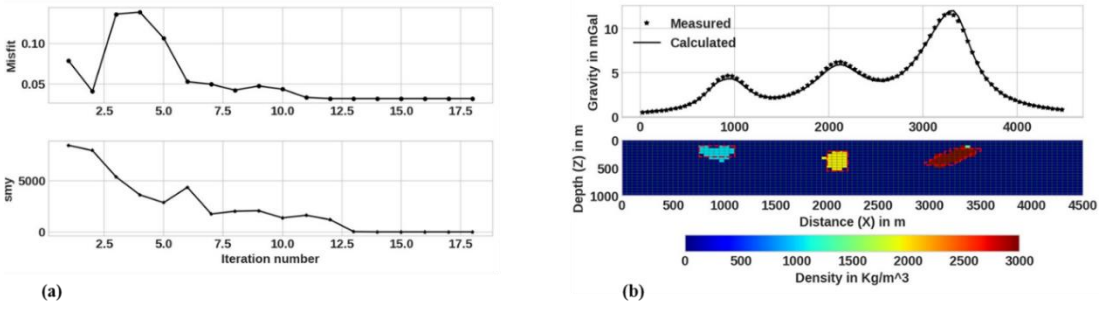

Figure 5.18: Late termination (at 18th iteration) inversion result for the synthetic example in Figure 10. (a) The variation of the *misfit* and *smy* in the course of the iterative scheme. (b) The obtained recovered density model (lower panel) and the corresponding data fit (upper panel).

In general, based on the results presented in this subsection and several other simulations for which results are not presented here the following remarks are made:

1. Implementing the commonly used stopping criterion that use the $misfit$ function solely may lead to neither a safe nor a robust solution (e.g. the iterative procedure may quit prematurely). As stated in section 4.9, it has been mentioned that the same has also be pointed out in number of previous works (e.g. Rao, et al., 2018).
2. Applying the smy function only may also give a misleading information about the convergence.
3. The proposed stopping criterion is effective and reliable in quitting the iterative scheme after optimal number of iterations. The suggest threshold values μ and τ are suitable. The other advantage of this technique is that it is relatively immune to the noise level in the data.

5.3 **Real Data Example**

In this section, we further illustrate the practicality and robustness of the proposed inversion approach using real data tests. For this purpose, the method is implemented in the inversion of distinct sets of gravity data measured over different geologic settings. The real data sets used here are from areas where the position and the characteristics of the targets are generally known. Consequently, the recovered density contrast models can be tested or compared directly against the known targets and an objective validation of the developed inversion algorithm can be made.

Woodlawn ore body

As a first field example, the gravity data that was collected over Woodlawn orebody, New South Wales, Australia (Templeton, 1981), has been inverted. The Woodlawn orebody, has a complex shape and it contains a massive sulfide deposit. Based on a priori information, the average estimated density of the footwall (host rock) ore is $2900\ \frac{kg}{m^3}$, and of the massive sulfide ore is of about $3900\ \frac{kg}{m^3}$. Hence, the target density contrast is equal to $1000\ \frac{kg}{m^3}$ which is the difference between host rock and the massive sulfides ore body. Further detail about the measurement and geology of the area can be referred in Whiteley (2016). Here, the residual anomaly data used to

perform the inverse modelling is obtained, by digitizing the data in Figure 7a of the paper by Last and Kubik (1983). The profile length is about 305 meters and the residual anomaly of this profile was digitized at regular intervals of 5 m producing a total of 61 measurement points. The top panel of Figure 5.19 displays this digitized residual anomaly, which is presented using star dots, over the Woodlawn massive sulfide ore body.

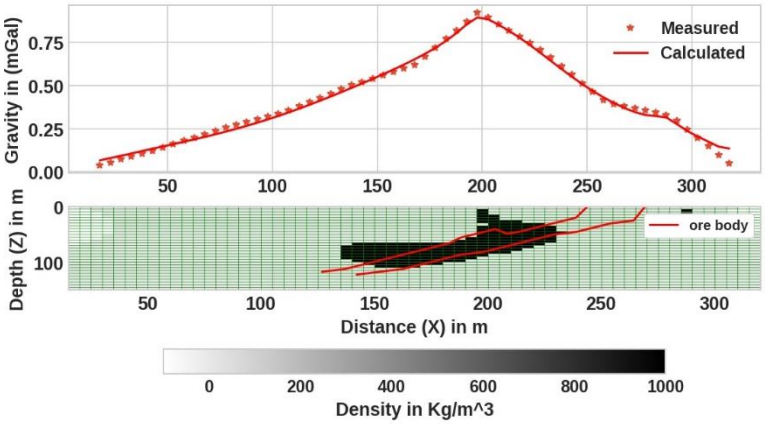

Figure 5.19: Inversion results of real gravity data from Woodlawn ore body, New South Wales (after Last and Kubik, 1981). The top panel shows the observed gravity data (red star dotes) and the calculated data from inverse model (solid line). The bottom panel on the other hand represents the recovered density model (squares field with black color) as a result of the newly developed inversion method and the outlines of the ore body indicated by the red solid line.

The subsurface model containing the ore body was discretized into 61 x 30 = 1830 rectangular cells with dimensions 5 x 5 m in the X- and Z-directions, respectively. Using the parameters described above under this subsection the newly developed method is implemented to invert the data. The inversion was started by using an initial value of $\mu^1 = 0.275$. Based on the prior information, the lower and the upper density bounds of the cells are taken as $\boldsymbol{\rho}_{min} = -100.0\ \frac{kg}{m^3}$ and $\boldsymbol{\rho}_{max} = 1000\ \frac{kg}{m^3}$. The given upper density bound is similar to the target density contrast. The maximum number of iterations was set to 20. In Figure 5.19 the final reconstructed density model and its gravity response using the proposed inversion methodology is displayed. Figure 5.19 top panel shows the fit between the observed data (red stars) and the gravity response of the density model resulted from the inversion process (red solid line). As one can see from the figure, there is a good agreement between the observed gravity data and the inverse model-generated data. The bottom panel in Figure 5.19 depicts, the final recovered density model together with the outlines (solid line) of the massive sulfide

ore body, which is verified by drilling (Templeton, 1981). As depicted in the figure, the recovered density distribution is compatible with the real density contrast of the subsurface that is obtained from prior information. The extent, position, and dip of the sulphide ore body are defined adequately except at the upper part of the ore body. As it can see from the data, this is due to the absence of high frequency information on the measured data at this particular location. The small misfit at the base might also be cause due to the reason that the measurement at the end of the profile were not continued until it asymptotically approaches a constant value and it has nothing to do with the inversion process. Therefore, this can be taken as additional evidence that the proposed method works properly and that it can effectively be applicable to real data.

East Bull gabbro-anorthosite complex

The second field example data was measured over East Bull Lake, Ontario, Canada (Paterson and Reeves, 1985). Figure 5.20 top panel displays the observed surface gravity anomaly (star dots) in this site. The maximum positive anomaly in the central part of the profile corresponds to gabbroic and anorthositic anomalous bodies. The background density which corresponds to the average density of the host rocks is given in their paper as $2650\ \frac{kg}{m^3}$. The gabbroic rock has the highest density $2930\ \frac{kg}{m^3}$ and the density of the anorthositic geological body is about $2850\ \frac{kg}{m^3}$ (Paterson & Reeves, 1985). This implies that the density contrasts of the target anomalous gabbroic and anorthositic rocks are 280 and $200\ \frac{kg}{m^3}$, respectively.

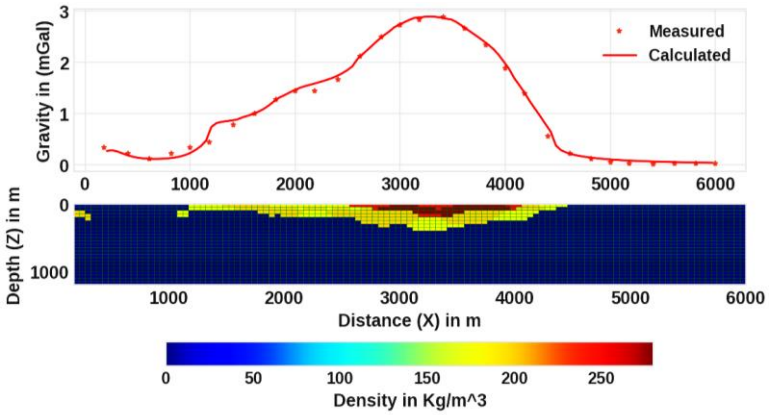

Figure 5.20: Field data from a survey at East Bull gabbro-anorthosite complex, Ontario, Canada (Paterson and Reeves, 1985), and the inversion result. Top panel: the observed (star dots) and calculated (solid line) gravity anomalies. Lower panel: the reconstructed density-contrast distribution of gabbroic and anorthositic geological units.

In order to carry out the inversion of the gravity data, the subsurface model was discretized into 24×117 regular cells that are having a dimension of 50 m in both the X and Z-directions. The developed inversion method was performed by setting the initial of $\mu^1 = 0.25$. To apply PPIC different minimum and maximum density contrasts bounds were assigned to different regions related to the specific anomalous sources. The minimum density contrast limits were calculated by subtracting a small density contrast value from the known target density contrast (Phillips, 2002 and Williams 2008). The known target density contrast values are assigned to be the maximum bound. Accordingly, the upper and lower bound for the density contrasts of the cells in the upper central part regions, where we expect the gabbroic rocks was assigned as $280\ \frac{kg}{m^3}$ and $252\ \frac{kg}{m^3}$ $(280 - 10\ \%)\ \frac{kg}{m^3}$ respectively. In the same way, for the cells where we anticipate the anorthositic rocks the maximum and minimum bounds were set to $200\ \frac{kg}{m^3}$ and $180\ \frac{kg}{m^3}$ respectively, and for the other part of the model space values of $200\ \frac{kg}{m^3}$ and 0.0 were used as upper and lower limit respectively.

The reconstructed density contrast model and the corresponding calculated anomaly are shown in Figure 5.20 lower panel and top panel respectively. As one can see from Figure 5.20 (upper panel) the calculated gravity anomaly (solid line) fits adequately with the observed data. The geometry and the spatial position (width and depth) of the reconstructed density contrast model (Figure 5.20 lower panel) of the gabbroic and anorthositic anomalous bodies, in general, agree with the results obtained by Paterson and Reeves (1985) and Silva and Barbosa (2006). This confirms the practicality of the suggested approach and also demonstrates that a geologically reasonable model can be obtained.

Guichon Creek batholith in south-central British Columbia

The last example for the real data inversion was taken from Green (1975) by carefully digitizing the residual gravity data. As it was given in Green (1975) the data was measured over the Guichon Creek batholith in south-central British Columbia. For the details about the measurement and geology the reader is referred to (Ager et al. (1973) and Ager (1972). The residual gravity profile is digitized at a regular interval of 0.5 km to produce a total of 64 data points as shown in Figure 5.21. For the inversion,

the source volume beneath the anomaly was divided into 64 x 22 square lattice with dimensions of each cell being 0.5 km in both X and Z-directions.

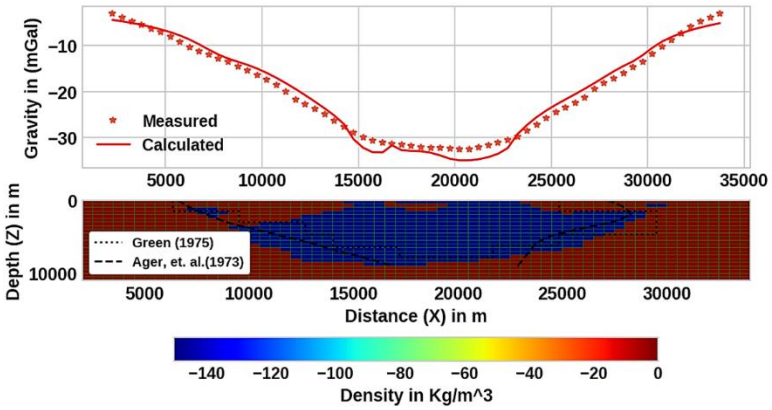

Figure 5.21: The observed gravity anomaly over Guichon Creek batholith in south-central British Columbia (after Green 1975) and its inversion result. Digitized data (star marks) with calculated data (solid line) shown on the top panel. Corresponding recovered density contrast model is shown on the bottom panel. For comparison, the results obtained by Ager (1973), which was obtained from drilling and Green (1975) are also presented.

The inversion was started with a homogeneous initial model in which every block has the same zero density and an initial μ^1 value of 0.48. In the course of the inversion process, based on the a prior information from Ager (1972), density values were constrained between the limits $\boldsymbol{\rho}_{min} = -150.0\ \frac{kg}{m^3}$ and $\boldsymbol{\rho}_{max} = 0.001\frac{kg}{m^3}$. The inversion was terminated after 9th iteration because the combined stopping criterion is fulfilled. The resulting model is presented in Figure 5.21. For comparison, the results obtained by Ager (1973) and Green (1975) are also included in Figure 5.21. The shape, real extent of the anomaly, and depth to bottom from the developed method are very close to the true geological feature (Ager et al., 1973) which was obtained from drilling. That means the implementation of the presented method resulted in a better solution compared to both Green (1975) and Ager (1973). Note that, this reasonable result is obtained by using only the density contrast limits as a prior information.

5.4 **Chapter Summary**

In this chapter, the practical implementation of the developed gravity inversion scheme presented in chapter 4 is discussed in two different sections. The tests focus on the major novel contributions incorporated to the method.

In the first section, prior to applying the developed inversion algorithm to real data sets its practicability, robustness and effectiveness were investigated and demonstrated on a number of synthetic data sets from different geological models. The presented synthetic inversion results by means of the developed method indicate that the algorithm is capable of producing compact and sharp images, and hence can give reliable reconstructions which delineate the subsurface multiple localized non-smooth structures adequately. The obtained results also show that the developed inversion technique is stable, even when the data is contaminated with different noise levels. Further, the obtained results also confirm the applicability and effectiveness of the novel contributions incorporated in the method.

In the second section of this chapter the proposed method is applied to invert three separate gravity data sets from various geologic settings and complexities. Based on the inversion results, the validity of the technique for practical applications has been successfully illustrated. The reconstructed models of the investigated real data are found to be conformal with that information derived from drilling. Furthermore, the testing of the new inversion approach using real gravity data also confirmed the potential and practicality of the method in producing compact and sharp images of the subsurface.

CHAPTER 6: CONCLUSION AND RECOMENDATIONS

6.1 Conclusion

The main objective of this Ph.D. thesis was the development of a gravity inversion algorithm that can recover sharp discontinuities and blocky features such as ore bodies, lithologic units separated by structures, dikes, subsurface cavities, magma chambers or in general formations of localized bodies in the subsurface. In the course of the thesis work, this goal has been achieved through the development of gravity inverse modelling method.

From the scientific point of view, the newly presented gravity inversion method, which is well described in Chapter 4, has the central position in the thesis. The developed method is based on an L_0-norm minimization of the objective function, which consists of L_2-norm data misfit function and L_0-norm stabilizing function, through the IRLS algorithm. The method incorporates an auto-adaptive regularization technique, which automatically determines a suitable regularization parameter at every iteration, and an error weighting function that helps to improve both the stability and convergence of the method. One of the strongest sides of the proposed auto-adaptive regularization and error weighting matrix is that they are not dependent on a priori knowledge of the noise level. Because of that, the method can yield reasonable results even when the noise level of the data is not known properly.

The other contribution of this work is the newly introduced depth weighting function that neutralizes the natural decay of the kernel function in a much better way than the traditional function so that the inversion results can provide realistic depth information. A crucial feature of the proposed depth weighting function is the automated determination of its parameters using a standard optimization method before the inversion process is commenced. This new method has a significant advantage over the older one in such that it avoids the selection of the parameter β through trial and error especially whenever there is no a priori depth information about the causative body.

Yet another important result of this work is the development of the PPICA algorithm, which is an efficient algorithm that is meant to impose the physical inequality constraints on density contrasts that are obtained as a result of the inversion

process. In contrast to previous work in compact gravity inversion, the PPICA allows the enforcement of localized density constraints at different localities of the model space to allow the recovery of multiple causative bodies having different densities. Another advantage of this algorithm is the possibility of assigning different density values for the upper and lower bounds.

The utilization of an effectively combined stopping rule to terminate the inversion process after an optimal number of iterative steps is another improvement that is introduced in this work.

In order to test the applicability, robustness, and capabilities of the newly developed method in producing the desired compact and sharp images it has been applied on both synthetic and measured data sets. Here it should be noted that these tests can also be considered as a validation test. Firstly, the presented inversion approach was applied on numerous synthetic gravity data sets that are imitating different geological scenarios. From these, few randomly chosen synthetic examples were presented in Chapter 5. The presented synthetic examples comprise models from a single causative body to multiple anomalous bodies having different geometry (size and shape), depth of burial and density contrast.

Based on the comparison of the recovered density contrast model with the true synthetic model the following concluding remarks were made. In the case of noise-free data inversion, the algorithm has successfully reproduced the actual model completely. The corresponding observed data and predicted response are exactly coincident with each other. The obtained results from the tests, when the input data is contaminated with different noise levels which are commonly encountered during real data measurement, confirmed the robustness and stability of the developed inversion method. Thereby indicate the effectiveness of the new method. The inversion of synthetic noise contaminated data sets from multiple and complicated geometry sources revealed the effectiveness of the method in such that it has successfully recovered the causative subsurface densities that were used to generate the synthetic gravity data. The results also revealed the efficiency of the method and its resolution capability in the vertical and lateral directions no matter where the true sources were placed. As a result of this, the applicability and effectiveness of the proposed depth weighting function can also be verified. The result of the test on synthetic data also showed the effectiveness and

efficiency of the proposed combined stopping criterion, as compared to the commonly used stopping criteria, in such that it terminates the inversion process after an optimal number of iterations.

After the method was tested with synthetic data, an additional test was made using published real gravity data sets measured over different geologic settings, to test its performance. The real data sets were from areas where the shape, location and physical characteristics of the causative subsurface bodies are generally known (e.g. from drilling). Thus, the obtained results from the inversion were easily compared directly against the known targets for verification purposes. Similar to the synthetic case, here also the obtained inversion results proved the effectiveness of the method in producing geologically viable models. Moreover, the recovered models demonstrated that the developed approach is stable and effective in resolving localized sharp subsurface futures with acceptable resolving capacity. From this, the practicality of the developed inversion method is also confirmed.

In summary, the presented non-smooth gravity inversion algorithm has been tested with synthetic and real data sets. Based on the analysis of the obtained results the method is proved to be effective and efficient in recovering the density contrast and resolve subsurface causative bodies that are placed near to each other both vertically and laterally. Further, the inversion results also confirm the method's capability to produce compact and sharp images that define the shape and extent of the anomalous geological bodies adequately. By this, the reliability effectiveness and efficiency of the developed non-smooth inversion method in practical applications, to delineate sharp discontinuities and blocky features, which is the objective of the thesis, is confirmed.

6.2 **Recommendations for Future Work**

In the course of this Ph.D. thesis work, I have identified several areas of further research that may improve the presented method. Therefore, what follows is the recommendations to future improve and extend the newly developed method.

- It is noted that the selection of the initial value μ^1 is very crucial in determining the final model. Therefore, further investigation should be carried out to determine the optimum initial μ^1 value, particularly when the noise level is not known.

- Since the applicability of the developed method is tested using self-developed codes and its potential applicability is foreseeable, it will be very useful to extend it to a user-friendly software.
- The method is already proved to be effective and efficient for 2D modelling and it is believed that it can easily be extended to 3D gravity modeling. Therefore, it is recommended to test the method for 3D modelling.
- IRLS minimization method, which is the core of the presented inversion scheme, is a popular approach provably achieves superior performance in a wide range small scale application. However, IRLS involves a matrix inversion at each iteration, which prohibits its application to large scale practical problems. Addressing this issue can be one possible research direction in the future.

References

Acar, R., & Vogel, C. R. (1994). Analysis of bounded variation penalty methods for ill-posed problems. *Inverse problems, 10*(6), 1217.

Ager, C. A. (1972). *A gravity model for the guichon creek batholith (Doctoral dissertation, University of British Columbia).*

Ager, C. A., Ulrych, T. J., & McMillan, W. J. (1973). A gravity model for the Guichon Creek batholith, south-central British Columbia. *Canadian Journal of Earth Sciences, 10*(6), 920-935.

Ajo-Franklin, J. B., Minsley, B. J., & Daley, T. M. (2007). Applying compactness constraints to differential traveltime tomography. *Geophysics, 72*(4), R67-R75.

Al-Chalabi, M. (1971). Some studies relating to nonuniqueness in gravity and magnetic inverse problems. *Geophysics , 36*(5), 835-855.

Aster, R. C., Borchers, B., & Thurber, C. H. (2018). *Parameter estimation and inverse problems.* Elsevier.

Ba, D., Babadi, B., Purdon, P. L., & Brown, E. N. (2013). Convergence and stability of iteratively re-weighted least squares algorithms. *IEEE Transactions on Signal Processing, 62*(1), 183-195.

Barbosa, V. C., & Silva, J. B. (1994). Generalized compact gravity inversion. *Geophysics, 59*(1), 57-68.

Barbosa, V. C., & Silva, J. B. (2006). Interactive 2D magnetic inversion: A tool for aiding forward modeling and testing geologic hypotheses. *Geophysics, 71*(5), L43-L50.

Barbosa, V. C., Silva, J. B., & Medeiros, W. E. (2002). Practical applications of uniqueness theorems in gravimetry: Part II—Pragmatic incorporation of concrete geologic information. *Geophysics, 67*(3), 795-800.

Barbosa, Valeria Cristina F., Joao BC Silva, and Walter E. Medeiros. (1997). Gravity inversion of basement relief using approximate equality constraints on depths. *Geophysics , 62*(6), 1745-1757.

Bassrei, A., Terra, F. A., & Santos, E. T. (2007). Application of the L-curve in geophysical inverse problems: methodologies for the extraction of the optimal parameter. *AGUFM*, S23B-1378.

Bertete-Aguirre, H., Cherkaev, E., & Oristaglio, M. (2002). Non-smooth gravity problem with total variation penalization functional. *Geophysical Journal International, 149*(2), 499-507.

Blakely, R. J. (1996). *Potential theory in gravity and magnetic applications*. Cambridge university press.

Borges, L. S., Baz´an, F. S., & Cunha, M. C. (2015). Automatic stopping rule for iterative methods in discrete ill-posed problems. *Computational and Applied Mathematics, 34*(3), 1175 – 1197.

Boulanger, O and Chouteau, M. (2001). Constraints in 3d gravity inversion. Geophysical prospecting. *49*, 265-280.

Boyd, S. P., & Vandenberghe, L. (2004). *Convex optimization*. Cambridge university press.

Cai, Y., & Li, S. (2017). Convergence and stability of iteratively reweighted least squares for low-rank matrix recovery. *Inverse Problems & Imaging, 11*(4), 643.

Camacho, A. G., F. G. Montesinos, and R. Vieira. (1997). A three-dimensional gravity inversion applied to São Miguel Island (Azores). *Journal of Geophysical Research: Solid Earth, 102*(B4), 7717-7730.

Camacho, A. G., Montesinos, F. G., & Vieira, R. (2002). A 3-D gravity inversion tool based on exploration of model possibilities. *Computers & Geosciences, 28*(2), 191-204.

Camacho, Antonio G., Fuensanta G. Montesinos, and Ricardo Vieira. (2000). Gravity inversion by means of growing bodies. *Geophysics , 65*(1), 95-101.

Caratori Tontini, F., Cocchi, L., & Carmisciano, C. (2009). Rapid 3-D forward model of potential fields with application to the Palinuro Seamount magnetic anomaly (southern Tyrrhenian Sea, Italy) . *Journal of Geophysical Research: Solid Earth*, 114(B2).

Cardarelli, E., & Fischanger, F. (2006). 2D data modelling by electrical resistivity tomography for complex subsurface geology. *Geophysical Prospecting, 54*(2), 121-133.

Carmi, A. Y., Mihaylova, L., & Godsill, S. J. (2014). *Compressed sensing & sparse filtering*. Springer Berlin Heidelberg.

Carrillo, R. E., & Barner, K. E. (2009). Iteratively re-weighted least squares for sparse signal reconstruction from noisy measurements. *2009 43rd Annual Conference on Information Sciences and Systems* (pp. 448-453). IEEE.

Cella, F., & Fedi, M. (2012). Inversion of potential field data using the structural index as weighting function rate decay. *Geophysical Prospecting, 60*(2), 313–336.

Chartrand, R., & Yin, W. (2008). Iteratively reweighted algorithms for compressive sensing. . *In 2008 IEEE international conference on acoustics, speech and signal processing* (pp. 3869-3872). IEEE.

Chen, G. X., Chen, S. C., Wang, H. C., & Zhang, B. (2013). Geophysical data sparse reconstruction based on L0-norm minimization. *Applied Geophysics, 10*(2), 181-190.

Chen, L., & Lanbo, L. (2019). Fast and accurate forward modelling of gravity field using prismatic grids. *Geophys. J. Int., 216*, 1062–1071.

Chen, S. S., Donoho, D. L., & Saunders, M. A. (2001). Atomic decomposition by basis pursuit. *SIAM review, 43*(1), 129-159.

Chen, X., Xu, F., & Ye, Y. (2010). Lower bound theory of nonzero entries in solutions of \ell_2-\ell_p minimization. *SIAM Journal on Scientific Computing, 32*(5), 2832-2852.

Commer, M. (2011). Three-dimensional gravity modelling and focusing inversion using rectangular meshes. *Geophysical Prospecting, 59*(5), 966–979.

Commer, M., & Newman, G. A. (2008). New advances in three-dimensional controlled-source electromagnetic inversion. *Geophysical Journal International, 172*(2), 513-535.

Cotter, S. F., & Rao, B. D. (2002). Sparse channel estimation via matching pursuit with application to equalization. *IEEE Transactions on Communications, 50*(3), 374-377.

Čuma, M., Wilson, G. A., & Zhdanov, M. S. (2012). Large-scale 3D inversion of potential field data. *Geophysical Prospecting, 60*(6), 1186-1199.

D'Urso, M. G. (2014). Analytical computation of gravity effects for polyhedral bodies. *Journal of Geodesy, 88*(1), 13-29.

Daubechies, I., Defrise, M., & De Mol, C. (2004). An iterative thresholding algorithm for linear inverse problems with a sparsity constraint. *Communications on Pure and Applied Mathematics: A Journal Issued by the Courant Institute of Mathematical Science, 57*(11), 1413-1457.

Daubechies, I., DeVore, R., Fornasier, M., & Güntürk, C. S. (2010). Iteratively reweighted least squares minimization for sparse recovery. *Communications on*

Pure and Applied Mathematics: A Journal Issued by the Courant Institute of Mathematical Sciences, 63(1), 1-38.

Do, T. T., Gan, L., Nguyen, N., & Tran, T. D. (2008). Sparsity adaptive matching pursuit algorithm for practical compressed sensing. *In 2008 42nd Asilomar Conference on Signals, Systems and Computers* (pp. 581-587). IEEE.

Donoho, D. L. (2006). For most large underdetermined systems of linear equations the minimal l1-norm solution is also the sparsest solution. *Communications on Pure and Applied Mathematics: A Journal Issued by the Courant Institute of Mathematical Sciences*.

Dubois, P. F., Hinsen, K., & Hugunin, J. (1996). Numerical python. *Computers in Physics, 10*(3), 262-267.

Ekanadham, C., Tranchina, D., & Simoncelli, E. P. (2011). Recovery of sparse translation-invariant signals with continuous basis pursuit. *IEEE transactions on signal processing, 59*(10), 4735-4744.

Ekinci, Y. L. (2008). 2D focusing inversion of gravity data with the use of parameter variation as a stopping criterion. *Journal of the Balkan geophysical society, 11*(1), 1–9.

Elad, M. (2010). *Sparse and redundant representations: from theory to applications in signal and image processing*. Springer Science & Business Media.

Esser, E., Guasch, L., van Leeuwen, T., Aravkin, A. Y., & Herrmann, F. J. (2018). Total variation regularization strategies in full-waveform inversion. *SIAM Journal on Imaging Sciences, 11*(1), 376-406.

Fan, Z., Ni, M., Zhu, Q., Sun, C., & Kang, L. (2015). L0-norm sparse representation based on modified genetic algorithm for face recognition. *Journal of Visual Communication and Image Representation, 28*, 15–20.

Fang, H., & Zhang, H. (2014). Wavelet-based double-difference seismic tomography with sparsity regularization. *Geophysical Journal International, 199*(2), 944-955.

Farquharson, C. G., & Oldenburg, D. W. (1998). Non-linear inversion using general measures of data misfit and model structure. *Geophysical Journal International, 134*(1), 213-227.

Farquharson, C. G., & Oldenburg, D. W. (2004). A comparison of automatic techniques for estimating the regularization parameter in non-linear inverse problems. *Geophys. J. Int.*, 411–425.

Farquharson, C. G., Ash, M. R., & Miller, H. G. (2008). Geologically constrained gravity inversion for the Voisey's Bay ovoid deposit. *The Leading Edge, 27*(1), 64-69.

Farquharson, G. C. (2008). Constructing piecewise-constant models in multidimensional minimum-structure inversions. *Geophysics, 73*(1), K1–K9.

Fedi, M., Hansen, P. C., & Paoletti, V. (2007). Ambiguity and depth resolution in potential field inversion. *In Communications to SIMAI Congress, 2*.

Fei, Z., Chunhui, T., Tao, W., Zhaofa, Z., & Cai, L. (2018). 3D focused inversion of near-bottom magnetic data from autonomous underwater vehicle in rough seas. *Ocean Science Journal*, 405-412.

Feng, X., Liu, S., Guo, R., Wang, P., & Zhang, J. (2020). Gravity Inversion of Blocky Basement Relief Using L0 Norm Constraint with Exponential Density Contrast Variation. *Pure and Applied Geophysics*, 1-15.

Fournier, D., & Oldenburg, D. W. (2019). Inversion using spatially variable mixed ℓ p norms. *Geophysical Journal International, 218*(1), 268-282.

Fournier, D., Heagy, L. J., & Oldenburg, D. W. (2020). Sparse magnetic vector inversion in spherical coordinates. *Geophysics, 85*(3), J33-J49.

Fuhry, M., & Reichel, L. (2012). A new Tikhonov regularization method. *Numerical Algorithms, 59*(3), 433-445.

Gao, X., Bai, Y., & Li, Q. (2019). A sparse optimization problem with hybrid $$ L_2 {\text {-}} L_p $$ L2-Lp regularization for application of magnetic resonance brain images. *Journal of Combinatorial Optimization*, 1-25.

Ghalehnoee, M. H., Ansari, A., & Ghorbani, A. (2016). Improving compact gravity inversion based on new weighting functions. *Geophysical Journal International*, ggw413.

Gholami, A., & Aghamiry, H. S. (2017). Iteratively re-weighted and refined least squares algorithm for robust inversion of geophysical data. *Geophysical Prospecting, 65*, 201-215.

Gholami, A., & Gheymasi, H. M. (2016). Regularization of geophysical ill-posed problems by iteratively re-weighted and refined least squares. *Computational Geosciences, 20*(1), 19-33.

Gorodnitsky, I. F., & Rao, B. D. (1997). Sparse signal reconstruction from limited data using FOCUSS: A re-weighted minimum norm algorithm. *IEEE Transactions on signal processing, 45*(3), 600-616.

Götze, H. J., & Lahmeyer, B. (1988). Application of three-dimensional interactive modeling in gravity and magnetics. *Geophysics, 53*(8), 1096-1108.

Grandis, H., & Dahrin, D. (2014). Constrained two-dimensional inversion of gravity data. *Journal of Mathematical and Fundamental Sciences*, 1-13.

Grayson, J. E. (2000). *Python and Tkinter programming*. Manning Publications Co. Greenwich.

Green, W. R. (1975). Inversion of gravity profiles by use of a Backus-Gilbert approach. *Geophysics, 40*(5), 763-772.

Grombein, T., Seitz, K., & Heck, B. (2013). Optimized formulas for the gravitational field of a tesseroid. *Journal of Geodesy, 87*(7), 645-660.

Guillen, A., & Menichetti, V. (1984). Gravity and magnetic inversion with minimization of a specific functional. *Geophysics, 49*(8), 1354-1360.

Guitton, A., & Symes, W. W. (2003). Robust inversion of seismic data using the Huber norm. *Geophysics, 68*(4), 1310-1319.

Guo, Q., Ruan, G., & Liao, Y. (2017). A time-frequency domain underdetermined blind source separation algorithm for mimo radar signals. *Symmetry, 9*(7), 104.

Han, J., Sun, Z., & Hao, H. (2015). L0-norm based structural sparse least square regression for feature selection. *Pattern Recognition, 48*, 3927–3940.

Hansen, P. C. (2001). The L-curve and its use in the numerical treatment of inverse problems. Computational Inverse Problems in Electrocardiology. *Advances in Computational Bioengineering, 5*(119).

Hansen, P. C. (1998). *Rank-deficient and discrete ill-posed problems: numerical aspects of linear inversion*. Society for Industrial and Applied Mathematics.

Hansen, P. C., & O'Leary, D. P. (1993). The use of the L-curve in the regularization of discrete ill-posed problems. *SIAM journal on scientific computing, , 14*(6), 1487-1503.

He, Z., Cichocki, A., Zdunek, R., & Xie, S. (2008). .Improved FOCUSS method with conjugate gradient iterations. *IEEE transactions on signal processing, 57*(1), 399-404.

Heck, B., & Seitz, K. (2007). A comparison of the tesseroid, prism and point-mass approaches for mass reductions in gravity field modelling. *Journal of Geodesy, 81*(2), 121-136.

Hinze, W. J., Von Frese, R. R., & Saad, A. H. (2013). *Gravity and magnetic exploration: Principles, practices, and applications*. Cambridge University Press.

Hirt, C., & Kuhn, M. (2012). Evaluation of high-degree series expansions of the topographic potential to higher-order powers. *J. Geophys Res, 117*, B12407.

Hirt, C., & Kuhn, M. (2014). Bandlimited topographic mass distribution generates full-spectrum gravity field: Gravity forward modeling in the spectral and spatial domains revisited. *J. Geophys Res. Solid Earth, 119*, 3646–3661.

Holstein, H. S. (1999). Comparison of gravimetric formulas for uniform polyhedra. *Geophysics, 64*(5), 1438-1446.

Hu, M., Yu, P., Rao, C., Zhao, C., & Zhang, L. (2019). 3D sharp-boundary inversion of potential-field data with an adjustable exponential stabilizing functional. *Geophysics, 84*(4), J1-J15.

Huang, S., & Tran, T. D. (2018). Sparse signal recovery via generalized entropy functions minimization. *IEEE Transactions on Signal Processing, 67*(5), 1322-1337.

Huber, P. J. (1964). Robust estimation of a location parameter. *Annals of Mathematical Statistics, 35*, 73–101.

Hunter, J. D. (2007). Matplotlib: A 2D graphics environment. *Computing in science & engineering, 9*(3), 90-95.

Hurley, N., & Rickard, S. (2009). Comparing measures of sparsity. *IEEE Transactions on Information Theory, 55*(10), 4723-4741.

Ji, S., Zhang, H., Wang, Y., Rong, L., Shi, Y., & Chen, Y. (2019). Three-dimensional inversion of full magnetic gradient tensor data based on hybrid regularization method. *Geophysical Prospecting, 67*(1), 226-261.

Jiang, W., & Zhang, J. (2017). First-arrival traveltime tomography with modified total-variation regularization. *Geophysical Prospecting,, 65*(5), 1138-1154.

Kilmer, M. E., & O'Leary, D. P. (2001). Choosing regularization parameters in iterative methods for ill-posed problems. *SIAM Journal on matrix analysis and applications, 22*(4), 1204-1221.

Kim, H. J., S. Y., & Lee, K. H. (1999). Inequality constraint in least-squares inversion of geophysical data. *Earth, planets and space, 51*(4), 255-259.

Kolehmainen, V., Lassas, M., Niinimäki, K., & Siltanen, S. (2012). Sparsity-promoting Bayesian inversion. *Inverse Problems, 28*(2), 025005.

Kuhn, M., & Seitz, K. (2005). Comparison of Newton's integral in the space and frequency domains. *In A Window on the Future of Geodesy*, 386-391.

Lai, M. J., & Wang, J. (2011). An Unconstrained \ell_q Minimization with 0q\leq1 for Sparse Solution of Underdetermined Linear Systems. *SIAM Journal on Optimization, 21*(1), 82-101.

Lai, M., Xu, Y., & Yin, W. (2013). Improved iteratively reweighted least squares for unconstrained smoothed ℓq minimization. *SIAM J. Numer. Anal., 51*, 927–57.

Last, B. J., & Kubik, K. (1983). Compact gravity inversion. *Geophysics, 48*(6), 713-721.

Lelievre, P. G., & Oldenburg, D. W. (2006). Magnetic forward modelling and inversion for high susceptibility. *Geophysical Journal International, 166*(1), 76-90.

Lelievre, P. G., & Oldenburg, D. W. (2009). A comprehensive study of including structural orientation information in geophysical inversions. *Geophysical Journal International, 178*(2), 623-637.

Lelièvre, P., Oldenburg, D., & Williams, N. (2009). Integrating geological and geophysical data through advanced constrained inversions. *Exploration Geophysics, 40*, 334-341.

Levin, E., & Meltzer, A. Y. (2017). Stopping criterion for iterative regularization of large-scale ill-posed problems using the picard parameter. *arXiv preprint arXiv*, 1707.04200.

Lewi, E. (1997). *Modelling and inversion of high precision gravity data (Doctoral dissertation, Munchen, Germany)*. Verlag der Bayerischen Akademie der Wissenschaften.

Li, D., Wu, Z., & Wang, Q. (2019). Edge guided compressive sensing for image reconstruction based on two-stage l0 minimization. *Journal of Visual Communication and Image Representation, 59*, 461-474.

Li, F., Xie, R., Song, W. Z., & Chen, H. (2018). Optimal Seismic Reflectivity Inversion: Data-Driven $\ell_p $-Loss-$\ell_q $-Regularization Sparse Regression. *IEEE Geoscience and Remote Sensing Letters, 16*(5), 806-810.

Li, F., Xie, R., Song, W., Zhao, T., & Marfurt, K. (2017). Optimal Lq norm regularization for sparse reflectivity inversion. *In SEG Technical Program Expanded Abstracts* (pp. 677-681). Society of Exploration Geophysicists.

Li, L., Fang, Y., Liu, L., Peng, H., Kurths, J., & Yang, Y. (2020). Overview of compressed sensing: sensing model, reconstruction algorithm, and its applications. *Applied Sciences, 10*, 5909.

Li, Y., & Oldenburg, D. W. (1996). 3-D inversion of magnetic data. *Geophysics, 61*(2), 394-408.

Li, Y., & Oldenburg, D. W. (1998). 3-D inversion of gravity data. *Geophysics, 63*(1), 109-119.

Li, Y., & Oldenburg, D. W. (2003). Fast inversion of large-scale magnetic data using wavelet transforms. *Geophysical Journal International, 152*, 251–265.

Li, Z., & Yao, C. (2020). 3D sparse inversion of magnetic amplitude data when strong remanence exists. *Acta Geophysica*, 1-11.

Lima, W. A., Silva, J. B., Santos, D. F., & Costa, J. C. (2019). A robust interactive estimation of the regularization parameter. *Geophysics, 84*(3), IM19-IM33.

Lin, J. W. (2012). Why Python is the next wave in earth sciences computing. *Bulletin of the American Meteorological Society, 93*(12), 1823-1824.

Lin, Y., & Wohlberg, B. (2008). Application of the UPRE method to optimal parameter selection for large scale regularization problems. *In 2008 IEEE Southwest Symposium on Image Analysis and Interpretation* (pp. 89-92). IEEE.

Loke, M. H., Acworth, I., & Dahlin, T. (2003). A comparison of smooth and blocky inversion methods in 2D electrical imaging surveys. *Exploration geophysics, 34*(3), 182-187.

Loris, I., & Verhoeven, C. (2012). Iterative algorithms for total variation-like reconstructions in seismic tomography. *GEM-International Journal on Geomathematics, 3*(2), 179-208.

Lutz, M. (2013). *Learning python: Powerful object-oriented programming*. O'Reilly Media, Inc.

Marques, E. C., Maciel, N., Naviner, L., Cai, H., & Yang, J. (2018). A review of sparse recovery algorithms. *IEEE Access, 7*, 1300-1322.

Martins, C. M., Lima, W. A., Barbosa, V. C., & Silva, J. B. (2011). Total variation regularization for depth-to-basement estimate: Part 1—Mathematical details and applications. *Geophysics, 76*(1), I1-I12.

McKinney, W. (2011). Pandas: a foundational Python library for data analysis and statistics. *Python for High Performance and Scientific Computing,, 14*(9).

McKinney, W. (2012). *Python for data analysis: Data wrangling with Pandas, NumPy, and IPython*. O'Reilly Media, Inc.

Meng, Z. (2018). Three-dimensional potential field data inversion with L0 quasinorm sparse constraints. *Geophysical Prospecting, 66*(3), 626-646.

Meng, Z. (2018). Three-dimensional potential field data inversion with L0 quasinorm sparse constraints. *Geophysical Prospecting, 66*(3), 626-646.

Meng, Z. H., Xu, X. C., & Huang, D. N. (2018). Three-dimensional gravity inversion based on sparse recovery iteration using approximate zero norm. *Applied Geophysics, 15*(3-4), 524-535.

Menke, W. (1989). *Geophysical Data Analysis: Discrete Inverse Theory,*. Revised edition, Academic Press.

Mohimani, H., Babaie-Zadeh, M., & Jutten, C. (2009). A fast approach for overcomplete sparse decomposition based on smoothed $\ell^{0} $ norm. *IEEE Transactions on Signal Processing, 57*(1), 289-301.

Morozov, V. A. (1984). *Methods for solving incorrectly posed problems*. Springer Science & Business Media.

Nabighian, M. N., Ander, M. E., Grauch, V. J., Hansen, R. O., LaFehr, T. R., Li, Y., . . . E., R. M. (2005). The historical development of the gravity method in exploration. *Geophysics, 70*, 63 – 89.

Nagy, D. (1966). The gravitational attraction of a right rectangular prism. *Geophysics, 31*(2), 362–371.

Nagy, D., Papp, G., & Benedek, J. (2000). The gravitational potential and its derivatives for the prism. *Journal of Geodesy, 74*, 552-560.

Namaki, L., Gholami, A., & Hafizi, M. A. (2011). Edge-preserved 2-D inversion of magnetic data: an application to the Makran arc-trench complex. *Geophysical Journal International,, 184*(3), 1058-1068.

Needell, D., & Tropp, J. A. (2010). CoSaMP: iterative signal recovery from incomplete and inaccurate samples. *Communications of the ACM, 53*(12), 93-100.

Needell, D., & Vershynin, R. (2010). Signal recovery from incomplete and inaccurate measurements via regularized orthogonal matching pursuit. *IEEE Journal of selected topics in signal processing, 4*(2), 310-316.

Nocedal, J., & Wright, S. (2006). *Numerical optimization*. Springer Science & Business Media.

Novák, P. (2010). Direct modelling of the gravitational field using harmonic series. *Acta Geodyn. Geomater, 7*(1), 35–47.

O'Leary, D. P. (1990). Robust regression computation using iteratively reweighted least squares. *SIAM Journal on Matrix Analysis and Applications, 11*(3), 466-480.

Ochs, P., Dosovitskiy, A., Brox, T., & Pock, T. (2015). On iteratively reweighted algorithms for nonsmooth nonconvex optimization in computer vision. *SIAM Journal on Imaging Sciences, 8*(1), 331-372.

Oldenburg, D. W., & Li, Y. (2005). Inversion for applied geophysics: A tutorial. *Near-surface geophysics*, 89-150.

Oliphant, T. E. (2007). Python for scientific computing. *Computing in Science & Engineering, 9*(3), 10-20.

Oliveri, G., Salucci, M., Anselmi, N., & Massa, A. (2017). Compressive Sensing as Applied to Inverse Problems for Imaging: Theory, applications, current trends, and open challenges. *IEEE Antennas and Propagation Magazine, 59*(5), 34-46.

Paoletti, V., Ialongo, S., Florio, G., Fedi, M., & Cella, F. (2013). Self-constrained inversion of potential fields. *Geophysical Journal International, 195*(2), 854–869.

Paterson, N. R., & Reeves, C. V. (1985). Applications of gravity and magnetic surveys: The state-of-the-art in 1985. *Geophysics, 50*(12), 2558-2594.

Peters, B., & Herrmann, F. J. (2017). Constraints versus penalties for edge-preserving full-waveform inversion. *The Leading Edge, 36*(1), 94-100.

Phillips, N. D. (2002). *Geophysical inversion in an integrated exploration program: Examples from the San Nicolas deposit (Doctoral dissertation, University of British Columbia).*

Pilkington, M. (1997). 3-D magnetic imaging using conjugate gradients. *GEOPHYSICS,, 62*(4), 1132–1142.

Pilkington, M. (2008). 3D magnetic data-space inversion with sparseness constraints. *Geophysics, 74*(1), L7-L15.

Portniaguine, O., & Zhdanov, M. S. (1999). Focusing geophysical inversion images. *Geophysics, 64*(3), 874-887.

Portniaguine, O., & Zhdanov, M. S. (2002). 3-D magnetic inversion with data compression and image focusing. *Geophysics, 67*(5), 1532-1541.

Qi, H., Chen, Z., Guo, J., & Zhou, L. (2015). Sparse-view computed tomography image reconstruction via a combination of L1 and SL0 regularization. *Bio-medical materials and engineering, 26*(s1), S1389-S1398.

Ramos, F. M., Velho, H. F., Carvalho, J. C., & Ferreira, N. J. (1999). Novel approaches to entropic regularization. *Inverse Problems, 15*(5), 1139.

Rao, K., Malan, P., & Perot, J. B. (2018). A stopping criterion for the iterative solution of partial differential equations. *Journal of Computational Physics, 352*, 265–284.

Ren, Z., Chen, C., Pan, K., Kalscheuer, T., Maurer, H., & Tang, J. (2017). Gravity anomalies of arbitrary 3D polyhedral bodies with horizontal and vertical mass contrasts. *Surveys in geophysics, 38*(2), 479-502.

Reynolds, J. M. (2011). *An introduction to applied and environmental geophysics.* John Wiley & Sons.

Rezaie, M. (2019). 3D non-smooth inversion of gravity data by zero order minimum entropy stabilizing functional. *Physics of the Earth and Planetary Interiors, 294*, 106275.

Rezaie, M. (2020). A sigmoid stabilizing function for fast sparse 3D inversion of magnetic data. *Near Surface Geophysics, 18*(2), 149-159.

Rezaie, M., Moradzadeh, A., & Nejati Kalate, A. (2017a). 3D gravity data-space inversion with sparseness and bound constraints. *Journal of Mining and Environment, 8*(2), 227-235.

Rezaie, M., Moradzadeh, A., Kalate, A. N., & Aghajani, H. (2017b). Fast 3D focusing inversion of gravity data using reweighted regularized Lanczos bidiagonalization method. *Pure and Applied Geophysics, 174*(1), 359-374.

Rish, I., & Grabarnik, G. (2014). *Sparse modeling: theory, algorithms, and applications.* CRC press, Taylor & Francis Group.

Rudin, L. I., Osher, S., & Fatemi, E. (1992). Nonlinear total variation based noise removal algorithms. *Physica D: nonlinear phenomena, 60*(1-4), 259-268.

Saab, R., Chartrand, R., & Yilmaz, O. (2008). Stable sparse approximations via nonconvex optimization. *In 2008 IEEE international conference on acoustics, speech and signal processing* (pp. 3885-3888). IEEE.

Scales, J. A., Gersztenkorn, A., & Treitel, S. (1988). Fast Lp solution of large, sparse, linear systems: Application to seismic travel time tomography. *Journal of Computational Physics, 75*(2), 314-333.

Schmidt, M., Fung, G., & Rosales, R. (2007). Fast optimization methods for ℓ1 regularization: A comparative study and two new approaches. *In European Conference on Machine Learning* (pp. 286-297). Berlin, Heidelberg: Springer.

Shang, W., Xue, W., Li, Y., & Xu, Y. (2020). Improved Primal–Dual Interior-Point Method Using the Lawson-Norm for Inverse Problems. *IEEE Access, 8*, 41053-41061.

Silva Dias, F. J., Barbosa, V. C., & Silva, J. B. . (2009). 3D gravity inversion through an adaptive-learning procedure. *Geophysics, 74*(3), I9-I21.

Silva Dias, F. J., Barbosa, V. C., & Silva, J. B. (2011). Adaptive learning 3D gravity inversion for salt-body imaging . *Geophysics, 76*(3).

Silva, J. B., & Barbosa, V. C. (2006). Interactive gravity inversion . *Geophysics, 71*(1), J1-J9.

Silva, J. B., Medeiros, W. E., & Barbosa, V. C. (2002). Practical applications of uniqueness theorems in gravimetry: Part I—Constructing sound interpretation methods. *Geophysics, 67*(3), 788-794.

Silva, J. B., Medeiros,W. E. and Barbosa, V. C. (2001). Potential-field inversion: Choosing the appropriate technique to solve geologic problem. *Geophysics, 66*, 511–520.

Silva, J. B., Oliveira, A. S., & Barbosa, V. C. (2010). Gravity inversion of 2D basement relief using entropic regularization. *Geophysics, 75*(3), I29-I35.

Silva, J. B., Oliveira, F. S., Barbosa, V. C., & Campos Velho, H. F. (2007). Apparent-density mapping using entropic regularization. *Geophysics, 72*(4), I51-I60.

Singh, A., Sharma, S. P., Akca, İ., & Baranwal, V. C. (2018). Fuzzy constrained Lp-norm inversion of direct current resistivity data. *Geophysics, 83*(1), E11-E24.

Snopek, K. (2005). *Inversion of gravity data with application to density modeling of the Hellenic subduction zone (Doctoral dissertation)*. Verlag nicht ermittelbar.

Stocco, S., Godio, A., & Sambuelli, L. (2009). Modelling and compact inversion of magnetic data. *Computer and Geosciences, 35*, 2111–2118.

Sun, J., & Li, Y. (2014). Adaptive L p inversion for simultaneous recovery of both blocky and smooth features in a geophysical model. *Geophysical Journal International, 197*(2), 882-899.

Templeton, R. (1981). Gravity surveys at Woodlawn, in Geophysical Case Study of the Woodlawn Ore Body, New South Wales, Australia. In R. Whiteley. Pergamon Press.

Tibshirani, R. (2011). Regression shrinkage and selection via the lasso: a retrospective. *Journal of the Royal Statistical Society: Series B (Statistical Methodology), 73*(3), 273-282.

Tikhonov, A. N., Goncharsky, A. V., Stepanov, V. V., & Yagola, A. G. (2013). *Numerical methods for the solution of ill-posed problems* (Vol. 328). Springer Science & Business Media.

Tikhonov, A., & Arsenin, V. (1977). *Solution of Ill-Posed Problems*. New York: W.H. Winston & Sons.

Trad, D., Ulrych, T., & Sacchi, M. (2003). Latest views of the sparse Radon transform. *Geophysics, 68*(1), 386-399.

Uieda, L., Barbosa, V. C., & Braitenberg, C. (2016). Tesseroids: Forward-modeling gravitational fields in spherical coordinates. *Geophysics, 81*(5), F41-F48.

Uieda, L., Oliveira Jr, V. C., & Barbosa, V. C. (2013). Modeling the Earth with fatiando a terra. *In Proceedings of the 12th Python in Science Conference*, (pp. 96-103).

Utsugi, M. (2019). 3-D inversion of magnetic data based on the L1–L2 norm regularization. *Earth, Planets and Space, 71*(1).

Van Rossum, G. (2005). *Python homepage*. Retrieved from URL: http://www. python. org.

Vatankhah, S., Anne Renaut, R., & Ardestani, V. E. (2018). A fast algorithm for regularized focused 3D inversion of gravity data using randomized singular-value decomposition. *Geophysics, 83*(4), G25-G34.

Vatankhah, S., Ardestani, V. E., & Renaut, R. A. (2014). Automatic estimation of the regularization parameter in 2D focusing gravity inversion: application of the method to the Safo manganese mine in the northwest of Iran. *Journal of Geophysics and Engineering, 11*(4).

Vatankhah, S., Ardestani, V. E., & Renaut, R. A. (2015). Application of the $\chi 2$ principle and unbiased predictive risk estimator for determining the regularization parameter in 3-D focusing gravity inversion. *Geophysical Journal International, 200*(1), 265-277.

Vatankhah, S., Renaut, R. A., & Ardestani, V. E. (2017). 3-D Projected L 1 inversion of gravity data using truncated unbiased predictive risk estimator for regularization parameter estimation. *Geophysical Journal International, 210*(3), 1872-1887.

Vatankhah, S., Renaut, R. A., & Ardestani, V. E. (2018). Total variation regularization of the 3-D gravity inverse problem using a randomized generalized singular value decomposition. *Geophysical Journal International, 213*(1), 695-705.

Vatankhah, S., Renaut, R. A., & Liu, S. (2020). Research Note: A unifying framework for the widely used stabilization of potential field inverse problems. *Geophysical Prospecting, 68*(4), 1416-1421.

Virtanen, P., Gommers, R., Oliphant, T. E., Haberland, M., Reddy, T., Cournapeau, D., & Van Mulbregt, P. (2020). SciPy 1.0: fundamental algorithms for scientific computing in Python. *Nature methods, 17*(3), 261-272.

Vogel, C. R. (2002). *Computational methods for inverse problems*. Society for Industrial and Applied Mathematics.

Wang, B., Wan, W., Wang, Y., Ma, W., Zhang, L., Li, J., & Gao, F. (2017). An L p (0≤ p≤ 1)-norm regularized image reconstruction scheme for breast DOT with non-negative-constraint. *Biomedical engineering online, 16*(1), 1-19.

Wang, C., Yu, P., Zhang, L., Zhao, C., & Shi, B. (2019). 2D magnetotelluric sharp boundary inversion using an exponential stabilizing functional. *In SEG Technical Program Expanded Abstracts* (pp. 1194-1198). Society of Exploration Geophysicists.

Wang, J. (2020). Non-convex ℓ p regularization for sparse reconstruction of electrical impedance tomography. *Inverse Problems in Science and Engineering*, 1-22.

Wang, J., Kwon, S., & Shim, B. (2012). Generalized orthogonal matching pursuit. *IEEE Transactions on signal processing, 60*(12), 6202-6216.

Wang, L., Wang, J., Xiang, J., & Yue, H. (2019). A re-weighted smoothed-norm regularized sparse reconstructed algorithm for linear inverse problems. *Journal of Physics Communication, 3*(7), 075004.

Wang, L., Ye, P., & Xiang, J. (2018). A modified algorithm based on smoothed l0 norm in compressive sensing signal reconstruction. *In 2018 25th IEEE International Conference on Image Processing (ICIP)* (pp. 1812-1816). IEEE.

Wang, L., Yin, X., Yue, H., & Xiang, J. (2018). A regularized weighted smoothed L0 norm minimization method for underdetermined blind source separation. *Sensors, 18*(12), 4260.

Wang, Y., & Ma, S. (2007). Projected barzilai–borwein method for large-scale nonnegative image restoration. *Inverse Problems in Science and Engineering, 15*(6), 559–583.

Wei, Z., Zhang, J., Xu, Z., Huang, Y., Liu, Y., & Fan, X. (2018). Gradient projection with approximate L0 norm minimization for sparse reconstruction in compressed sensing. *Sensors, 18*(10), 3373.

Wen, F., Pei, L., Yang, Y., Yu, W., & Liu, P. (2017). Efficient and robust recovery of sparse signal and image using generalized nonconvex regularization. *IEEE Transactions on Computational Imaging, 3*(3), 566-579.

Wen, J., Zhou, Z., Wang, J., T. X., & Mo, Q. (2016). A sharp condition for exact support recovery with orthogonal matching pursuit. *IEEE Transactions on Signal Processing, 65*(6), 1370-1382.

Whiteley, R. J. (2016). *Geophysical Case Study of the Woodlawn Orebody, NSW Australia: The First Publication of Methods and Techniques Tested Over a Base Metal Orebody of the Type which Yields the Highest Rate of Return on Mining Investment with Modest Capital Requirements.* Elsevier.

Wieczorek, M. A. (2007). Gravity and topography of the terrestrial planets, in Treatise on Geophysics. *Elsevier-Pergamon, 10*, 165–206.

Wijns, C., & Kowalczyk, P. (2007). Interactive geophysical inversion using qualitative geological constraints. *Exploration Geophysics, 38*(3), 208-212.

Wild-Pfeiffer, F., & Heck, B. (2007). Comparison of the modelling of topographic and isostatic masses in the space and the frequency domain for use in satellite gravity gradiometry. *Gravity Field of the Earth, 73*(18), 312-317.

Wolke, R., & Schwetlick, H. (1988). Iteratively reweighted least squares: algorithms, convergence analysis, and numerical comparisons. *SIAM journal on scientific and statistical computing, 9*(5), 907-921.

Xiang, J., Yue, H., Yin, X., & Ruan, G. (2018). A Reweighted Symmetric Smoothed Function Approximating L0-Norm Regularized Sparse Reconstruction Method. *Symmetry, 10*(11), 583.

Xiang, J., Yue, H., Yin, X., & Wang, L. (2019). A New Smoothed L0 Regularization Approach for Sparse Signal Recovery. *Mathematical Problems in Engineering*.

Ye, X., Zhu, W. P., Zhang, A., & Yan, J. (2013). Sparse channel estimation of MIMO-OFDM systems with unconstrained smoothed l 0-norm-regularized least squares compressed sensing. *EURASIP Journal on Wireless Communications and Networking, 2013*(1), 282.

Yuan, G., & Ghanem, B. (2017). L0 TV: A Sparse Optimization Method for Impulse Noise Image Restoration. *IEEE transactions on pattern analysis and machine intelligence., 41*(2), 352-364.

Zhang, L., Koyama, T., Utada, H., Yu, P., & Wang, J. (2012). A regularized three-dimensional magnetotelluric inversion with a minimum gradient support constraint. *Geophysical Journal International, 189*(1), 296-316.

Zhang, Y., Yan, J., Li, F., Chen, C., Mei, B., Jin, S., & Dohm, J. H. (2015). A new bound constraints method for 3-D potential field data inversion using Lagrangian multipliers. *Geophysical Journal International, 201*(1), 267-275.

Zhang, Z., Xu, Y., Yang, J., Li, X., & Zhang, D. (2015). A survey of sparse representation: algorithms and applications. *IEEE, 3*, 490-530.

Zhao, C., Yu, P., & & Zhang, L. (2016). A new stabilizing functional to enhance the sharp boundary in potential field regularized inversion. *Journal of Applied Geophysics, 135*, 356-366.

Zhdanov, M. S. (2002). *Geophysical inverse theory and regularization problems* (Vol. 36). Elsevier.

Zhdanov, M. S. (2009). New advances in regularized inversion of gravity and electromagnetic data. *Geophysical Prospecting*, 463–478.

Zhdanov, M. S. (2015). *Inverse theory and applications in geophysics* (Vol. 36). Elsevier.

Zhdanov, M. S., Ellis, R., & Mukherjee, S. (2004). Three-dimensional regularized focusing inversion of gravity gradient tensor component data. *Geophysics, 69*(4), 925-937.

Zhdanov, M. S., Endo, M., Cox, L. H., Čuma, M., Linfoot, J., Anderson, C., & Gribenko, A. V. (2014). Three-dimensional inversion of towed streamer electromagnetic data. *Geophysical Prospecting, 62*(3), 552-572.

Zhou, Z., & Yu, J. (2019). A new nonconvex sparse recovery method for compressive sensing. *Frontiers in Applied Mathematics and Statistics,, 5*, 14.

Zibulevsky, M., & Elad, M. (2010). L1-L2 optimization in signal and image processing. *IEEE Signal Processing Magazine, 27*(3), 76-88.

Appendix A Title and Abstract of published and submitted manuscripts to different journals

Appendix A.1 Gravity Inversion Method to Produce Compact and Sharp Images Using L0-norm Constraint with Auto-adaptive Regularization and Combined Stopping Criteria.

Abstract

We present a gravity inversion method that can produce compact and sharp images, to assist the modeling of non-smooth geologic features. The proposed iterative inversion approach makes use of L0-norm stabilizing functional, hard, and physical parameter inequality constraints, and depth weighting function. The method incorporates an auto-adaptive regularization technique, which automatically determines a suitable regularization parameter and error weighting function that helps to improve both the stability and convergence of the method. The auto-adaptive regularization and error weighting matrix are not dependent on the known noise level. Because of that, the method yields reasonable results even the noise level of the data is not known properly. The utilization of an effectively combined stopping rule to terminate the inversion process is another improvement that is introduced in this work. The capacity and the efficiency of the new inversion method were tested by inverting randomly chosen synthetic and measured data. The synthetic test models consist of multiple causative blocky bodies, with different geometries and density distributions that are vertically and horizontally distributed adjacent to each other. Inversion results of the synthetic data show that the developed method can recover models that adequately match the real geometry, location, and densities of the synthetic causative bodies. Furthermore, the testing of the improved approach using published real gravity data confirmed the potential, practicality of the method in producing compact and sharp inverse images of the subsurface.

Appendix A.2 Compact and Sharp Gravity Inversion Method Using L_0-norm Regularization with New Depth Weighting and Bound Constraints.

Abstract

Abstract

Delineating localized and blocky geologic features through the inversion of gravity data is an important goal in a range of geophysical investigations. To recover such geologic features, we have improved a gravity inversion method that produces compact and sharp images of the subsurface density distribution. The method is based on the minimization of an objective function, which consists of data misfit and L_0-norm stabilizing functions, by iteratively reweighted least-squares (IRLS) algorithm. To determine a suitable regularization parameter at each iteration an auto-adaptive method is implemented. As a major contribution of this work, an improved depth-weighting function that counteracts the natural decay of the kernel, in gravity data inversion, is introduced. This function has improved depth resolution and led to realistic geological features. Unlike previous results, in which the depth weighting functions were determined manually, the parameters in our function were determined automatically no matter where the source is located and independent of the cell size of the subsurface model. This has led to an iterative approach that improved the compact gravity inversion method by incorporating a set of constraints, including compactness and physical inequality constraints. To evaluate the practicality and resolution capability, the method was tested using a number of synthetic data sets from geometrically complex models and real data collected from different geological settings. The results of the inversion confirmed the applicability, effectiveness, and efficiency of our method in producing geologically acceptable density distribution of multiple bodies that lie adjacent to each other. The results also illustrated the capabilities of the function in resolving and reproducing models that are vertically or horizontally placed relative to each other.